DISSERTATION
submitted to the
Combined Faculties for the Natural Sciences and for Mathematics
of the Ruperto-Carola University of Heidelberg, Germany
for the degree of Doctor of Natural Sciences

Put forward by
M.S. Chia-Chun Lu (盧佳均)
born in Taipei, Taiwan
Oral examination: 17th April 2013

An advanced direction reconstruction technique and application to the observation with H.E.S.S.

Referees:
Prof. Dr. Werner Hofmann
Prof. Dr. Stefan Wagner

Kurzfassung

H.E.S.S. (High Energy Stereoscopic System) ist ein Array von fnf abbildenden Cherenkov Teleskopen zur Untersuchung nichtthermischer Prozesse im Universum mit Hilfe hochenergetischer (Tera-Elektronenvolt; TeV) Gammastrahlung. In dieser Arbeit wird ein Algorithmus zur Richtungsrekonstruktion entwickelt, der eine verbesserte rumliche Auflsung und Sensitivitt im Vergleich mit Standardmethoden erreicht und auf die Analyse der komplexen Morphologie in der grossen Magellanschen Wolke angewandt wird. Die grosse Magellansche Wolke ist eine Satellitengalaxie der Milchstrasse in einer Entfernung von 48 kpc. Dieser relativ kleine Abstand macht sie zum guten extragalaktischen Labor fr astronomische Beobachtungen. Die H.E.S.S. Beobachtungen konzentrieren sich auf drei Objekte: den junge Supernovaberrest SN 1987A, den Pulsarwindnebel N157B und die "Superbubble" 30DorC. Obwohl der TeV-Fluss von SN1987A auf einem fr H.E.S.S. detektierbaren Niveau vorhergesagt wird, kann in den bisher verfgbaren Daten keine signifikante Emission nachgewiesen werden. Aus den Messungen wird demnach eine TeV-Flussobergrenze bestimmt. Das zweite Objekt - der Pulsarwindnebel N 157B - wurde detektiert, dessen Spektrum rekonstruiert und dadurch physikalische Parameter eingeschrnkt. Der Gammastrahlungsfluss impliziert, dass N157B der energetischste bekannte Pulsarwindnebel ist. In der Nhe von N157B wurde ein Signal aus der Richtung von 30DorC gemessen. Die Existenz dieser Quelle wird durch detaillierte morphologische Studien demonstriert und ihr Verhltnis zu 30DorC wird diskutiert.

Abstract

The High Energy Stereoscopic system (H.E.S.S.) is an array of five imaging atmospheric Čerenkov telescopes which aims at exploring the high energy non-thermal processes in the universe via detecting very-high-energy (VHE) γ rays. In this work, an advanced direction reconstruction algorithm which yields better point spread function (PSF) and sensitivity is developed to cope with the complex morphology analysis in the Large Magellanic Cloud (LMC) region. LMC is a satellite galaxy of Milky Way at the distance of 48 kpc. The relatively short distance makes it a good extra-galactic laboratory for astronomical observation. The H.E.S.S. observation focuses on the three targets hosted in this region: the young supernova remnant SN 1987a, the pulsar wind nebula N 157B, and the superbubble 30Dor C. The VHE flux of SN 1987a is predicted at the detectable level for H.E.S.S. but no significant detection is found in the current dataset. An upper limit on the γ-ray flux is derived for this target. The pulsar wind nebular N 157B is detected, and the spectrum and other physical quantities are derived. The γ-ray flux shows that it is the most-energetic-ever observed pulsar wind nebula. At the vicinity of N 157B, we find extra γ-ray excess towards the direction of 30Dor C. The existance of this source is established by detailed morphology studies and its connection to 30Dor C is discussed.

Contents

List of Figures

List of Tables

Preface

After 10 years of operation, H.E.S.S. has achieved a great success on the Galactic plane survey where $\sim$ 70 γ-ray emitters have been found. Most of them are associated as pulsar wind nebulae (PWNs) or supernova remnants (SNRs). For extra-galactic observations, most of the sources are AGNs. Only very few of extra-galactic non-AGN sources are detected by H.E.S.S, such as the starburst galaxy NGC 253, the radio galaxies M 87 and Centaurus A. Due to their large distance to the Earth (3.5 Mpc for NGC 253, 16 Mpc for M 87, and $3 - 5$ Mpc for Centaurus A), it is difficult to resolve the detailed structures of these sources with the $\sim 0.1^\circ$ angular resolution of H.E.S.S..

The Large Magellanic Cloud (LMC) is an excellent target for studies of extra-galactic non-AGN objects. Its nearby distance of 48 kpc makes the studies of its individual objects possible. H.E.S.S. observation focuses on the Tarantula Nebula region in the LMC, initially aiming to the detection of SN 1987a. This very young SNR, still in its free expansion state, is a very unique target for VHE γ-ray observation while most of other VHE γ-ray SNRs are in or entering the Sedov phase. No significant point-like emission was found from SN 1987a, instead, the emission from the PWN, N 157B, was detected. The fact that the emission is extended has become more and more significant with the increase of observation time. The nature of this extended emission is very intriguing because a 5000-year-old PWN at 48 kpc is expected to have a angular size much smaller than the H.E.S.S. point-spread function.

An advanced Hillas-type reconstruction technique is developed in this work, aiming on achieving a better angular resolution. The performance of this technique is compared with the currently-used one and the systematic uncertainties are studied with strong known sources. This technique is applied to the analysis

of the LMC. A second source next to N 157B is found with a significance of 5.5σ on top of the superbubble 30 Dor C.

The chapters in this thesis are arranged as follows:

- Chapter1: An introduction about the imaging atmospheric Čerenkov technique and the H.E.S.S. experiment.
- Chapter2: The methods about H.E.S.S. data analysis, especially with detailed descriptions about the event reconstruction.
- Chapter3: Performance and systematic studies with known sources.
- Chapter4: A brief introduction about particle acceleration and VHE γ-ray production is and the results of H.E.S.S. observation on the LMC.
- Chapter5: Conclusions and outlook are given.

Chapter 1

Detection of very high energy gamma rays

The range of the observation of the electromagnetic spectrum of astronomical objects has been intensively expanded in the last few decades. The launch of sophisticated observatories in space allows us to explore the high-energy world of the universe. Satellite-based instruments such as EGRET [Hartman et al., 1999], INTEGRAL [Winkler et al., 2003] and Fermi [Atwood et al., 2009] have made remarkable achievements in the detection of high-energy γ rays (HE; 1 MeV $<$ E $<$ 100 GeV). In the very-high-energy γ-ray regime (VHE; E $>$ 100 GeV), where the flux steeply declines, however, the small effective area (with the order of $\mathcal{O}(\mathrm{m}^2)$) of satellite-based instruments is no longer sufficient. The Imaging Atmospheric Cerenkov Technique (IACT) with its tremendously increased effective area ($> \mathcal{O}(10^4\,\mathrm{m}^2)$) compensates for the declining γ-ray flux and has been proven as the most successful technique for VHE γ-ray detection. In this chapter, a brief introduction to the IACT technique will be addressed.

1.1 Air showers

When an energetic particle (e.g. a photon, proton, or heavy nucleus) enters the atmosphere of the Earth, secondary particles are generated through its interaction with the atoms in the atmosphere, and the energy and momentum of the primary particle are distributed to the secondary particles. This process repeats for the secondary particles, developing into a particle cascade referred to as an Extensive Air Shower (EAS). The characteristics of EAS vary according to the species of primary particles. One can categorize the EAS into two types: electromagnetic (EM) showers and hadronic showers. In EM showers, the EAS is induced by a photon, positron, or electron through EM interactions. In hadronic showers, the

EAS is induced by a hadron (e.g. a proton), and both electromagnetic and strong interactions are involved in the shower development.

1.1.1 Electromagnetic showers

When a γ, electron or position enters the atmosphere and induces an EM shower, three processes can happen: Bremsstrahlung, pair production and ionization. Bremsstrahlung happens when a moving charged particle (e.g. an electron) gets deflected by the Coulomb field (e.g. of the nuclei in the atmosphere). The electron is decelerated and losses its energy by the form of emitting photons. In the relativistic regime, the energy loss rate is proportional to the electron's energy (see the derivation in e.g. [Longair, 1992a]). The radiation length X_0 is defined as the mean distance after which a particle remains only $1/e$ of its original energy,

$$E(x) = E_0 \cdot e^{-x/X_0}. \tag{1.1}$$

For electrons, $X_0 = 37.2\mathrm{g} \cdot \mathrm{cm}^{-2}$, corresponding to 300 m at the sea level. The energy loss rate of this process is inversely proportional to the squared particle mass so the energy loss efficiency is higher for electrons and positrons than for protons. Pair Production happens when a photon with an energy greater than twice the rest energy of an electron interacts with the Coulomb field of nuclei in the atmosphere. The mean free path or also called the conversion length, defined as the distance after which $(1 - 1/e)$ fraction of photons are converted into electrons and positrons, is slightly larger than the bremsstrahlung radiation length, $X_c = 9/7X_0$. These two processes repeat and create particles building up a particle cascade. This cascade expands to its maximum when the mean particle energy drops below the critical energy E_c. At the critical energy E_c, the energy loss via ionization of air molecules starts to dominate over the creation of new particles and the shower starts dying out.

Under three simplifications, the basic properties of an electromagnetic air shower can be derived with a simplified model [Heitler, 1954]:

1. Only Bremsstrahlung and pair production processes are responsible for the creation of secondary particles.

2. The radiation length and conversion length are assumed to be equal, namely, $X_0 = X_c$.

3. The energy is shared equally between secondary particles.

The schematic diagram of this simplified model is shown in Figure 1.1. Let the traveled distance along the shower axis be x in unit of $\mathrm{g} \cdot \mathrm{cm}^{-2}$ and the energy of the primary particle be E_0. After $n = x/X_0$ branchings, the shower consists

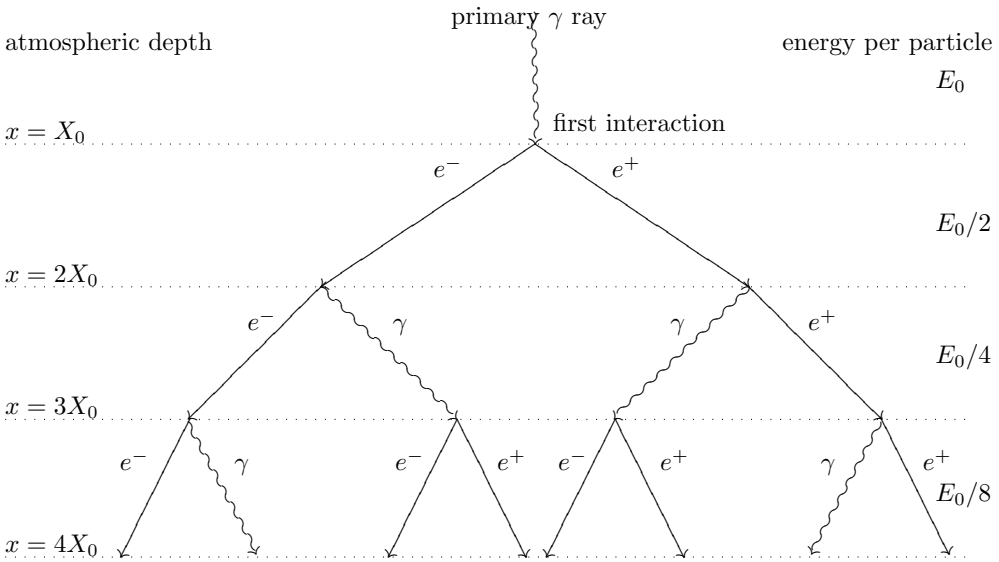

Figure 1.1: Simplified model for the development of an electromagnetic shower in Heitler's approach. Taken from Ohm [2010].

of $N(x) = 2^{x/X_0}$ particles, and each of them has an energy of $E(x) = E_0 \cdot 2^{-x/X_0}$. The shower reaches the maximum when the secondary particles reach the critical energy E_c. The depth of the shower maximum, $X_{\max}$ can be expressed as:

$$E_0 \cdot 2^{-X_{\max}/X_0} = E_c \quad \Rightarrow \quad X_{\max} = \frac{\ln E_0/E_c}{\ln 2} \cdot X_0. \tag{1.2}$$

Also the number of particles at the shower maximum can be obtained:

$$N_{\max} = 2^{X_{\max}/X_0} = \frac{E_0}{E_c}. \tag{1.3}$$

To summarize, this model predicts the following characteristics of an EM shower:

- In the initial phase of the shower development, the number of particles increase exponentially with the traveled depth. This relation holds until the shower reaches the maximum.
- The maximum amount of particles is proportional to the energy of the primary particle.
- The depth of the shower maximum grows logarithmically with the energy

of the primary particle.

For more realistic cases, energy loss and other higher order interaction processes during shower development are taken into account by Monte-Carlo simulations.

1.1.2 Hadronic showers

Compared to EM showers, the development of hadronic showers is more complicated. The strong force interactions give rise to the development of a shower composed of hadrons (e.g. pions, kaons, nucleons and hyperons) and feed leptons and gammas into the EM component via charged and neutral meson decay. These EM sub-showers, which dominate Čerenkov emission, share about only 1/3 of the total primary particle energy. The other 2/3 of the total primary energy loses in the production of muons and neutrinos in the charged pion decay.

In some cases, most of the primary energy is transformed into a π^0 in one of the first interactions. This will lead to a shower development very similar to an electromagnetic shower even though the incident particle is of hadronic origin. The distinction between γ-ray and hadron induced showers is very important for VHE γ-ray observation because of the high hadronic background level. The intrinsic properties of these two kinds of showers and the distinction between them are discussed in the next subsection.

1.1.3 Difference between γ-ray and hadron induced showers

Due to the conversion of primary energy into the creation of muons and neutrinos as well as the dissipation of energy in nucleonic interactions, the number of charged particles in hadronic showers is about 1/3 of that of a γ ray with the same primary energy. That means that a 1 TeV proton produces roughly the same amount of Čerenkov light as a 300 GeV γ ray. In this energy regime, the proton has a larger mean free path length compared to the electromagnetic radiation length and conversion length ($X_p \approx 80\,\mathrm{g}\cdot\mathrm{cm}^{-2}$). Hence, hadronic showers penetrate deeper into the atmosphere and have on average a larger shower maximum $X_{\max}$.

In addition, the difference between involved interactions in the shower results in distinctive lateral extension. The lateral extension of a hadronic shower is determined by the transverse momentum which secondary particles receive during their creation via inelastic strong-force scattering on spatially extended targets. In the case of electromagnetic showers, the lateral spread is mainly determined by multiple scattering and is in general small compared to hadronic

showers. Hadronic air showers are characterized by complex multi-particle interactions, while electromagnetic showers are dominated by three-particle processes. Hadronic showers thus show a less pronounced radial symmetry and may have multiple distinct cores.

These properties can be seen in Figure 1.2 which shows the simulated tracks of a 300 GeV γ ray and a 1 TeV proton and the lateral Čerenkov light distribution of the same events on the ground.

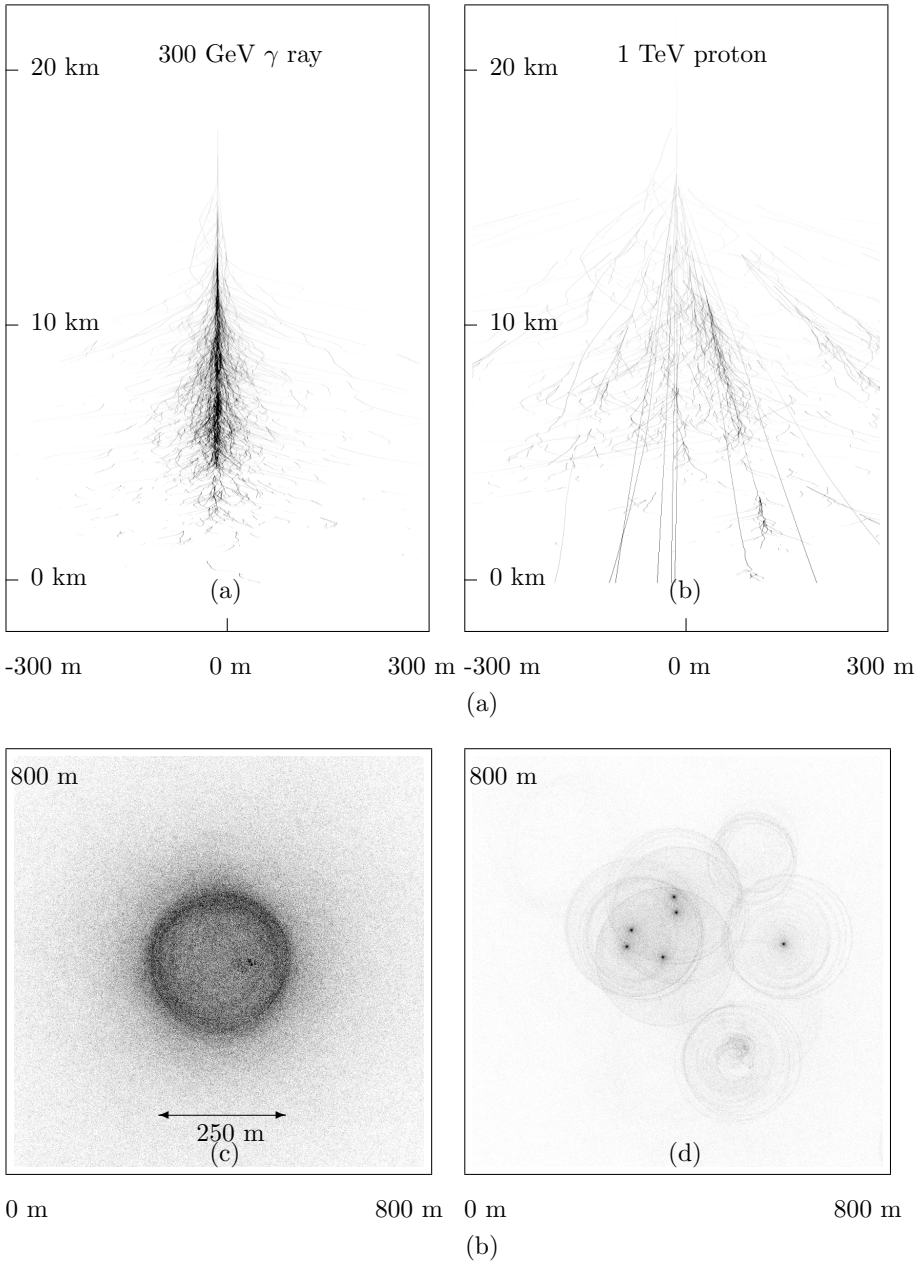

Figure 1.2: (a) Simulated tracks of the secondary particles in the shower as projected onto the (x,z) plane. The longitudinal development of an 300 GeV γ-ray shower is presented in the left panel and a 1 TeV proton is presented in the right panel. (b) Lateral Čerenkov light distribution of the showers on the ground for the same events as in (a). Taken from Bernlöhr [2000]

1.2 Atmospheric Čerenkov light

Most of the secondary particles in the EAS have highly-relativistic energies. They move with a velocity larger than the local phase velocity of light in the air (a dielectric medium) and emit Čerenkov radiation in a narrow cone. The half-angle ϑ_c of the Čerenkov cone for a particle with velocity $\beta = v/c$ in a medium with refractive index n is given by

$$\cos\vartheta = \frac{1}{\beta n}, \tag{1.4}$$

The threshold velocity of a particle to emit Čerenkov-light is $\beta_t = 1/n$. The corresponding threshold energy depends on the mass of the particle m_0 and the refractive index of the medium:

$$E_{\min} = \gamma_{\min} m_0 c^2 = \frac{m_0 c^2}{\sqrt{1-n^{-2}}}\,. \tag{1.5}$$

Since the threshold energy is proportional to the mass of particle, light particles such as electrons dominate Čerenkov emission in air showers. The threshold energy also depends on the refractive index and the refractive index varies with the height due to the continuous variation of air density. With the decreasing height, the density and refractive index increase. Hence, the threshold energy and the half-angle depend on the altitude in the atmosphere. Under the simplified assumption of an isothermal atmosphere, one can use the barometric formula for the density of air to express the dependency of the refractive index on the height in the atmosphere:

$$n(h) = n_0 e^{-h/h_0}, \qquad n_0 = 0.00029,\ h_0 = 7250\,m\,. \tag{1.6}$$

With Eq. (1.4) and Eq. (1.6), one can get the relation between the emission half-angle ϑ_c and height as shown in the left panel of Figure 1.3. At the observation level, the Čerenkov light cone around the particle trajectory results in a roughly circular ring with radius R_c given by

$$R_c = (h - h_{\rm obs}) \cdot \tan\vartheta_c\,, \tag{1.7}$$

where $h_{\rm obs}$ is the observation height above sea level. The change of R_c with the emission height is shown in the middle panel of Figure 1.3. Superimpositions of the light cones emitted at different heights yield an almost homogeneous light distribution in a circle with radii between 80 m and 150 m around the shower axis for an electromagnetic shower. If all the particles emitting Cerenkov light would move parallel and close to the shower axis, there would be no light outside the

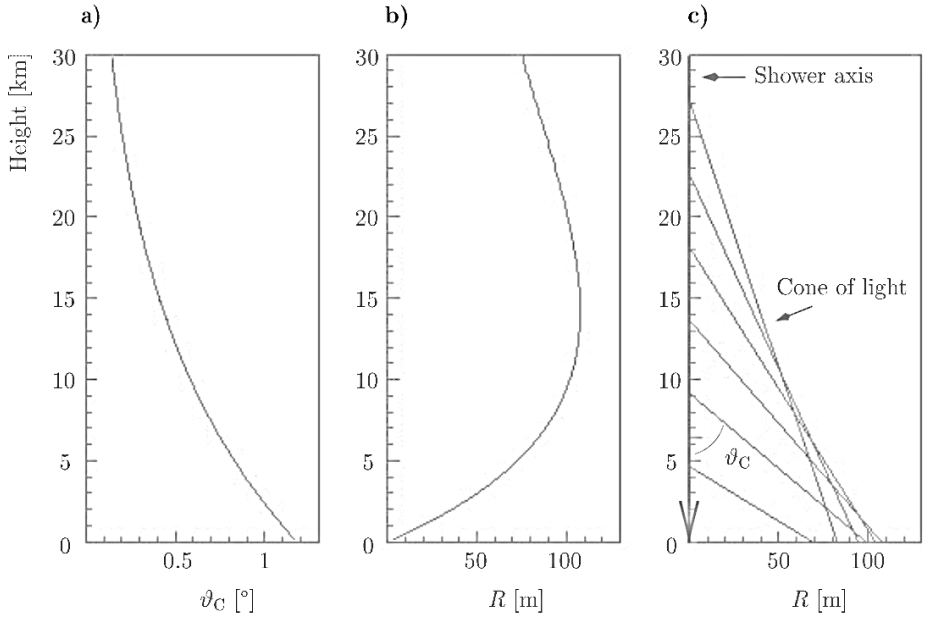

Figure 1.3: (a) The changing of the Čerenkov cone half-angle ϑ_c with the atmosphere height. With the decreasing height, ϑ_c gets larger due to the increase of the atmosphere density and refractive index. (b) The ring radius of the Čerenkov light cone on the ground at $2200\,m$ above sea level. The ring radius increases with the height due to the increasing ϑ_c until it is canceled out by the geometry effect. (c) The Čerenkov light cone emitted at different heights. The beaming effect at $100\,m$ due to the combination of increasing ϑ_c and decreasing height is clearly seen. This effect results in the ring feature in Figure 1.2(b). Taken from Ulrich [1996].

maximum radius. However, due to multiple scattering of the particles, the light distribution is smeared out. One can see this phenomenon in Figure 1.2(b) which shows the simulated lateral Čerenkov light distribution on the ground for a γ and a proton. In contrast to the smeared and symmetric light distribution for a γ, protons show the asymmetric structures with faint circles originating from electromagnetic sub-showers.

The effect of the zenith angle

The properties of the emission of atmospheric Čerenkov light in electromagnetic cascades discussed above are for observations at zenith. The radius of Čerenkov light pool, which is an important factor for telescope design and event reconstruc-

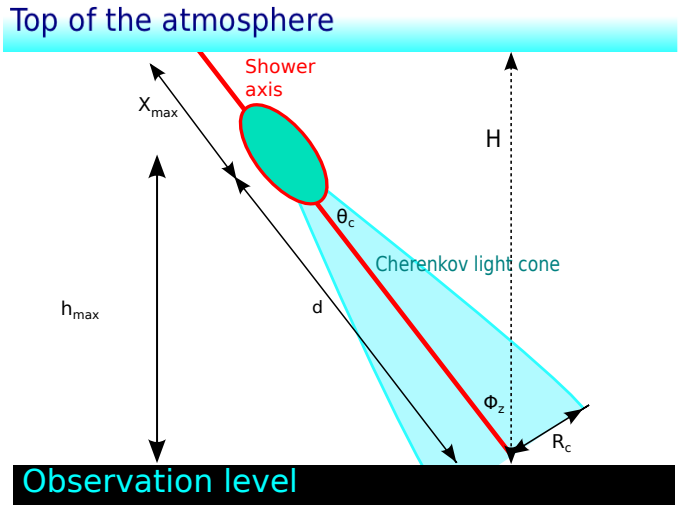

Figure 1.4: Illustration of the geometry of the Čerenkov light cone. The light-cone radius on the observation level depends on ϑ_c, the half angle of the cone, and d, the distance from the shower maximum point to the observation level. Since $X_{\max}$ is fixed in a small range for showers with the same energy, d increases with the zenith angle.

tion, however, is dependent on the zenith angle of the shower.

Figure 1.4 shows the zenith angle dependency of the geometry of Čerenkov light cone. One can see an increase of d, the distance between the shower maximum and the impact point of the Čerenkov front, with the zenith angle. The formation of the shower depends on the traveled atmospheric depth, so the depth of the shower maximum $X_{\max}$ is thus the atmospheric depth in g/cm^2 along the shower axis. With increasing zenith angles, the height of the shower maximum above see level ($h_{\max}$) remains almost unchanged, but the Čerenkov light cone travels increasingly larger distances until the observation level and widens correspondingly; namely, the Čerenkov radius on the ground (in a plane perpendicular to the shower axis) increases. Figure 1.4 shows the height of the shower maximum above observation level $h_{\max}$, which can be approximately calculated as

$$h_{\max} = H - \cos\phi_z \cdot X'_{\max}\,, \tag{1.8}$$

where H is the height of the top of the atmosphere, ϕ_z is the zenith angle of the shower, and $X'_{\max}$ is the distance in meters the shower has traveled before reaching its maximum, equivalent to $X_{\max}$ in units of $g \cdot cm^{-2}$. The distance d

between the shower maximum and impact point on the ground is

$$d = \frac{h_{\max}}{\cos\phi_z} = \frac{H}{\cos\phi_z} - X^{'}_{\max}\,. \tag{1.9}$$

Adopting Eq.(1.7) with $\tan\vartheta_c \approx \vartheta_c$, one obtains the zenith-angle dependence of the Čerenkov light-cone radius on the observation level,

$$R_c = \left(\frac{H}{\cos\phi_z} - X^{'}_{\max}\right)\cdot\vartheta_c\,. \tag{1.10}$$

Figure 1.5 shows the zenith-angle dependence of the lateral profile of Čerenkov-photon density on the observation level for γ-ray induced showers. The mean image amplitude measured with Čerenkov telescopes in unit of photo-electrons (p.e.) is a quantity equivalent to the photon density, and the impact distance is the perpendicular distance between the telescope and shower axis. The characteristics of the distribution are summarized as follows.

At lower energies, the photon density first increases with the distance and reaches to a maximum before declining. This is called as *Čerenkov shoulder* as seen in the right panel of Figure 1.5. The position of this break is usually identified with the Čerenkov-cone radius R_c as expressed in Eq. (1.10). Most of the Čerenkov light is emitted in a narrow region around the shower maximum. The break is pronounced if the shower maximum is formed at heights where the shortened traveling distance of the Čerenkov light is canceled out by the widened half angle in shower development with the decreasing height. As shown in Figure 1.3, the effect as described above results in a beaming effect on the observation level when Čerenkov light emitted in different heights is focused on the Čerenkov-cone radius. One can see in Figure 1.5 that this radius increases with the zenith angle and the shape of the distribution depends on the shower energy.

For energies around 1 TeV, the photon density is roughly constant up to a certain distance, for 20° zenith angle, it is at $\approx$ 130 m. Beyond this point, the density starts to declines. For larger energies, the plateau and the *Čerenkov shoulder* are less pronounced because the shower maximum is formed deeper in the atmosphere where the canceling described above does not happen any more. At very high energies, namely, 10 TeV for 20° zenith angle and 100 TeV for 60° zenith angle, this break disappears.

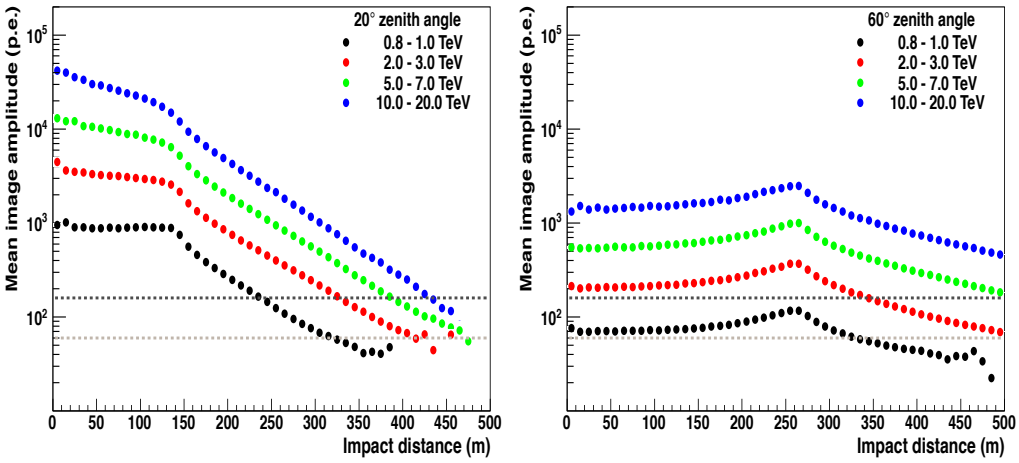

(a) (b)

Figure 1.5: Image amplitude (*image size*) is a quantity equivalent to the observed Čerenkov light intensity. The plots shown here represent the lateral Čerenkov-light distribution for showers with different energy at 20° and 60° zenith angle. The horizontal dashed lines at 60 p.e. and 160 p.e. correspond to the *image size* cut which will be introduced in Chapter 3.

1.3 Imaging Atmospheric Čerenkov technique

As mentioned in the previous sections, when a γ-ray or cosmic-ray particle enters the atmosphere, Čerenkov radiation is generated by the superluminal particles in the induced extended air showers. The imaging atmospheric Čerenkov telescopes makes use of the Earth's atmosphere as a part of the detector. It takes images of the emitted Čerenkov light which tracks the development of the EAS. Due to the large extension of the Čerenkov light pool (typically several hundred meters in radius), a much larger detection area is available compared to satellite-based experiments. This technique was pioneered by the Whipple collaboration [Weekes et al., 2002] who detected the Crab nebula in 1989. This is the first time that a VHE γ-ray source is detected with this technique. The HEGRA collaboration [Daum et al., 1997] later built an array of Cerenkov telescopes to perform stereoscopic observations of air showers. The simultaneous observation with multiple telescopes has several advantages:

- A trigger coincidence of multiple telescopes can be required to reduce random triggers of night-sky background (NSB) light and local muons which have narrow Čerenkov light cone triggering only one single telescope.
- Multiple views of the same air shower can improve the direction and energy reconstruction of the shower.
- Since that cosmic-ray induced showers are much more irregular and asymmetric than γ-ray showers, viewing the shower from different sides improves the rejection of the dominant hadronic background.

Several current-generation IACT experiments such as H.E.S.S. [Hinton, 2004], MAGIC [Lorenz, 2004], and VERITAS [Weekes et al., 2002] are operating. Depending on the scientific purpose and aimed energy band, the layouts and designs are different, but the basic principles are similar. Čerenkov telescopes map the Čerenkov light of air showers with parabolic mirrors onto a camera in the focal plane of the mirrors. Since the light rays viewed under the same opening angle are imaged onto the same point in the camera, the camera coordinate system is commonly defined as an angular system. On the other words, Čerenkov telescopes measure the angular distribution of Čerenkov light from air showers. For γ-ray induced air showers, the shower maximum is typically at the height of 10 km. Most of the Čerenkov light is emitted in a narrow cylindrical region around the shower axis at this height. The longitudinal distribution is much wider than the lateral distribution so the mapped image in the camera is roughly an ellipse. Figure 1.6 illustrates the image mapping of an air shower onto a camera. In the left panel, one can see that:

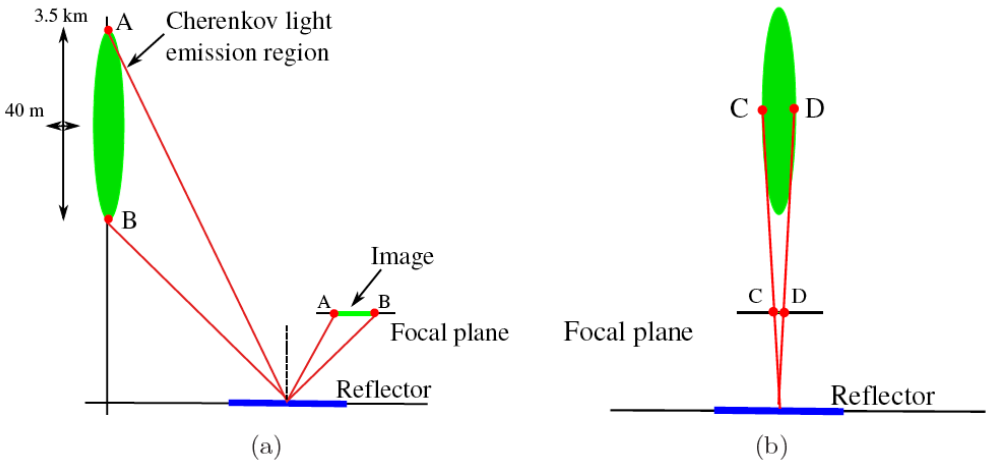

Figure 1.6: Illustration of the mapping of an air shower onto a camera. The left panel shows the view of the plane spanned by the shower axis and the telescope position. The length of the image is determined by the angles between points A and B. The right panel shows the perpendicular view from the telescope towards the shower. The width of the image is determined by the angles between points C and D. Taken from [Hoppe, 2008].

- The major image axis points back to the incident direction of the primary particle.
- The distance between the shower axis and the reflector axis affects the position and length of the image in the camera.
- The length of the image also depends on the inclination of the shower axis with respect to the telescope pointing direction.

And the right panel illustrates the mapping of lateral Čerenkov-light distribution. The angular separation between point C and D translates to the width of the image in the camera.

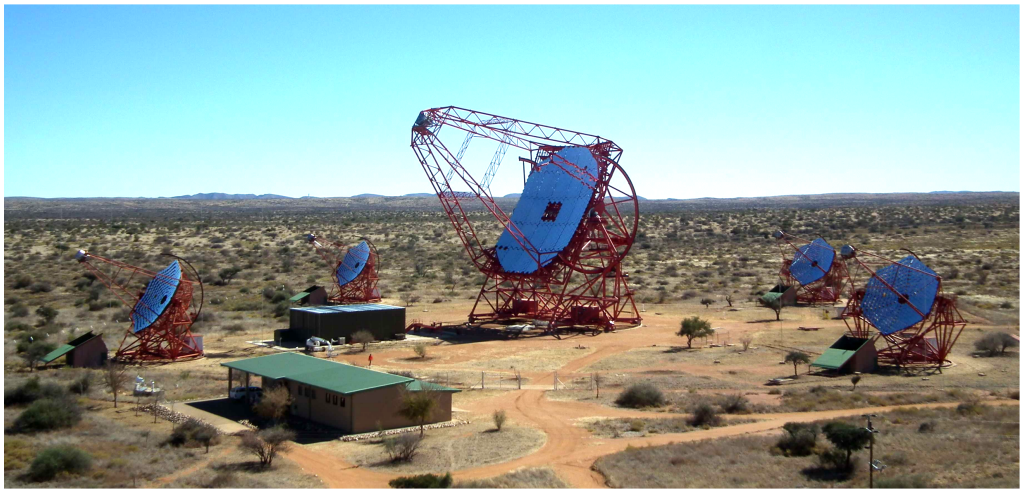

Figure 1.7: Overview of the H.E.S.S. array. The whole array is composed of one large telescope and four identical small telescopes.

1.4 H.E.S.S. instrument

The High Energy Stereoscopic System (H.E.S.S.) is named after Victor Hess for his discovery of cosmic rays. It is a system of five Čerenkov telescopes which employs the IACT. The telescope array is located in the Khomas Highland in Namibia (23°16′17″S , 16°29′58″E), at 1800 m above sea level. The site location is about 100 km away from the capital Windhoek. The area close to the Gamsberg is renowned for its excellent conditions for astronomical observations [Wiedner, 1998]. To exude the influence of the moon light on the observation, H.E.S.S. telescopes only perform observations in moon-less nights. It was shown that 57% of the moon-less nights were cloud-free and in 94% of these nights, the relative humidity was below 90%. Additionally, the location of the H.E.S.S. array in the southern hemisphere makes this site perfectly suited for the study of a large number of potential VHE γ-ray sources located in the Milky Way.

1.4.1 Telescopes

Figure 1.7 shows the view of the whole array. The array is built in two phases. The four smaller telescopes (CT1, CT2, CT3, CT4) of phase I are arranged in a square of 120 m side length and started operation in late 2003. In the middle is the big CT5 telescope which started operating in July 2012. In this thesis, the data analysis is designed and tested for phase I, but can be easily expanded to phase II. The spacing of the telescopes is chosen as a compromise. Large distances between telescopes are desirable because they increase the collection

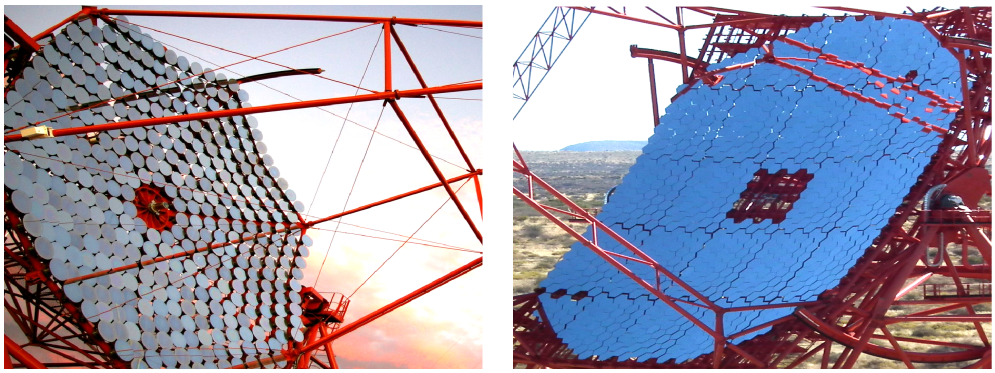

(a) Phase-I telescope (b) Phase-II telescope

Figure 1.8: Close-up views of the H.E.S.S. telescopes. The difference between the mirror designs can be seen.

area and provide good stereoscopic viewing conditions for close-by showers. The Čerenkov light pool of typical γ-ray air showers is, however, with the diameter of $\approx 250\,\mathrm{m}$. Larger distances between telescopes reduce the rate at which multiple telescopes are illuminated by the same shower. CT5 is placed at the center of the array for simultaneous observation of low energy showers.

The four phase-I telescopes are identical in construction. The mirror support structure has a diameter of 12 m and accommodates 382 spherical mirrors, each with a diameter of 60 cm, together adding up to a total reflector area of $108\,\mathrm{m}^2$. CT5 has a diameter of 28 m and accommodates 875 hexagonal mirrors, each with a flat-to-flat diameter of 90 cm, together adding up to a total reflector area of $614\,\mathrm{m}^2$. This larger reflector area lowers the observable energy threshold. The mirror structures of these two types of telescopes are shown in Figure 1.8.

The phase-I cameras have a 5° field of view and 60 drawers. Each drawer has 16 photon detector elements, also called pixels. In total, there are 960 pixels, each subtending an angle of 0.16°. The phase-II camera has a smaller field of view of 3.5°, 128 drawers and totally 2048 pixels, each subtending an angle of 0.067°.

1.4.2 Data taking

H.E.S.S. telescopes take data only in moon-less dark time. The available observation time is sub-divided into data-taking periods of typically 28 mins, which are called data runs. During a run, the telescopes are targeted at and track a certain astronomical object or a given position in the sky. For the multi-telescope observation mode, the data are stored to the disk only when at least two telescopes are triggered.

1.4.3 Monte-Carlo simulations

Data analysis and event reconstruction throughout this work are based on the Monte-Carlo air shower simulations. The simulations are done in two steps. First, the complete development of the air shower in the atmosphere and the formation of Čerenkov light is simulated by CORSIKA, COsmic Ray SImulations for KAscade [Heck et al., 1998]. An important aspect of shower simulations is the model for atmospheric transmission. The simulations used here have been compared with the real conditions in Namibia, in particular for two different sets of transmission tables calculated using MODTRAN [Bernlohr, 2000]. One is based on a rather conservative assumption of aerosol content: maritime haze and boundary layer starting at sea level. The other one corresponds to a clearer atmosphere: desert haze and boundary layer starting at 1800 m. The later one seems more appropriate for the desert-like conditions at the H.E.S.S. site and is used in the simulations for this work.

The second step is to simulate the optical and electronic response of the detector to air showers. The simulation used here is called *sim hessarray* [Bernlöhr, 2008]. It includes the exact layout of the light reflectors and telescope structures such as camera masts which cast shadows onto the cameras itself. The measured optical point-spread function (PSF) as well as quantum efficiencies of PMTs and their signal pulse shapes are also included. Moreover, potential degradation of mirror reflectivity and therefore decrease of the optical efficiency of the telescopes are taken into account.

Monte-Carlo samples

The Monte-Carlo simulation sample used throughout this work for filling lookup tables and other studies is introduced here. It consists of simulations for a γ-ray point-source with a primary spectrum obeying a power law in energy:$dN/dE \sim \mathrm{E}^{-2}$. The simulations are performed at 11 fixed zenith angles for observation of the source: 0°, 20°, 30°, 40°, 45°, 50°, 55°, 60°, 63°, 65°, and 67°. For each zenith angle, the source is simulated for six different *offset* angles, which are defined as the angular distances between the source direction and telescope pointing direction: 0°, 0.5°, 1.0°, 1.5°, 2.0°, and 2.5°. Simulations with showers originating from the South and the North are also performed for each zenith angle and *offset*. This is important because of the influence of the Earths magnetic field on the shower development in the atmosphere. Another important factor of the detector simulation is the light collection efficiency of the telescope system. Since the reflectivity of mirrors degrades with time as Figure 1.9 shown, the simulated light collection efficiency has to be matched to reality to cope for this aging effect. To compensate the degrading of performance, mirror refurbishment on each telescope

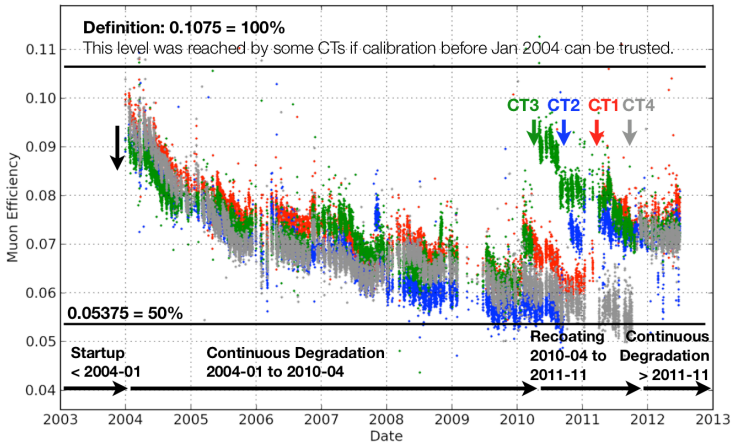

Figure 1.9: The changing of the light collection efficiency with time for each telescope. Taken from [Deil, 2013].

was performed during 2010 and 2011. The refurbishments result in jumps in the light collection efficiency. The light collection efficiency can be inferred by the measurement of the image amplitude of the Čerenkov muon rings. Muon phases are defined as a function of time and used in the Monte-Carlo simulations to deal with the change of the light collection efficiency. The muon phases and the corresponding light collection efficiencies are listed in Table 1.1.

OptConf	Phase	Start	Muon Efficiency				Comment
			CT1	CT2	CT3	CT4	
100	1	2000-01-01	100	100	92.3	100	Brand new
101	1b	2004-05-26	70.2	70.2	70.2	70.2	Degrading
102	1c	2007-07-03	61.5	55.7	61.3	61.6	Degrading
103	1c1	2010-04-27	61.5	55.7	85.6	61.5	CT3 recoated
104	1c2	2010-10-17	61.5	73.2	78.8	61.5	CT2 recoated
105	1c3	2011-04-14	76.0	71.1	75.7	54.5	CT1 recoated
106	1d	2011-11-09	70.2	70.2	70.2	70.2	CT4 recoated

Table 1.1: This table shows the mean light collection efficiency used in Monte-Carlo simulations. The jump in the values for an individual telescope reflects the refurbishment of the mirrors.

Chapter 2

H.E.S.S. data analysis

In this chapter, the analysis method for H.E.S.S. data is introduced. Figure 2.1 summarizes the main steps in the H.E.S.S. data analysis chain. The raw data are taken in the H.E.S.S. site in Namibia and stored on tapes. The raw data are first quality-selected and then the usable data are calibrated through the calibration chain [Aharonian et al., 2004]. After image cleaning and Hillas parameterization, the data are ready for further image analysis. In the analysis chain, the direction and energy of events are reconstructed. Two reconstruction methods following Hillas-type approach [Hillas, 1985; Hofmann et al., 1999] are introduced in this work. After event reconstruction, γ-like events are selected with cuts on shape parameters or with the Multivariate Analysis (MVA) approach. The background level of the remaining events is estimated and then finally, one can make sky maps and spectra of the interested region for morphology and spectral analysis.

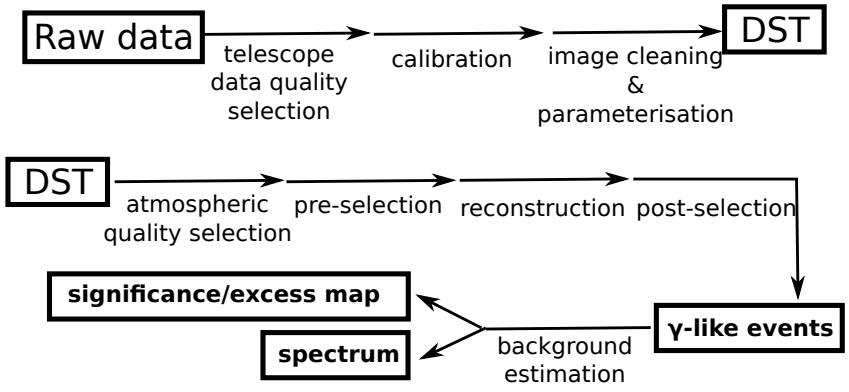

Figure 2.1: A brief summary of the H.E.S.S. data analysis chain.

2.1 Data preparation

Before entering the analysis chain, the data must be pre-processed through several steps: data selection, cleaning and calibration. The calibrated data are then stored in the DST (Data Storage Tapes) for further image analysis. In this section, data preparation is introduced.

Data selection

In the data selection procedure, the raw data has to pass the defined quality criteria to guarantee that the run is taken under stable weather conditions with functioning hardware components. The most important items of these criteria are:

- Cuts on the stability of the system trigger rate to exclude data where clouds passed through the field of view.
- A cut on the absolute system trigger rate to exclude data where the atmospheric transparency is reduced by dust or haze.
- A cut on the number of broken pixels to exclude data where more than 10% pixels are turned off due to bright stars or technical problems. High broken pixel rates may produce artifacts or degrade the reconstruction quality.

Image cleaning

Image cleaning is done by the two-step procedure. In the first step, the so-called tail-cut procedure, a pixel is kept in the image if it achieves one of the following conditions:

- It has an intensity of more than 10 p.e. and a neighbouring pixel with more than 5 p.e..
- It has an intensity of more that 5 p.e. and a neighbouring pixel with more than 10 p.e..

In the second step, the pixels which pass the the above tail cuts but have intensity less than 3σ away from the pedestal RMS are rejected to exclude the ones lighted by the bright stars instead of Čerenkov light.

After this procedure, shower images are parameterized as an ellipse using the Hillas approach [Hillas, 1985]. This approach is motivated by the roughly elliptical shape of the shower images, which is due to the larger longitudinal than lateral extension of the shower. The details of this parameterization are described in the following.

Hillas parameters

Shower images can be characterized by Hillas parameters derived from the two-dimensional intensity distribution of the image. The five Hillas parameters involved in this work are c.o.g., width, length, size, and φ. The definitions of them are described as follows and illustrated in Figure 2.2:

- **c.o.g.**: The first moment of the image intensity distribution yields the center of gravity of the image.
- **length** & **width**: The matrix of second moments can be interpreted as an ellipse around the c.o.g.. Diagonalization of the matrix gives the major and minor axes of the ellipse which are referred to as *Hillas length* and *width*, whose values are the square root of the corresponding eigenvalues.
- **size**: The total intensity of the camera image is referred to as *size*, in units of photo-electrons (p.e.).
- φ: The orientation angle of the ellipse.

2.2 Event reconstruction

As discussed by Hofmann et al. [1999], there are several kinds of algorithms in Hillas-type approach for stereo reconstruction. The most straightforward method is the *Geometrical reconstruction* (Algorithm I), also referred to as *gm* in this work.

2.2.1 Geometrical reconstruction (Algorithm I)

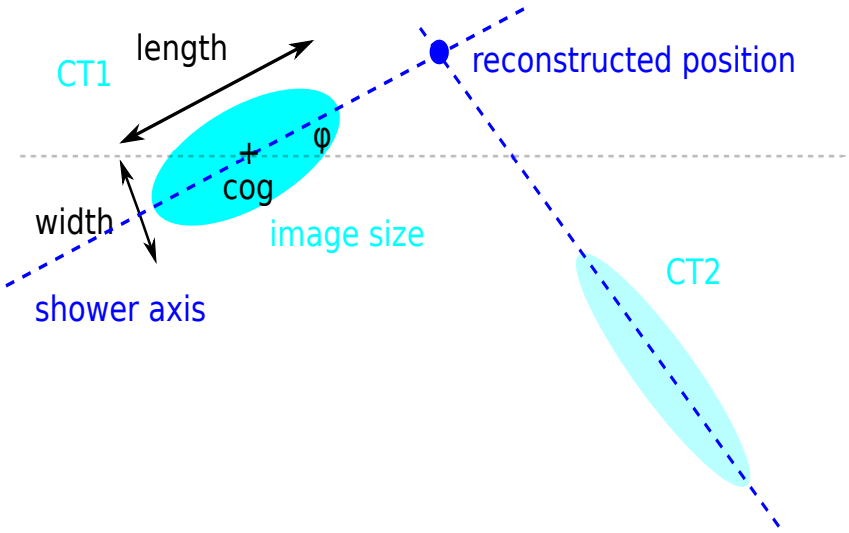

Figure 2.2: Hillas parameters and the *Geometrical reconstruction*(algorithm I).

The advantage of this algorithm is that it is simple and efficient. As shown in Figure 1.6, the major axis of the Hillas ellipse points towards the incident direction of the event. However, there is a left-right ambiguity in the exact direction along the axis. For the mono-reconstruction, one needs the third moment of the Hillas ellipse, namely, *skewness* to break this ambiguity, but for stereo reconstruction, this ambiguity can be easily broken. The schematic diagram for two-image reconstruction is shown in Figure 2.2. The event direction is well determined by the intersection of the two image axes. In case of N telescopes, there are $N(N-1)/2$ intersection points and the event direction is determined by the weighted average. The product of three weighting factors as described below is used to calculate the weighted average for the best estimation of event direction:

- The sine of the angles between the image axes, for taking into account that images with larger stereo angle provide better determination of the shower direction.

- The relative-intensity factor $(\frac{1}{size1} + \frac{1}{size2})^{-1}$, for taking into account that brighter images provides more precise information.
- The ratio of *width* over *length*, $(\frac{width1}{length1} + \frac{width2}{length2})^{-1}$, for taking into account that more elongated images have better defined major axes.

The *core location*, also known as the *impact position*, defined as the intersection of the shower axis with the ground, is reconstructed in a similar way but in an array-wide coordinate system with the telescope positions as the reference. The perpendicular distance between the telescope and shower axis is called the *impact distance*. This parameter combined with *image size* yields the energy of the primary particle. *Geometrical reconstruction* is the standard reconstruction technique used in *hap* (H.E.S.S. Analysis Program) for H.E.S.S. data analysis. It is proved robust and used for most of the H.E.S.S. publication. Nevertheless, the drawback of this reconstruction algorithm is that the weighting factors metioned above do not sufficiently reflect the quality of the images.

2.2.2 Reconsturction by the Disp method (Algorithm III)

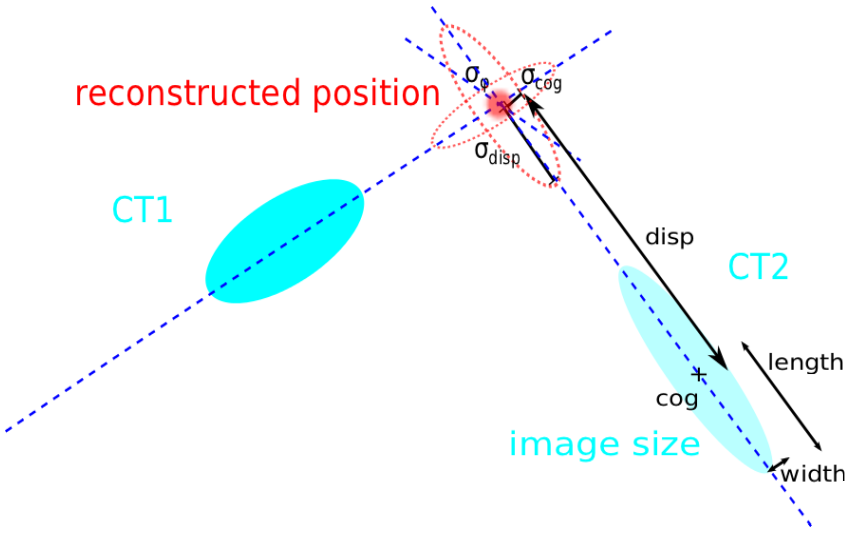

Figure 2.3: Image parameters and the *Disp method* (algorithm III)

As shown in Figure 2.3, the shower image can be represented by its *c.o.g.*, *length*, *width*, *size* and the orientation angle φ. Due to statistical fluctuation in the intensity in each pixel, *c.o.g.* and φ have an uncertainty which can be estimated from the Hillas parameters. One can improve the *Geometrical reconstruction* by introducing the uncertainties of the image parameters (*c.o.g.* and

φ) as a better way of weighting (the Algorithm II in Hofmann et al. [1999]). Even better, the image shape also contains the information about *disp*, the angular distance between the event direction and image *c.o.g.*. The reconstruction method using image uncertainty parameters and *disp* corresponds to the Algorithm III in [Hofmann et al., 1999] and is also called *Disp method*, also referred to as *dm* in this work. This method is frequently used in mono-reconstruction (e.g. for Whipple [Lessard et al., 2001], CT1 in HEGRA [Kranich and Stark, 2003] and MAGIC [Domingo-Santamaria et al., 2005]) and is also being developed for mono-reconstruction for H.E.S.S. II. CT5 telescope.

Experimentally, the uncertainty of *c.o.g.* along the minor axis , σ_{cog} has a dependency on $\ln(size)$ and $width$, and the uncertainty of φ, σ_φ has a dependency on $\ln(size)$ and $width/length$. *Disp* can be estimated by the ellipticity defined as $(1 - width/length)$ as proposed by Fomin et al. [1994] since a shower with a larger *disp* has a more elongated image. In the work mentioned above, analytical formula containing $width/length$ and $\ln(size)$ are used for the estimation of *disp*. In this work, however, $length$ and $\ln(size)$ are found to be better parameters. Instead of analytical formulae, lookup tables generated from Monte-Carlo simulations are used to obtain more precisely the image uncertainty parameters and *disp*.

Event direction predictor of a single telescope

After getting the image uncertainty parameters from the lookups, one can combine them together to calculate the event direction predictor P_i of the ith telescope. The coordinate transformation involved in the calculation is shown in Figure 2.4. The error ellipse representing the image uncertainty parameters is defined in the uv frame where u-axis and v-axis are aligned to the major and minor axes of Hillas ellipse of the individual telescope image. For combining the error ellipses in all telescope images, coordinate transformation to one unique coordinate, the nominal frame here, is desired. Let xy be the *nominal frame* with the pointing direction as the origin, $d \equiv disp$ and (x_0, y_0) be the position of c.o.g.. P_i is calculated by:

$$P_i = \begin{pmatrix} P_x \\ P_y \end{pmatrix} = \begin{pmatrix} d\cos\varphi + x_0 \\ d\sin\varphi + y_0 \end{pmatrix}. \tag{2.1}$$

The uv frame is rotated from the xy frame by φ degrees. The coordinate transformation from the uv frame to the xy frame is:

$$\begin{pmatrix} x \\ y \end{pmatrix} = \begin{pmatrix} \cos\varphi & -\sin\varphi \\ \sin\varphi & \cos\varphi \end{pmatrix} \begin{pmatrix} u \\ v \end{pmatrix}. \tag{2.2}$$

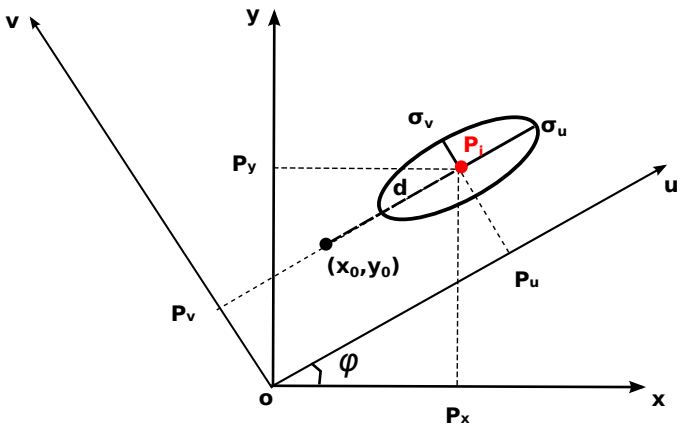

Figure 2.4: Coordinate transformation for calculating the covariance matrix of single event direction predictor.

$P_i = (P_u, P_v)$ in the uv frame is transformed to $P_i = (P_x, P_y)$ in the xy frame by:

$$P_x = P_u \cos\varphi - P_v \sin\varphi \tag{2.3}$$
$$P_y = P_u \sin\varphi + P_v \cos\varphi, \tag{2.4}$$

Let $\sigma^2[P_u]$ and $\sigma^2[P_v]$ be the errors along the u and v direction and let $\sigma_u \equiv \sigma_{disp}$, $\sigma_v \equiv \sigma_{cog}$, and σ_φ being the uncertainty of φ, then:

$$\sigma^2[P_u] = \sigma_u^2 \tag{2.5}$$
$$\sigma^2[P_v] = \sigma_v^2 + d^2 \sin^2\sigma_\varphi, \tag{2.6}$$

Let $\mathbf{C_{i,xy}}$ be the covariance matrix of $\mathbf{P_i}$ in the xy frame:

$$\mathbf{C_{i,xy}} = \begin{pmatrix} \sigma_x^2 & \sigma_{xy} \\ \sigma_{xy} & \sigma_y^2 \end{pmatrix}. \tag{2.7}$$

Each element of $\mathbf{C_{i,xy}}$ is calculated by the coordinate transformation from the uv frame to xy frame:

$$\sigma_x^2 = \sigma^2[P_u]\cos^2\varphi + \sigma^2[P_v]\sin^2\varphi \tag{2.8}$$
$$\sigma_{xy} = \cos\varphi\sin\varphi\left(\sigma^2[P_u] - \sigma^2[P_v]\right) \tag{2.9}$$
$$\sigma_y^2 = \sigma^2[P_u]\sin^2\varphi + \sigma^2[P_v]\cos^2\varphi, \tag{2.10}$$

The averaged event direction and its uncertainty

With the event direction predictor and the associated covariance matrix for each participating telescope, one can calculate the averaged event direction by:

$$\mathbf{P} = \mathbf{C} \sum_{\mathbf{i=1}}^{\mathbf{n_{tel}}} \mathbf{C_{i,xy}^{-1}} \mathbf{P_i}, \tag{2.11}$$

where the *ith* source position predictor, $\mathbf{P_i}$ is as expressed in Eq. (2.1) and the associated weighting factor $\mathbf{C_{i,xy}}$ is as expressed in Eq. (2.7). The covariance matrix $\mathbf{C}$ associated with $\mathbf{P}$ is calculated by:

$$\mathbf{C} = \frac{\mathbf{1}}{\mathbf{D}} \sum_{\mathbf{i=1}}^{\mathbf{n_{tel}}} \frac{\mathbf{C_{i,xy}}}{|\mathbf{C_{i,xy}}|}, \tag{2.12}$$

with $\mathbf{D}$:

$$\mathbf{D} = \sum_{\mathbf{i=1}}^{\mathbf{n_{tel}}} \frac{\sigma_{\mathbf{i,x}}^{\mathbf{2}}}{|\mathbf{C_i}|} \sum_{\mathbf{i=1}}^{\mathbf{n_{tel}}} \frac{\sigma_{\mathbf{i,y}}^{\mathbf{2}}}{|\mathbf{C_i}|} - \left(\sum_{\mathbf{i=1}}^{\mathbf{n_{tel}}} \frac{\sigma_{\mathbf{i,xy}}}{|\mathbf{C_i}|} \right)^{\mathbf{2}}. \tag{2.13}$$

The combined covariance matrix $\mathbf{C}$ can also be represented as an error ellipse. After diagonalization, the eigenvalues σ_j and σ_k correspond to the half length of major and minor axes. The error σ_P of the weighted average event direction is thus:

$$\sigma_P = \sqrt{\sigma_j^2 + \sigma_k^2}. \tag{2.14}$$

Parameter lookup tables

All the lookups are filled with different muon phases, azimuth angles, and zenith angles because Hillas parameters of the same shower change with these observation parameters:

- Muon phase: The reflectivity of the telescope mirrors vary with time. It directly affects the recorded *image size* under the same Čerenkov light intensity. Simulations with 6 muon phases as shown in Table 1.1 are used for filling the lookups.

- Azimuth angle: Shower development is affected by the geomagnetic field of the earth so the observation azimuth angle has to be taken into account. Simulations with 2 azimuth angles, to the north and the south, are used in filling the lookups.

- Zenith angle: As discussed in Section 1.2, the lateral Čerenkov distribution and the light-pool radius depend on the zenith angle so the observation

zenith angle has to be taken into account. Simulations with 11 zenith angles as listed in Section 1.4.3 are used.

The involved observation parameters and layout of the lookups are listed in Table 2.1. Lookups for *disp* and σ_{disp} have one extra parameter: *impact distance*. The reason for this is explained in the following.

In Figure 2.5(a), one can see that *disp* is roughly proportional to *length* for smaller *disp* values. From a certain point, however, *length* stops growing with increasing *disp*. This can be more clearly seen in Figure 2.5(b). This plot shows the mean value of length with the error bar denoting the spread of it. The maximal mean length appears at $disp \sim 30\,\mathrm{mrad}$ and starts to decline. This phenomenon is due to the truncation on the image by the limited read-out window and camera edge.

The read-out window for H.E.S.S. telescopes is fixed to 16 ns. When the arriving time spread on the focal plane of a shower is larger than this value, the part of the shower beyond the read-out window is not recorded. Because H.E.S.S. cameras do not record the timing information of a shower, it is difficult to distinguish whether a shower is truncated or not. Some of the images truncated by the camera edge are rejected by the local-distance cut which gets rid of images with c.o.g. falling $> 2^\circ$ away off the camera center. Nevertheless, this cut does not reject all the truncated images because for some cases the position of c.o.g. is also severely shifted due to the image truncation.

To cope with these two effects, *impact distance* is needed for *disp* and σ_{disp} lookup tables. The lookup tables are filled with the true *impact distance* of Monte-Carlo simulated events. The boundaries for filling the small- and large-impact-distance lookup tables are chosen experientially by the following procedure. Figure 2.5(b) suggests the truncation effect gets involved around the turning point where the *length* stops growing with the *disp*. For this case, it happens at $disp \sim 30\,\mathrm{mrad}$. Figure 2.6 shows the *impact distance* distribution for $disp \sim 30\,\mathrm{mrad}$. The boundaries of the two lookup tables are chosen as (the mode of the distribution $\pm$ the rms) as denoted by the dashed lines. Figure 2.7(a) and 2.7(b) shows the *length-disp* correlation for the events with *impact distance* smaller than the lower boundary and larger than the upper boundary. One can see that these boundaries quite nicely separate the untruncated and truncated events. For large *impact distance length* has a negative correlation with *disp* while for small *impact distance* it is a positive correlation.

In practice, the events with *impact distance* larger (smaller) than the upper (lower) boundary will take *disp* values from the large (small) *impact distance* lookup table, and the events with *impact distance* in between will take the values by linear interpolation.

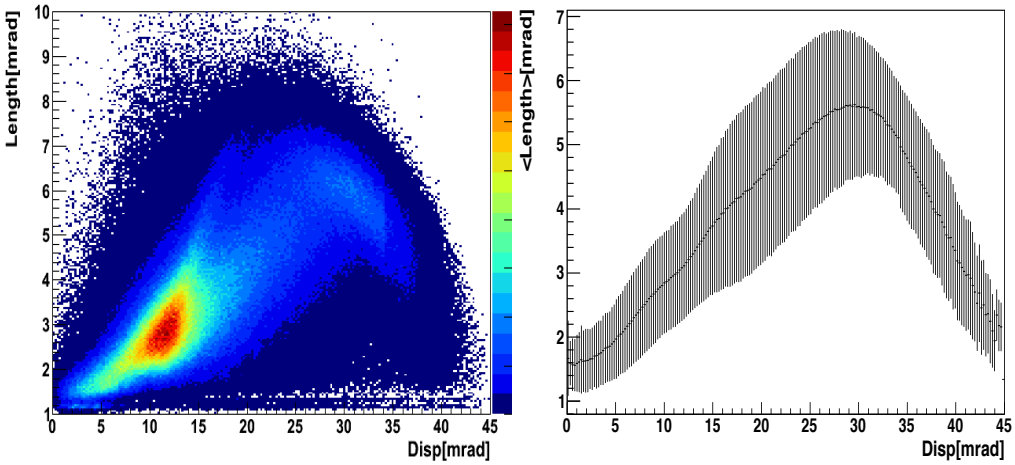

(a) (b)

Figure 2.5: (a) Correlation between *disp* and *length*. (b) The profile of the average *length* versus *disp*.

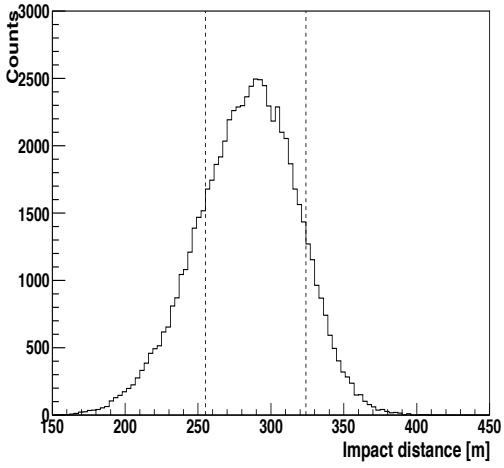

Figure 2.6: Distribution of the *impact distance* for $disp \sim 30$ mrad. The dashed lines denotes the boundaries for the lookup tables.

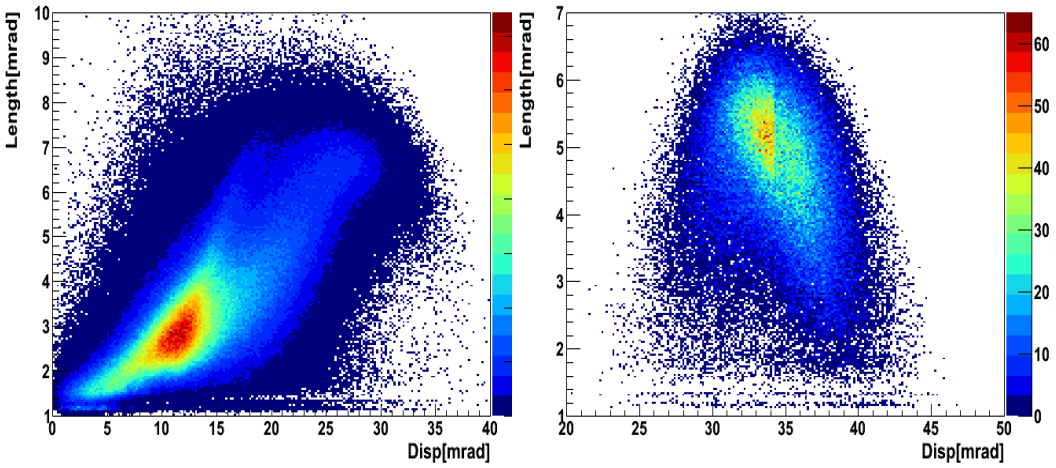

(a) (b)

Figure 2.7: (a) Relation between *disp* and *length* for small *impact distance* where the images are not truncated by the read-out window. One can see that *disp* is roughly proportional to *length*. (b) Relation between *disp* and *length* for large *impact distance* where the images are truncated by the read-out window. For these cases, *disp* is not proportional to *length*.

histogram	**parameters**	**x-axis**	**y-axis**	**z-axis**
disp	muon,azm,zen,impact	ln(size/p.e.)	length	disp/mrad
σ_{disp}	muon,azm,zen,impact	ln(size/p.e.)	length	disp/mrad
σ_{cog}	muon,azm,zen	ln(size/p.e.)	width	σ_{cog}/mrad
σ_{φ}	muon,azm,zen	ln(size/p.e.)	width/length	σ_{φ}/rad
$\mathrm{impact}_{\mathrm{new}}$	muon,azm,zen	$\mathrm{disp}_{\mathrm{true}}$	$\hat{\mathrm{H}}_{\mathrm{max}}$	$\mathrm{impact}_{\mathrm{new}}$/m

Table 2.1: The layout of the error parameter lookups used in the *Disp method*. Here muon, azm, and zen are the abbreviation of muon efficiency phase, azimuth angle and zenith angle. The *disp* and σ_{disp} lookups have one extra parameter, *impact*, which is the *impact distance* reconstructed by the *Geometrical reconstruction*, to cope with the truncation of the shower image at large *impact distance*. $Impact_{new}$ is used in the *Disp method* to reconstruct the *core location*. $\hat{H}_{\mathrm{max}}$ which stands for H_{max}-estimator, is the ratio of *impact distance* over *disp* reconstructed by the *Geometrical reconstruction*.

For the reconstruction of *impact distance* and *core location*, the H_{max} estimator, $\hat{H}_{\mathrm{max}}$ is used as a parameter in the lookups. As shown in Figure 1.4, H_{max} is approximately the ratio of *impact distance* over *disp*. $\hat{H}_{\mathrm{max}}$ is calculated by the *impact distance* and *disp* from the *Geometrical reconstruction* and combined with *disp* from the *Disp Method* to give the new *impact distance*.

Figure 2.8 shows the whole set of lookups for muon-phase 100 at zenith. One can see that the uncertainties of all parameters in principle decrease with *image size*. σ_{cog} increases with *width* and σ_{φ} increases with *width/length*. *Disp* increases with *length* and σ_{disp} peaks at moderate lengths.

In practice, the azimuth angle, zenith angle, and *impact distance* reconstructed by the *Geometrical reconstruction* are used for looking up the value of the desired variable for real events. Since the lookups are sampled with discrete values of the parameters, linear interpolation is needed. Let $A_1 \pm \sigma_1$ and $A_2 \pm \sigma_2$ be two lookup values with their respective uncertainties, and c_1 and c_2 be the corresponding parameters, the desired value A is calculated by

$$A = \frac{c - c_1}{c_2 - c_1} A_2 + \frac{c_2 - c}{c_2 - c_1} A_1. \tag{2.15}$$

By assuming that the variables follow Gaussian distributions, the uncertainty of A, σ_A is calculated by

$$\sigma_A = \sqrt{\frac{\sigma_1^2 (c_2 - c)^2 + \sigma_2^2 (c - c_1)^2}{(c1 - c2)^2}}. \tag{2.16}$$

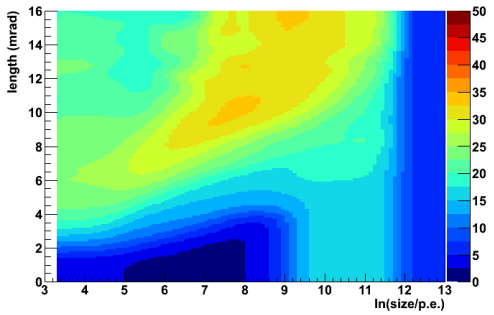

(a) Lookup for *disp* at small *impact distance*

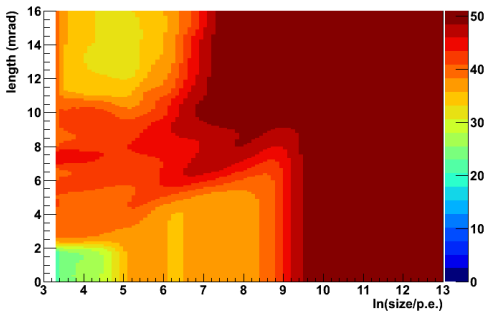

(b) Lookup for *disp* at large *impact distance*

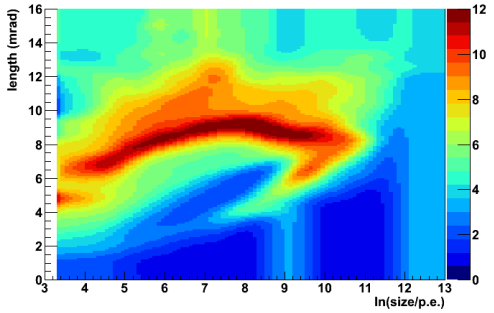

(c) Lookup for σ_{disp} at small *impact distance*

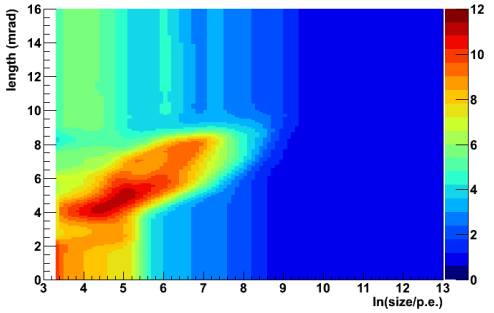

(d) Lookup for σ_{disp} at large *impact distance*

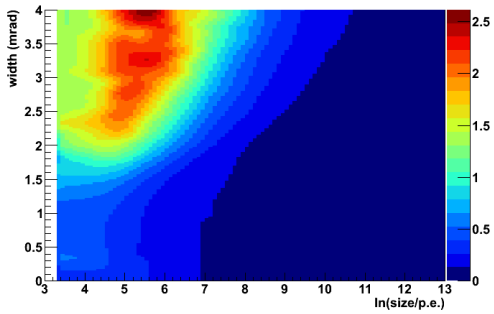

(e) Lookup for σ_{cog}

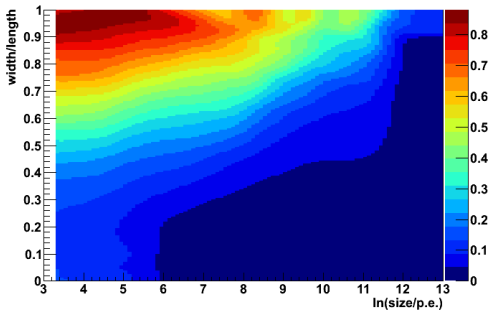

(f) Lookup for σ_{φ}

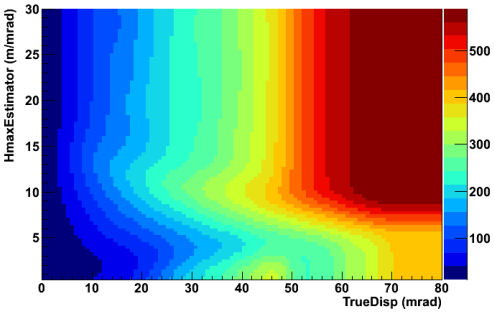

(g) Lookup for *impact distance*

Figure 2.8: Lookup tables for the error parameters, *disp*, and *impact distance*.

2.3 Event selection and γ-hadron separation

The event selection in the H.E.S.S. data analysis chain contains two steps: *pre-selection* and *post-selection*. *Pre-selection* is applied before event reconstruction to ensure that the images of input events have a reasonable quality for Hillas parameterization. *Pre-selection* contains two cuts, the *local-distance cut* and *image size cut*:

- **local-distance cut**: The local distance is defined as the angular distance between the image *c.o.g.* and the camera center. The field of view of the H.E.S.S. I camera has a radius of 2.5°. A *local-distance cut* at 2° is applied to exclude the images truncated by the camera edge.

- **size cut**: This cut defines the lowest threshold on the total image intensity. In principle, images with higher intensity have better quality for Hillas parameterization and yield better reconstruction. However, a stricter *size cut* means lower γ-ray acceptance. To reach the compromise between the reconstruction quality and γ-ray acceptance, different *size cut* values are defined in configurations optimized for different types of sources with assumed spectrum indices and strengths. The details of these will be introduced in 3.1.

Images passing *pre-selection* are then used in the reconstruction chain for reconstructing the direction and energy of events. Only events with two or more images passing *pre-selection* are processed. This requirement reduces γ-ray acceptance but increases hadron separation power and improves reconstruction quality. As the flux of hadronic background is a factor of $\mathcal{O}(10^4)$ larger than the γ-ray flux of the strongest known γ-ray source, *post-selection* is needed after reconstruction to suppress the background level.

2.3.1 Shower shape parameters

As discussed in Section 1.1.3, the lateral extension of hadronic showers is usually wider and less symmetric than that of γ-ray showers. These characteristics can also be seen in shower images. Figure 2.9 shows the images for a 1 TeV γ-ray event and a 2.3 TeV proton event. One can clearly see that the proton-induced image is more irregular and less elliptical. This results in poor Hillas parameterization which can be used to reject the background events. As proposed in [Hillas, 1985], using cuts on *width* and *length* is a common method for hadron suppression. The shape of shower images are found being dependent on the *impact distance* and *image size*. To make use of shower shape parameters more efficiently, *mean reduced scaled width* (*MRSW*) and *mean reduced scaled length* (*MRSL*) are introduced.

For an image of given *impact distance*, *size*, *offset*[1], zenith angle, azimuth angle and muon efficiency, its *width* and *length* are compared to the mean value as expected from γ-ray Monte-Carlo simulations. The difference between the measured value $width_i$ and the expected value $\langle width \rangle_{\gamma,i}$ scaled by the spread $\sigma_{\gamma,i}$ of the simulated distribution yields the *reduced scaled width* (RSW) and *reduced scaled length* (RSL). From which, $MRSW$ is calculated by averaging RSW over every participating telescope with a weighting factor $w_i = (\langle width \rangle_{\gamma,i} / \sigma_{\gamma,i})^2$:

$$MRSW = \frac{1}{\sum_{i=1}^{N_{\mathrm{tel}}} w_i} \sum_{i=1}^{N_{\mathrm{tel}}} \left(\frac{width_i - \langle width \rangle_{\gamma,i}}{\sigma_{\gamma,i}} \right) \cdot w_i. \tag{2.17}$$

$MRSL$ is also calculated in the same way. The distributions of $MRSW$ and $MRSL$ for simulated γ-ray and *off-run*[2] events are shown in the first two panels of Figure 2.10. One can see that these two shape parameters have quite strong hadron separation power. In the H.E.S.S. standard analysis, cuts on $MRSW$ and $MRSL$ in *post-selection* are used for $\gamma-$like event selection.

2.3.2 Other parameters with hadron suppression power

Although cutting on the shape parameters is a standard approach in IACT for background suppression, this method does not sufficiently use the information from shower images. Besides $MRSW$ and $MRSL$, there are several other parameters with hadron suppression potential: $MRSWO$, $MRSLO$, X_{max}, and $\Delta E/E$. Their definition and characteristics are discussed as follows:

- $MRSWO$ amd $MRSLO$: The definition of $MRSWO$ and $MRSLO$ is similar to $MRSW$ and $MRSL$:

$$MRSWO = \frac{1}{\sum_{i=1}^{N_{\mathrm{tel}}} w_i} \sum_{i=1}^{N_{\mathrm{tel}}} \left(\frac{width_i - \langle width \rangle_{\mathrm{off,i}}}{\sigma_{\mathrm{off,i}}} \right) \cdot w_i, \tag{2.18}$$

  where $\langle width \rangle_{\mathrm{off,i}}$ and $\sigma_{\mathrm{off,i}}$ are the mean and spread of *width* expected from *off data*, and w_i is a weighting factor defined as $w_i = (\langle width \rangle_{\mathrm{off,i}} / \sigma_{\mathrm{off,i}})^2$. One can see in Figure 2.11 that these two parameters provide separability

[1] The offset is defined as the angular distance between the event direction and pointing direction

[2] *Off runs* are observation runs pointing to a direction where there is no known γ-ray emitter in the field of view.

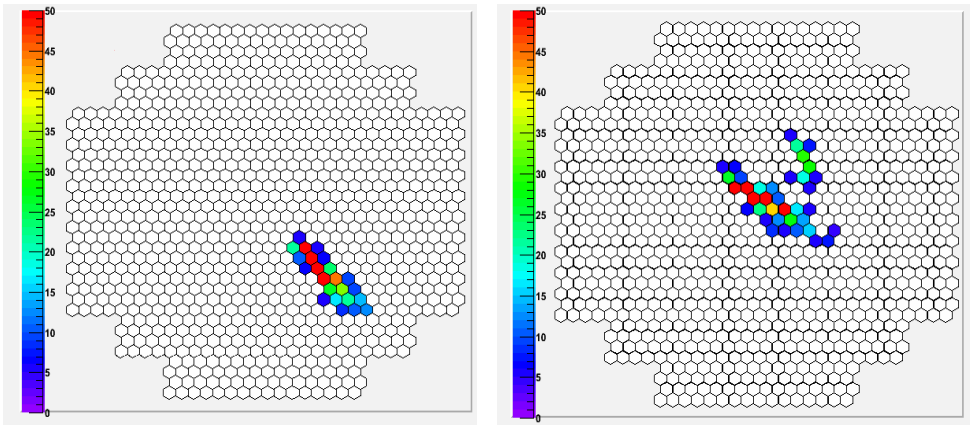

(a) (b)

Figure 2.9: (a) The camera image of a 1 TeV γ-ray event at the *array impact distance*[1] of 221 m after image cleaning. (b) The camera image of a 2 TeV proton event at the *array impact distance* of 232 m after image cleaning. One can clearly see that the proton image is less elliptical and has a multi-core structure.

of γ-rays and hadrons of a given *image size*. This separability increases with *size* since the difference in $\langle width \rangle$ for γ rays and hadrons gets larger with increasing *size*.

- $X_{\max}$: As mentioned in Section 1.1.3, hadronic showers in the TeV regime penetrate typically deeper into the atmosphere and have a larger $X_{\max}$ than γ-ray showers due to the larger radiation length of hadrons. In addition, the complex structure of hadronic showers results in irregular image shapes and ill-defined Hillas parameters which yield bad reconstruction of $X_{\max}$. The $X_{\max}$ distribution of hadronic showers thus has larger spread, and in some cases when $X_{\max}$ is very badly reconstructed, the value of $X_{\max}$ is close to 0.

- $\Delta E/E$: ΔE is the *sample standard deviation* of the energies of all participating telescopes:

$$\Delta E = \sqrt{\frac{1}{n_{\text{tel}} - 1}\left(\sum_{i=1}^{n_{\text{tel}}} E^2 - \frac{1}{n_{\text{tel}}}\left(\sum_{i=1}^{n_{\text{tel}}} E\right)^2\right)} \tag{2.19}$$

The irregularity and asymmetry of hadronic showers yield different Čerenkov light distribution at different viewing angles. This is directly translated to

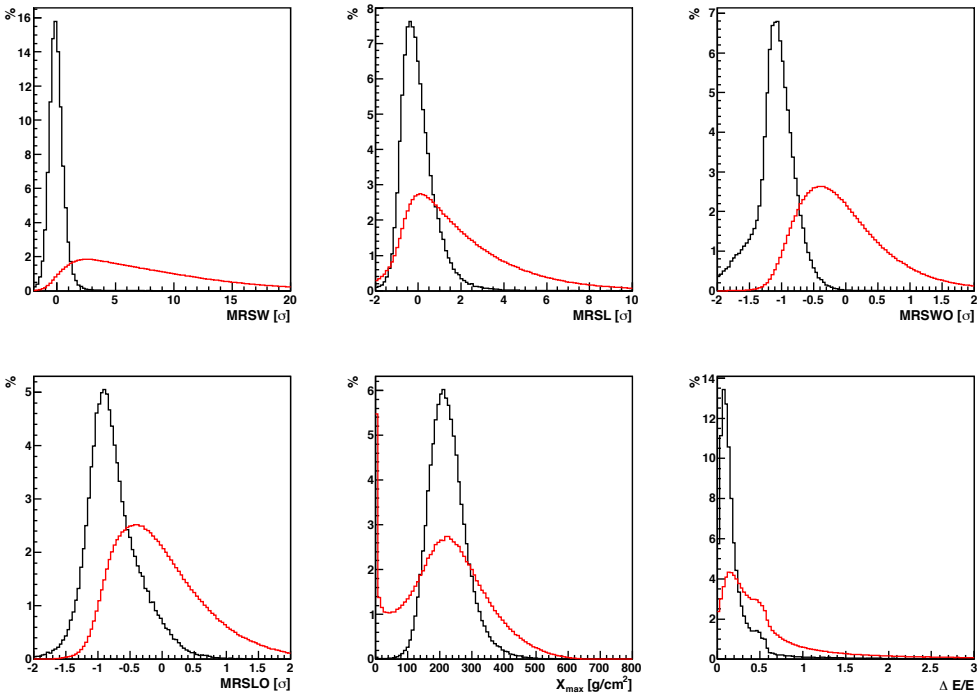

Figure 2.10: Distributions of parameters with hadron suppression power. The black lines are the distributions for Monte-Carlo simulation γ-rays at 30° zenith angle and 0.5° offset, and the red lines are for hadron events from *Off data* in the zenith angle range $25° - 35°$.

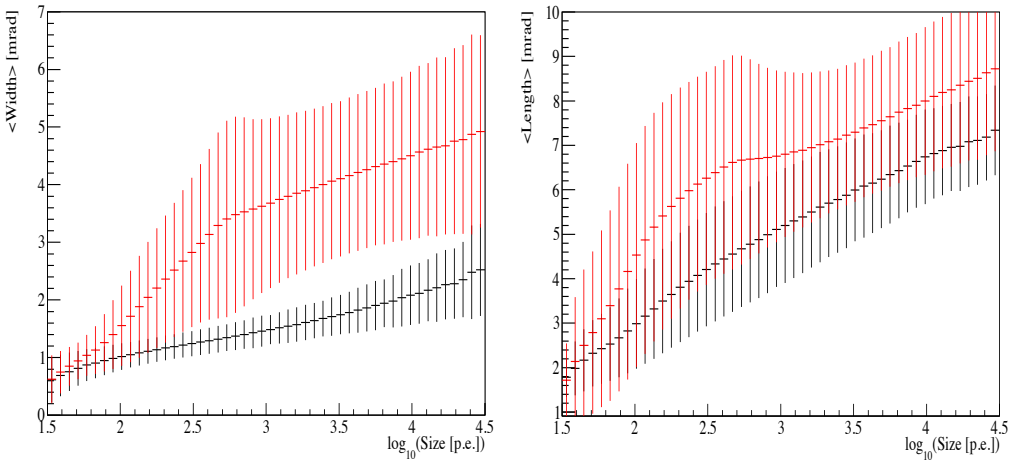

(a) (b)

Figure 2.11: Profiles of (a) *width* versus $\log_{10}(size)$ and (b) *length* versus $\log_{10}(size)$ of Monte-Carlo γ rays (black) and *off data* (red) at 30° zenith angle and 0.5° offset. The error bars here denote the spread of the parameter.

image size and results in large spread in the reconstructed energies for each telescope, so the $\Delta E/E$ distribution of hadron events is wider than that of γray events.

2.3.3 Multivariate analysis technique for γ-hadron separation

The distributions of the six mentioned parameters for Monte-Carlo simulated γ rays and *off data* are shown in Figure 2.10. It can be cearly seen that all parameters provide γ-hadron separation potential. Because of the complex correlation between the parameters, the simple box-cut (e.g. cutting on a range of *MRSW* and *MRSL*.) is not the optimal way for γ-like event selection. A more sophisticated method is desired to efficiently use these parameters. The multivariate analysis (MVA) technique is commonly used in natural sciences and sociology for complex problems. The software package TMVA [Hoecker et al., 2007] contains several MVA algorithms. Among them, the method of Boosted Decision Trees is used in this work.

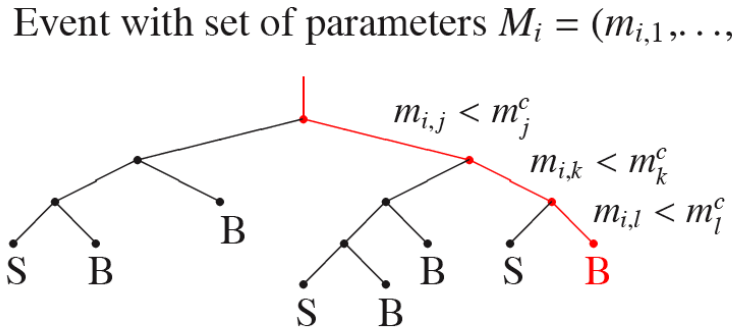

Figure 2.12: Diagram of a decision tree. An event's parameters are compared with the split criterion at each node until it ends in a *leaf*, marked as signal (S) or background (B). Taken from [Ohm, 2010].

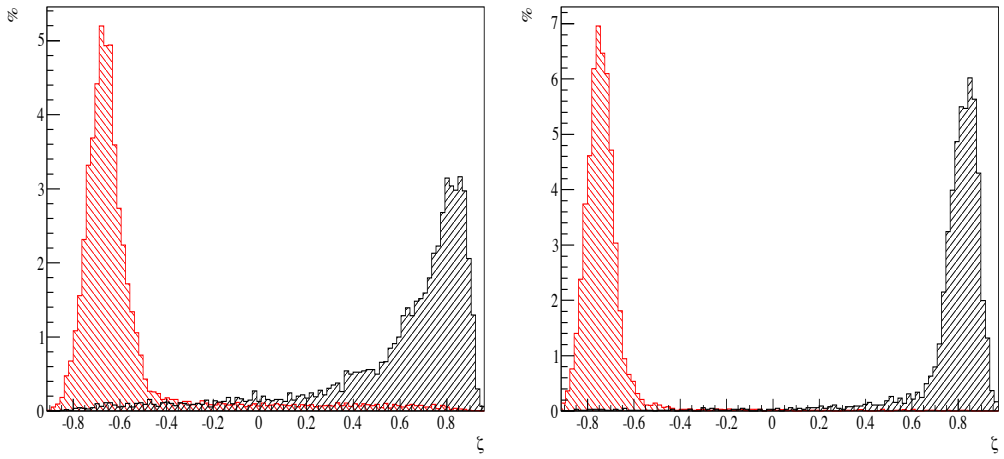

(a) (b)

Figure 2.13: (a) ζ distribution for the lowest energy band $0.1 - 0.3\,\mathrm{TeV}$ at 30° zenith angle. (b) ζ distribution for the highest energy band $5.0 - 100.0\,\mathrm{TeV}$ at 30° zenith angle. The red shaded areas denotes the distribution for *off data* and the black shaded area denotes the distribution for Monte-Carlo simulated γ rays.

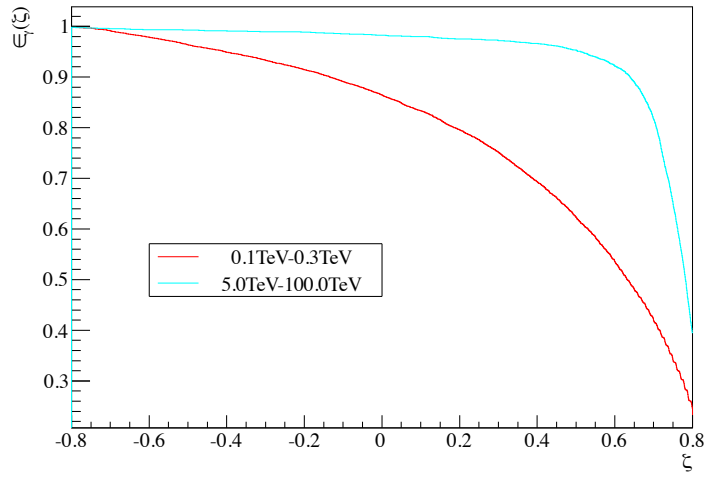

Figure 2.14: Relation between $\epsilon_\gamma(\zeta)$ and ζ for the lowest energy band $0.1 - 0.3\,\mathrm{TeV}$ and highest energy band $5.0 - 100.0\,\mathrm{TeV}$ at 30° zenith angle.

Decision Trees

The schematic diagram of a decision tree is shown in Figure 2.12. A decision tree is composed of layers of branches and leaves labeled with **S** and **B** at the very end. Consider an event with a set of parameters $(m_{i,1}...m_{i,6})$ is put into the decision tree. At each node, one of the parameters is compared to the binary split criterion m_j^c. Depending on whether passing the criterion or not, this events is thrown into the corresponding branches. After several branchings, the event ends up in a leaf and is classified as signal-like or background-like. To optimize the split criteria, the tree is trained with a sample of events with known types. To reduce statistical fluctuations and achieve a stable performance, a forest of decision trees is used. The number of trees is chosen to be 200 in this work as a good compromise between separation performance and reasonable computing time. The single tree is extended to a forest of trees through the *AdaBoost* procedure [Freund and Schapire, 1997]. In this procedure, misclassified events in the current tree are given a higher weight in the training of the next tree. Compared with using a random sample of the data to train the trees, this method focuses on the most difficult cases and makes the learning for classification more efficient.

Training sample

The six parameters (*MRSW*, *MRSL*, *MRSWO*, *MRSLO*, X_{max}, and $\Delta E/E$) metioned in Section 2.3.1 and 2.3.2 are used as classifying variables for training.

The training sample contains signal events from Monte-Carlo γ-ray simulations and background events from *Off data*. As discussed in [Ohm, 2010], these variables are more or less energy and zenith-angle dependent. Therefore, the training is processed in energy and zenith angle bands to achieve a stable performance.

BDT response

All trees in the forest have different criteria and the final response is calculated as the weighted mean vote of the classification of all single trees. The value of mean vote is referred to as ζ which gives an evaluation of background- or signal-likeliness of an event. The ζ distributions of the test signal and background samples are shown in Figure 2.13. One can see that events with $\zeta \sim -1$ are more background-like and with $\zeta \sim 1$ are more signal-like. For a given zenith angle, the distributions of ζ show strong dependency on energy. For the higher-energy band, the spread of the distributions is narrower than those for the lower-energy band. The mean values of the distributions also shift away from each other for the higher-energy band. This means that the fraction of misclassified events changes with the energy. For lower-energy, the amounts of misclassified events increase. This behavior is expected since the intensity fluctuations in the low-energy-event images are more pronounced. The change of ζ distribution results in different ζ cuts for varying zenith angle and energy for a desired γ efficiency. To avoid this complexity, the ζ dependent γ-efficiency, $\epsilon_\gamma(\zeta)$, is introduced. Figure 2.14 shows the conversion to ζ from a given $\epsilon_\gamma(\zeta)$ for the lowest and highest energy bands. Cutting on a value of $\epsilon_\gamma(\zeta)$ yields the corresponding cuts on ζ for different energy bands under a fixed γ efficiency. One can see that for a given $\epsilon_\gamma(\zeta)$, the corresponding ζ of the highest energy band is larger than that of the lowest energy band which yields better γ-hadron separability.

2.4 Background estimation and signal extraction

After *post-selection*, the remaining events still contain a few γ-like background events which can not be completely excluded. To extract the γ-ray signal from a certain position (*On-region*) on the sky, one has to estimate the background component at this position from the *Off-region*. Depending on different purposes, several methods are developed for background estimation. In this work, the *ring-background* method is used to generate the sky map for morphology studies and the *reflected-background* method is used for spectral analysis.

2.4.1 Background estimation

Ring background method

This method is illustrated in the left panel of Figure 2.15. The *Off-region* is defined as a ring centered at the target position (*On-region*). Its inner radius is chosen much larger than that of the *On-region* to avoid contamination from the signal. Its area is also set much larger than that of the *On-region* to increase the statistics of the background. Since the *On* and *Off-region* have different offsets to the pointing position (camera center), the acceptance in each region is different from each other and energy-dependent. The normalization factor α (defined in Eq. (2.21) has to be calculated with acceptance correction. The *Ring-background* method can be used to estimate the background of each point in the field of view for generating 2D sky maps for morphology studies. However, it is not suitable for spectral analysis because it is difficult to calculate the energy-dependent acceptance in the *On-* and *Off-* region.

Reflected background method

As shown in the right panel of Figure 2.15, in *Reflected background* method, the *Off-regions* are defined as a series of circles with the same radius at the same offset from the pointing direction as the *On-region*. Since there is no reflected circle when the target overlaps with the pointing direction, to use *Reflected-background* method, the observation has to be performed in the so-called *wobble mode*, where the pointing direction has a pre-determined offset[1] to the target position. Because the camera acceptance is roughly radially symmetric, all *Off-regions* have the same background acceptance as the *On-region*. This property

[1]The wobble offset used in H.E.S.S. observation dedicated to a certain target is usually a value between 0.5° to 1.0°.

makes this method ideal for spectral analysis. For this method, the normalization factor α is merely the ratio of the number of *On-* and *Off-regions*.

***On-off background* method**

This method is useful for extended sources with more than 1° extension. In these cases, *Ring-background* and *Reflected-background* method may not work because the on-region is too large. The ideal way of applying the *On-off background* method is to take the data in the classical *On-off mode* as first proposed for the Whipple experiment [Weekes et al., 1989]. This observation mode is not the standard observation mode for H.E.S.S. so most observation runs do not have dedicated background runs. Nevertheless, the characteristics of H.E.S.S. background was investigated in [Glueck, 2011]. A method of matching *On-off* run pairs for different observation conditions was proposed, with off runs taken from observations of targets which did not show significant γ-ray excess. This study makes it possible to find a paired *Off* run for a *wobble-mode* run.

***Template background* method**

Instead of using different regions in the sky map, this method estimate the background using the scaled parameter MRSW. Events falling in the *On-region* are assigned to the signal regime (N_{On}) if they pass the γ-selection cut and to the background regime (N_{Off}) if they pass the background-selection cut. The MRSW distribution of both kinds of events and the corresponding selection regions are shown in Figure 2.16. The relative acceptance for background and signal is required to calculate the normalization factor α and is calculated from lookup tables. This method is suitable for the morphology study of extended sources where the *On-region* is so large that the *Off-region* for *Ring-background* method falls near the edge of the field of view where the systematic uncertainties on acceptance increases. However, it is not suitable for spectral analysis since the events in the background regime have different estimated energy from those in the signal regime.

2.4.2 Signal extraction with the likelihood ratio method

With the estimated background, the VHE γ-ray excess is calculated as

$$N_{\gamma} = N_{\mathrm{On}} - \alpha \cdot N_{\mathrm{Off}}, \tag{2.20}$$

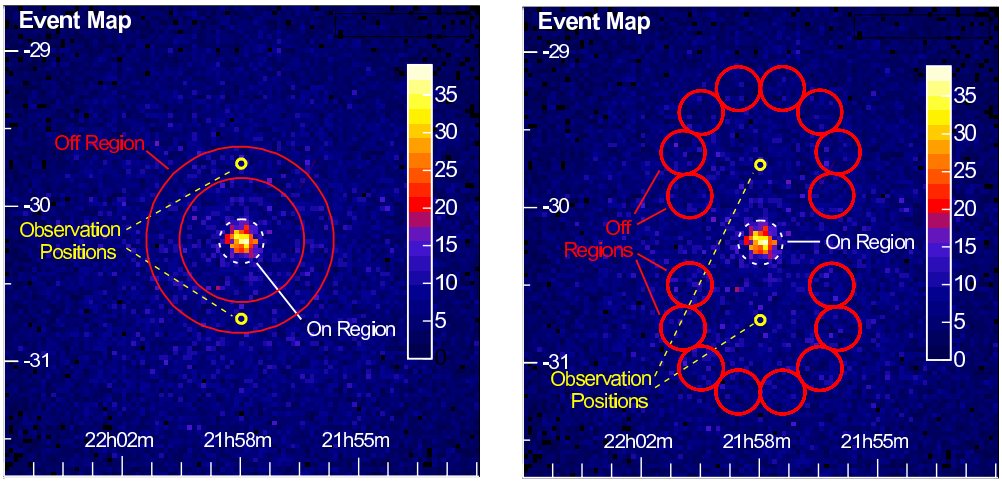

Figure 2.15: Shown is the VHE γ-ray count map without background subtraction for five-hour H.E.S.S. observation on the active galactic nuclei PKS 2155-304, which is one of the strongest VHE γ-ray emitters on the sky. The *Ring-background* method is illustrated in the left panel and the *Reflected-background* method is illustrated on the right panel. The observation is done in *wobble mode*. The yellow circles donate the observation pointing position at a given wobble offset from the target position (*On-region*). The red lines denote the *Off-regions*. For the *Ring-background* method, the *Off-region* is a ring centered at the target position with a defined radius and thickness, while for the *Reflected-background* method, it is a set of circles with the same radius at the same offset from the pointing position as the *On-region*. Taken from [Berge et al., 2007].

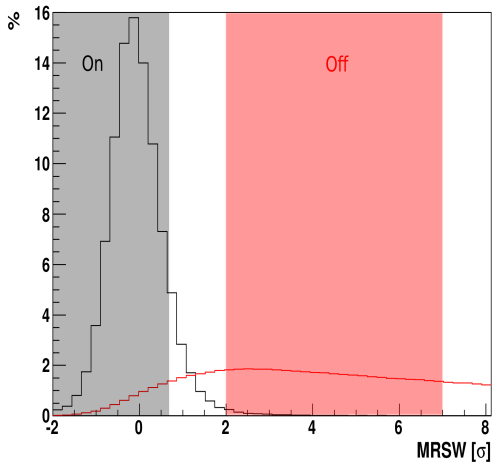

Figure 2.16: The *On-* and *Off-* regimes in the MRSW space for template background method.

where $N_{\rm On}$ and $N_{\rm Off}$ are the number of events in the *On-region* and *Off-region* and α is a normalization factor accounting for the geometrical areas and acceptance:

$$\alpha = A_{on}/A_{\rm off}, \tag{2.21}$$

with A_{on} and $A_{\rm off}$ as the area of *On-region* and *Off-region* after acceptance correction. To establish the reliability of a signal and estimate the probability that it's not due to the background fluctuation, the excess has to be compared with the uncertainties of signal and background level. By assuming $N_{\rm On}$ and $N_{\rm Off}$ follows a Poisson distribution, one can define the significance of the signal, S, as the ratio of the excess counts to its uncertainty:

$$S = \frac{N_\gamma}{\hat{\sigma}(N_\gamma)} = \frac{N_{\rm On} - \alpha N_{\rm Off}}{\sqrt{N_{\rm On} + \alpha^2 N_{\rm Off}}}. \tag{2.22}$$

This idea behind this formula is easy to understand. Nevertheless, Monte-Carlo simulation studies by Li and Ma [1983] shows that $\hat{\sigma}(N_\gamma) = \sqrt{N_{\rm On} + \alpha^2 N_{\rm Off}}$ is not a good estimator of $\sigma(N_\gamma)$ for $\alpha \neq 1$. To get a better $\hat{\sigma}(N_\gamma)$, one has to take the likelihood ratio test approach.

The method of likelihood ratio test has been widely used in high-energy astronomy to quantify the significance of a signal and to decide the preferred model for a dataset [Cash, 1979]. In the test, the maximum likelihoods of the *null-* and *alternative-* hypothesis are compared.

Consider a 2-D skymap containing n pixels and let $N = (N_1, ..., N_n)$ represents

the measured event counts in each pixel: N_i represents the measured event counts in the ith pixel. The likelihood of this dataset under a set of parameters $\Theta = (\Theta_1, ...\Theta_p)$ is given by:

$$L = \prod_{i=1}^{n} f(N_i; \Theta), \tag{2.23}$$

where $f(N_i; \Theta)$ is the probability distribution of N_i under a given Θ. In γ-ray astronomy, $f(N_i; \Theta)$ is usually assumed following the Poisson distribution:

$$P(N_i|\hat{N}_i) = \frac{\hat{N}_i^{N_i}}{N_i!} e^{\hat{N}_i}, \tag{2.24}$$

where $\hat{N}_i$, the expected count in the ith pixel is determined by the probability distributions of the signal and background. If the knowledge about these is lacking, the only thing one can do is to select an *On* and an *Off* region and calculate the likelihood by:

$$L(N|\Theta) = L(N_{\rm on}, N_{\rm Off}; \hat{N}_S, \hat{N}_B) = f(N_{\rm On}; \hat{N}_S, \hat{N}_B) f(N_{\rm Off}; \hat{N}_S, \hat{N}_B). \tag{2.25}$$

The signal and background counts $\hat{N}_S$ and $\hat{N}_B$ which yield the maximum likelihood under the given N_{On} and N_{Off} are calculated by:

$$\hat{N}_S = 0, \tag{2.26}$$
$$\hat{N}_B = \frac{\alpha}{1+\alpha}(N_{On} + N_{Off}), \tag{2.27}$$

for *null* hypothesis where there is no signal. Then the expected counts in *On*- and *Off*-regions are:

$$\hat{N}_{\rm On} = \frac{\alpha}{1+\alpha}(N_{\rm On} + N_{\rm Off}), \tag{2.28}$$
$$\hat{N}_{\rm Off} = \frac{1}{1+\alpha}(N_{\rm On} + N_{\rm Off}). \tag{2.29}$$

For *alternative* hypothesis where there is a signal,

$$\hat{N}_S = N_{\rm On} - \alpha N_{\rm Off}, \tag{2.30}$$
$$\hat{N}_B = \alpha N_{\rm Off}, \tag{2.31}$$

and

$$\hat{N}_{\rm On} = N_{\rm On}, \tag{2.32}$$
$$\hat{N}_{\rm Off} = N_{\rm Off}. \tag{2.33}$$

With Eq. (2.28)–(2.29) and Eq. (2.32)–(2.33), we can calculate the maximum likelihood of *null* and *alternative* hypothesis analytically by using Eq. (2.23) with

$$f(N_{\rm On};\hat{N}_S,\hat{N}_B) = f(N_{\rm On};\hat{N}_S,\hat{N}_B) = P\left(N_{\rm On}|\hat{N}_{\rm On}\right), \tag{2.34}$$

$$f(N_{\rm Off};\hat{N}_S,\hat{N}_B) = P\left(N_{\rm Off}|\hat{N}_{\rm Off}\right). \tag{2.35}$$

Let the maximum likelihood of two hypotheses be $L_0 = L(N;\Theta_0)$ and $L_1 = L(N;\Theta_a)$, and their ratio be $\lambda = L_0/L_1$. According to the Wilks' theorem [Wilks, 1938], $-2\ln\lambda$ follows a χ^2 distribution with r degrees of freedom, which is the difference between the numbers of free parameters in the two hypotheses. The value $-2\ln\lambda$ is defined as the *test statistic*:

$$TS \equiv -2\ln\lambda \sim \chi^2(r), \tag{2.36}$$

One can quantify the reliability of the favored hypothesis by the *p-value*, which is the probability that the obtained *test statistic* is merely due to statistical fluctuations:

$$p = \int_{TS}^{\infty} \chi^2(t,r)dt \tag{2.37}$$

For the case here, the *p-value* represents the probability that the obtained TS is not due to a real signal but merely the statistical fluctuation of the background. A TS-value can be translated to the significance by converting the *p-value* to the corresponding numbers of standard deviation away from zero in a Gaussian distribution via the *complementary error function* $erfc(x)$:

$$erfc(x) \equiv 1 - erf(x), \tag{2.38}$$

where $erf(x)$ is the error fuction defined as:

$$erf(x) = \frac{2}{\sqrt{\pi}}\int_0^x e^{-t^2}dt. \tag{2.39}$$

The significance, S standard deviations, for a given *p-value* p is:

$$S = \sqrt{2}\,erfc^{-1}(p). \tag{2.40}$$

In this case, we have two free parameters in the *alternative* hypothesis: $\hat{N}_S$ and $\hat{N}_B$, and one in the *null* hypothesis: $\hat{N}_B$. The degree of freedom is 1 and the significance S_γ can be calculated directly with the λ derived above, which is the

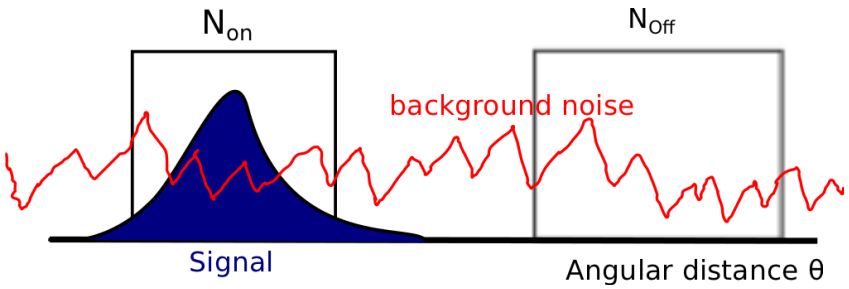

Figure 2.17: *On* and *Off* region for extracting signal and background.

so-called Li & Ma formula [Li and Ma, 1983]:

$$S_\gamma = \sqrt{2}\left(N_{\mathrm{On}} \ln\left(\frac{(1+\alpha)N_{\mathrm{On}}}{\alpha(N_{\mathrm{On}}+N_{\mathrm{Off}})}\right) + N_{\mathrm{Off}} \ln\left(\frac{(1+\alpha)N_{\mathrm{Off}}}{N_{\mathrm{On}}+N_{\mathrm{Off}}}\right)\right)^{1/2}. \quad (2.41)$$

Given the fact that most of the signals follow a Gaussian-like distribution, a too narrow width of the *On* region yields a lose of signal events and a too wide width includes more background events as seen in Figure 2.17. It is also clearly seen that this width strongly depends on the S/N ratio. For larger S/N ratio, the larger width of the *On* region collects more signal events while including less background noise. If the distribution of the signal changes with the observation conditions, it will be even harder to find the optimized width.

One can improve the likelihood function in 2.25 by $\hat{N}_i(x, y)$ inferred from the knowledge of the signal and background distribution:

$$\hat{N}_i(x, y) = PSF(x, y) \bigotimes (\mathrm{Exp(x, y)} \times \mathrm{Src(x, y)}) + \mathrm{Bg(x, y)}, \quad (2.42)$$

where $PSF(x, y)$ is the point spread function characterizing the instrument response to a point source, Exp(x, y) is the fuction to describe the exposure gradient in the 2-D map, Src(x, y) is the model of the source, and Bg(x, y) is the distribution of the background.

In practice, $PSF(x, y)$ can be calculated by the Monte-Carlo simulation events. Exp(x, y) and Bg(x, y) can be directly derived from the observation. Src(x, y) can be any function. Point-like, symmetric or asymmetric Gaussian, and shells-like models are commonly used for H.E.S.S. data analysis. In this work, all the position and extension fits are performed with the *hdsourcefit* package with the maximum likelihood method.

Chapter 3

Performance Studies

All the configurations yield different energy threshold, sensitivity, energy and angular resolution. Comparison about these quantities for different configuration will be addressed in this Chapter.

3.1 Analysis configurations

The analysis software *hap* contains three kinds of event reconstruction and selection algorithms: *hap* standard analysis, *hap* TMVA analysis, and *hap* TMVA+DM (Disp Method) analysis. The first one uses the *Geometrical reconstruction* and performs *post-selection* on the shape parameters (*MRSW* and *MRSL*). The second one also uses the *Geometrical reconstruction* but performs *post-selection* on the TMVA output $\epsilon_r(\zeta)$. The third one, developed in this thesis by expanding the studies by Berge [2010], uses *Disp Method* and *post-selection* on the TMVA output $\epsilon_r(\zeta)$ since this event selection method is proved more powerful on γ-hadron separation. This conclusion can be seen in Figure 3.1 where the background efficiency versus the γ efficiency with the shape-parameter cut and $\epsilon_r(\zeta)$ cut is compared. Except for very loose cuts (for which γ efficiency $\eta_\gamma \sim 1$), the background-rejection efficiency $(1 - \eta_{bg})$ under a given η_γ with the shape-parameter cut is always smaller than that with the $\epsilon_r(\zeta)$ cut.

The analysis configurations set up in *hap* are listed in Table 3.1. They are optimized for different source types and used according to the expected characteristics of the interested targets:

- *std* configuration: This configuration is optimized for sources with moderate spectral indices and flux. It takes a compromise between the energy threshold and signal to noise ratio and is suitable for spectral analysis.
- *hard* configuration: This configuration is optimized for sources with hard spectra but with smaller flux. Its higher *size* cut results in better angular

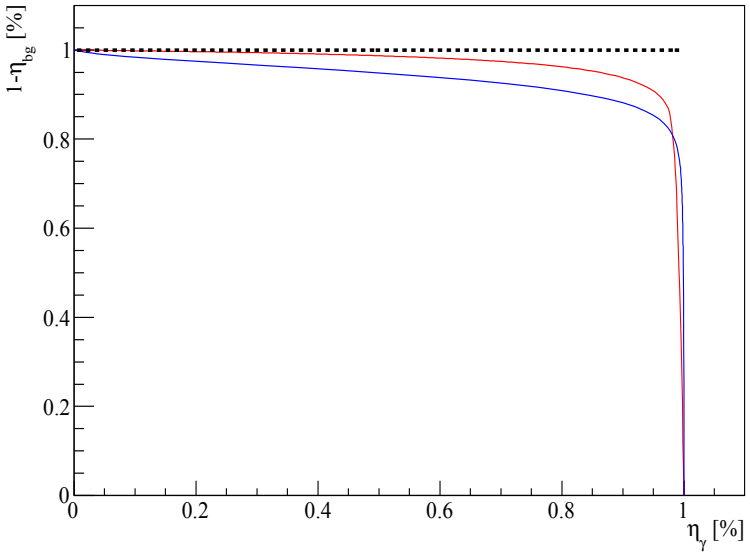

Figure 3.1: The blue line denotes the γ-efficiency (η_γ) versus background-rejection efficiency ($1 - \eta_{bg}$) for the shape-parameter cuts and the red line for the TMVA cuts. The dashed line denotes the perfect γ-hadron separation: all background events are rejected while all γ events are kept.

Configuration	Spectral index	Source flux[%Crab]
std	-2.6	10
hard	-2.0	1
weak	-2.6	0.5
loose	-3.2	100

Table 3.1: Configurations set up in *hap*. Each configuration is optimized for a pre-defined source type with an assumed spectral index and source flux in the unit of the Crab flux.

Configuration	$MRSW[\sigma]$	$MRSL[\sigma]$	Max. θ^2[deg^2]	Min. *Size*[p.e.]
std	-2.0∼0.9	-2.0∼2.0	0.0125	80
hard	-2.0∼0.7	-2.0∼2.0	0.01	200
loose	-2.0∼1.2	-2.0∼2.0	0.04	40

Table 3.2: The selection cuts used in HAP Standard analysis configurations.

resolution but also the loss of significant amount of low energy events. This configuration is suitable for morphology studies of complicated targets.

- *weak* configuration: This configuration is designed for very weak sources with moderate spectral indices (e.g. the star-burst galaxy NGC253 [Acero et al., 2009; Ohm, 2010]).

- *loose* configuration: This configuration is designed for strong sources with very soft spectral indices. Because of the relatively low energy threshold, it is suitable for spectral analysis. Nevertheless, this configuration suffers from the poor angular resolution and is more suitable for the analysis of extra-galactic point sources such as Active Galactic Nuclei (AGN).

Configuration	Max. $\epsilon_\gamma(\zeta)$	Max. θ^2[deg^2]	Min. *Size*[p.e.]
std_ζ	0.84	0.0125	60
$hard_\zeta$	0.89	0.01	160
$weak_\zeta$	0.80	0.01	80
$loose_\zeta$	0.85	0.02	40

Table 3.3: The selection cuts used in HAP TMVA analysis configurations.

Configuration	Max. $\epsilon_\gamma(\zeta)$	Max. θ^2[deg^2]	Min. *Size*[p.e.]	Max Error[deg]
$std_{\zeta,dm}$	0.8	0.0125	60	X
$hard_{\zeta,dm}$	0.86	0.01	160	X
$hires_{\zeta,dm}$	0.86	0.004	160	0.08

Table 3.4: The selection cuts used in HAP TMVA+DM analysis configurations.

3.2 Comparison of TMVA and TMVA+DM configurations

3.2.1 The PSF and angular resolution

Due to the limited resolution of the instrument, the angular distribution of the reconstructed events of a γ-ray point source is not a δ-function and has a spread. This distribution is described by the point-spread-function (PSF) and characterized by the 68% containment radius, R_{68}, which is referred to as the angular resolution of the instrument. The H.E.S.S. PSF is calculated by lookups generated by Monte-Carlo simulated γ-ray point sources under different observation conditions. Since the PSF is roughly radially-symmetric, the PSF lookups are filled in the 1-D squared angular distance (θ^2) space and fit with a triple-Gaussian function to eliminate statistical fluctuations:

$$PSF(\theta^2) = \mathrm{A}\left(\exp(-\frac{\theta^2}{2\sigma_1^2}) + \mathrm{A}_2\exp(-\frac{\theta^2}{2\sigma_1^2}) + \mathrm{A}_3\exp(-\frac{\theta^2}{2\sigma_1^2})\right). \tag{3.1}$$

The shape of PSF is dependent on the observation conditions, e.g. zenith angle, source offset, azimuth angle , telescope pattern, and muon efficiency.

PSF dependency on the multiplicity

The multiplicity is the number of telescopes passing the $pre-selection$ cut whose images are used in the event reconstruction. As shown in Figure 3.2, the resolution significantly improves with higher multiplicities for all zenith angles. This phenomenon results from the advantage of stereo reconstruction. When more images are available, more intersection points of the image major axes are provided. The influence of statistical fluctuations thus reduces and yields a more accurate estimation of event direction. At the mean time, the improvement on resolution by the *Disp method* gets larger for smaller multiplicities.

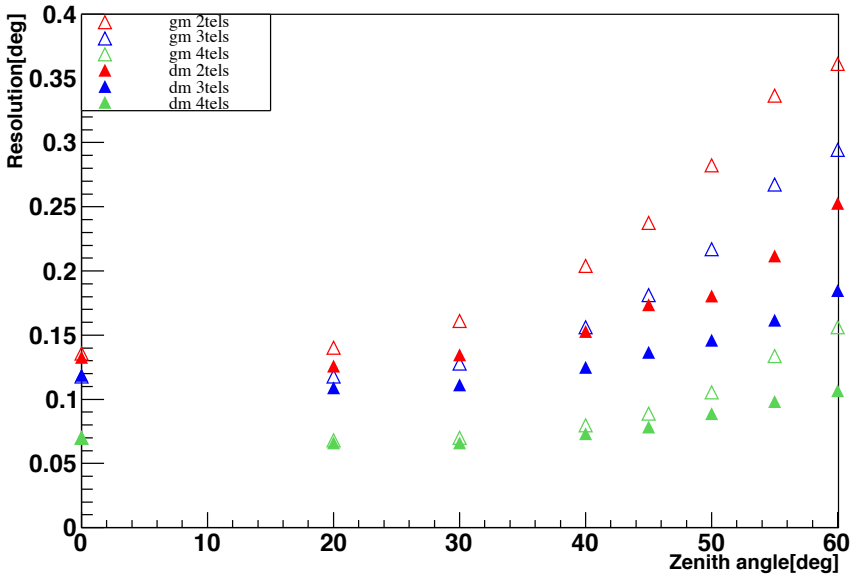

Figure 3.2: Angular resolution R_{68} of the std_{ζ} (hollow triangles) and $std_{\zeta,\mathrm{dm}}$ (solid triangles) configurations versus the zenith angle for different multiplicities at the 0.5° offset.

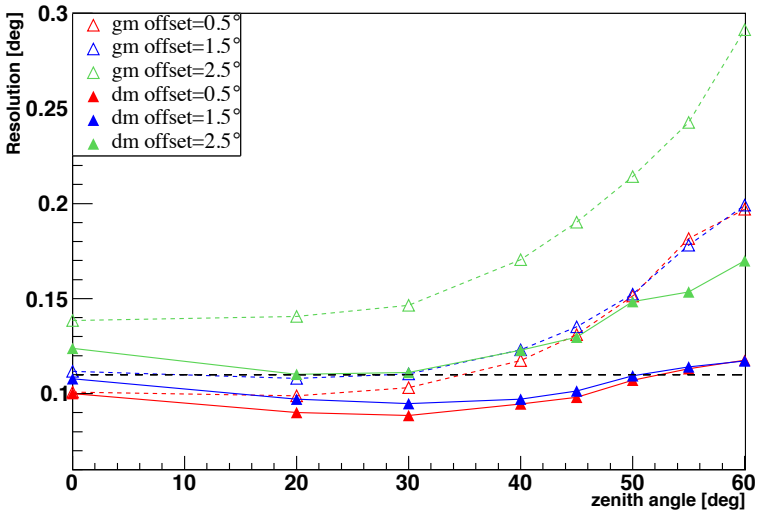

(a) *std* configuration

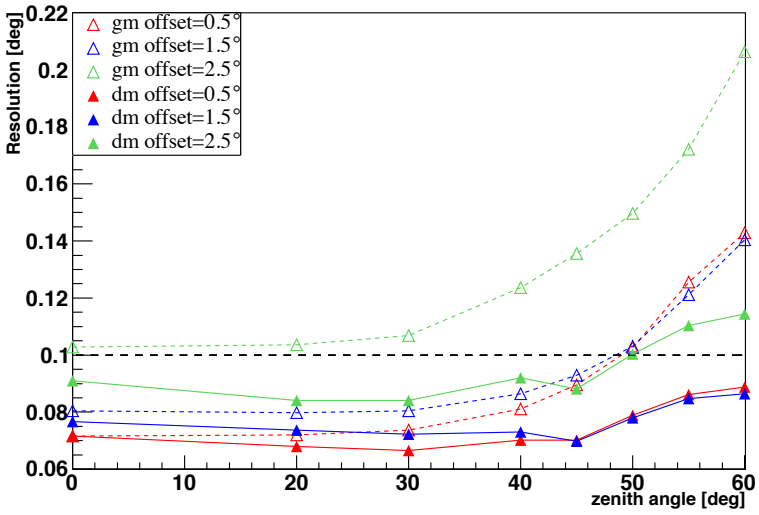

(b) *hard* configuration

Figure 3.3: (a) Angular resolution R_{68} versus zenith angle for std_ζ (dashed lines and hollow triangles) and $std_{\zeta,\mathrm{dm}}$ (solid lines and solid triangles) at different offsets. (b) Angular resolution versus zenith angle for $hard_\zeta$ (dashed lines and hollow triangles) and $hard_{\zeta,\mathrm{dm}}$ (solid lines and solid triangles) at different offsets. The horizontal dashes lines denote the θ-cut values.

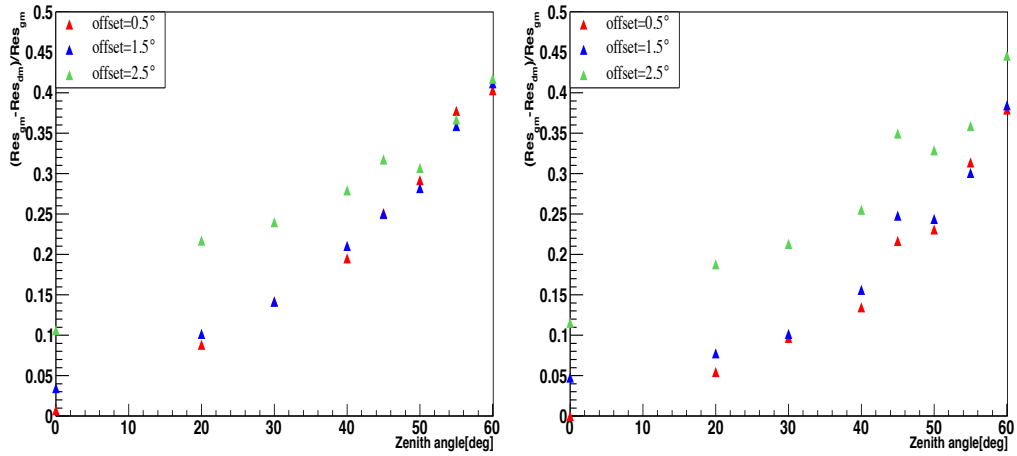

(a) *std* configuration (b) *hard* configuration

Figure 3.4: (a) Angular resolution improvement versus zenith angle for *std* configuration at different offsets. (b) Angular resolution improvement versus zenith angle for *hard* configuration at different offsets.

PSF dependency on the zenith angle

The PSF has a strong dependency on the zenith angle as shown in Figure 3.3. In general, the PSF gets wider with the increasing zenith angle. Both the PSF of *Geometrical reconstruction* and *Disp method* have this tendency. Nevertheless, the change of PSF width of the *Disp method* is more moderate. For a larger zenith angle, as discussed in Section 1.2, the radius of Čerenkov light pool increases. The effective area of the instrument increases since more distant showers can be detected. This can be clearly seen in Figure 3.5. In these plots, the *core* distributions of Monte-Carlo simulated $\gamma-$ray events passing the *pre-selection* are shown. One can see that for larger zenith angles, the *core* positions of detected events are more widely scattered and more and more events have a *core* position outside the telescope array. Figure 3.6(a) shows the multiplicity distribution for different zenith angles. One can see that for increasing zenith angles, the fraction of events with multiplicity of 4 increases because the chance that four telescopes are illuminated simultaneously is larger for a larger Čerenkov light pool.

It was mentioned in the previous paragraph that the angular resolution is improved with increasing multiplicities. Nevertheless, this only holds true when the telescopes are viewing the shower at different viewing angles and is not the case here as can be seen in Figure. 3.6(b). This plot shows how the distribution of $\Delta\varphi$, the angle between image axes of two telescopes, varies with the zenith

angle. A smaller $\Delta\varphi$ means a smaller difference in the view angles. For events observed by telescopes at similar viewing angles, the resultant images are nearly parallel. Less information is gained by multi-images and small fluctuations in the image may shift the image major axis away from the real position and results in bad reconstruction on the event direction by the *Geometrical reconstruction* as shown in Figure 3.7. The capability of stereo reconstruction thus reduces and the reconstruction quality degrades. The reconstruction quality can be improved by the *Disp method* with the use of estimated *disp*, so the improvement on the angular resolution by the *Disp method* also increases with the zenith angle as shown in Figure 3.4.

PSF dependency on the offset

From Figure 3.3, one can also see the dependency of PSF on the offset. This dependency is marginal for offsets up to 1.5° and gets significant above this value. This effect is also due to the increasing amounts of events observed by the telescopes at similar viewing angles. Figure 3.8 shows the *core* position distributions of simulated γ-ray events at different offsets. The distribution is symmetry for 0° offset. For larger offsets, a selection effect emerges due to the limited field of view of the camera. In the plot of 2.5° offset, the events triggering the system all have the *core* position outside the telescope array and results in more parallel images. Figure 3.9 shows the $\Delta\phi$ distribution for events at different offsets. The $\Delta\phi$ tends to get smaller for increasing offsets as expected.

PSF dependency on the azimuth angle

Since Čerenkov light is emitted by charged particles whose paths are bent by the geomagnetic field, the Čerenkov light distributions change with the azimuth angles of event directions. The impact of the geomagnetic field on the H.E.S.S. experiment was discussed in Bernloehr [2005]. The strength of magnetic field (B field) at the H.E.S.S. site is $\sim 28.7\mu T$. the smallest in all atmospheric Čerenkov experiment sites. Thus the impact of geomagnetic field is not very significant: The resolution of showers from the South is about 10% worse than from the North. Figure 3.11 shows the angle between the shower direction and B field as a function of azimuth angle for different zenith angles. One can see that for zenith angles smaller than 70°, the angle is larger for showers from the South (180° azimuth angle) and results in larger bending on the paths of charged particles. The spreads of lateral Čerenkov light distributions of the showers are therefore wider. This means an increasing in *width* and decreasing in *image size* for a shower of a given energy and *impact distance*. The resulted uncertainty on the orientation of Hillas ellipse is thus larger. Besides, the geomagnetic field also

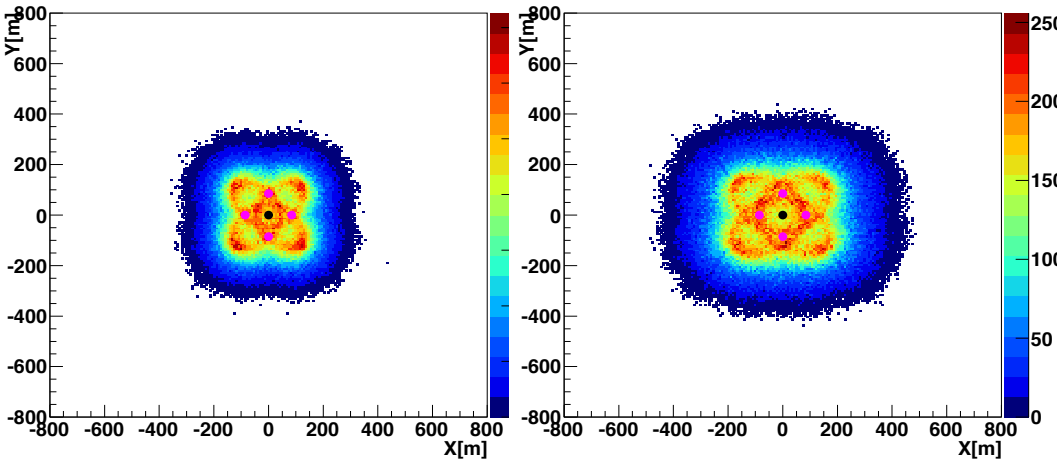

(a) 0° zenith angle

(b) 30° zenith angle

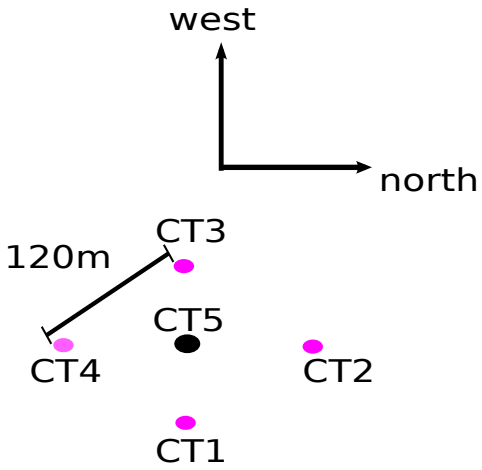

(c) Layout of the telescope array

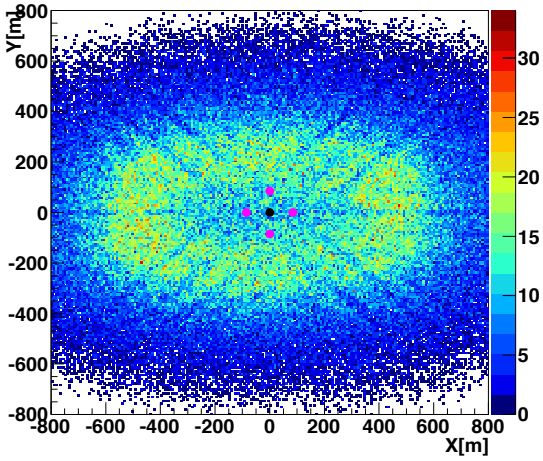

(d) 60° zenith angle

Figure 3.5: The distributions of true *core* positions of events simulated at 0.0° offset and different zenith angles. The magenta dots denote the positions of the Phase-I telescopes. The black dot denotes the array center where CT5 is situated.

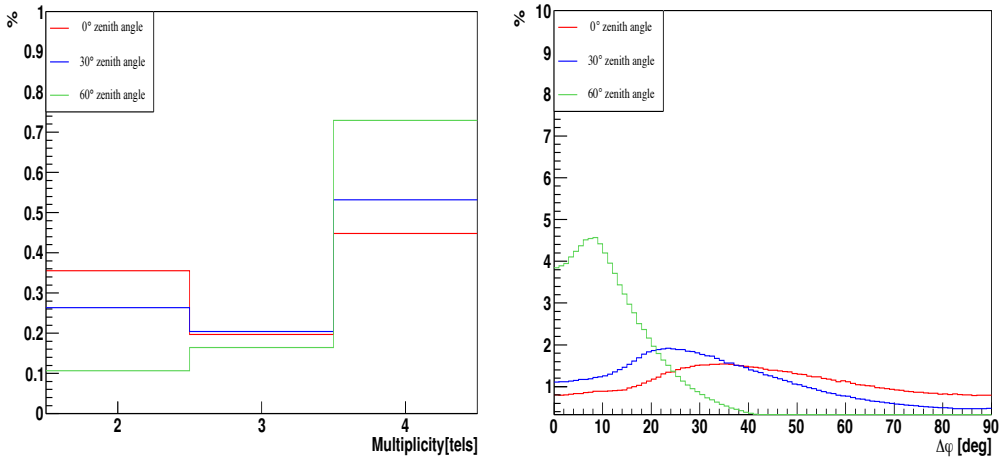

(a) (b)

Figure 3.6: a) Multiplicity (b) $\Delta\varphi$ distribution for events simulated at 0°, 30°, and 60° zenith angles and 0° offset. $\Delta\varphi$ is the angle between image axes of two telescopes.

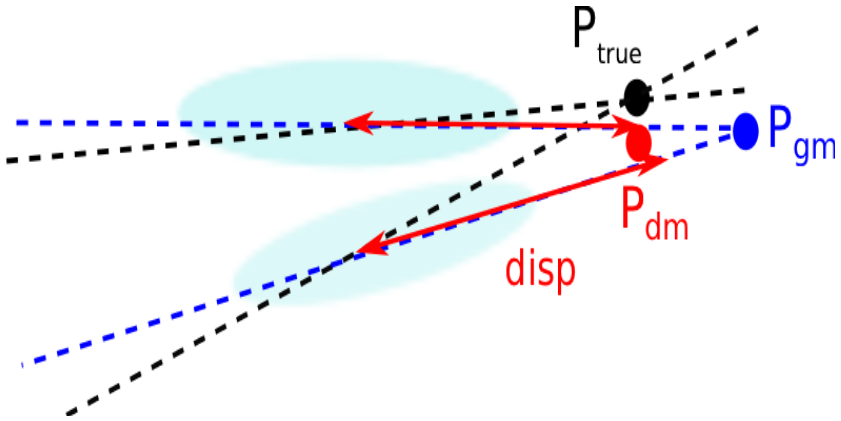

Figure 3.7: This plot illustrates how the direction reconstruction of nearly-parallel images is improved by the *Disp method* with the estimate of *disp*. P_{true}, P_{gm}, and P_{dm} are the true position, reconstructed position by the *Geometrical reconstruction* and *Disp method*.

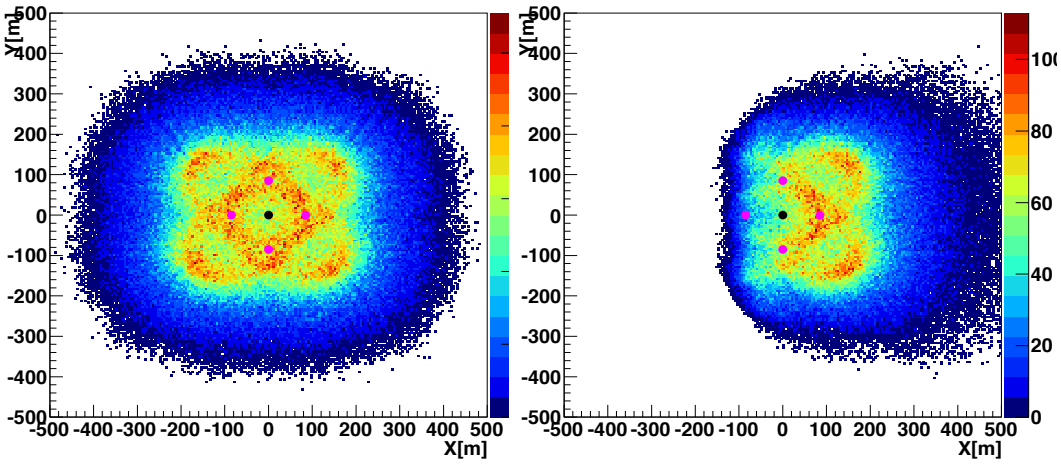

(a) 0.0° offset

(b) 1.5° offset

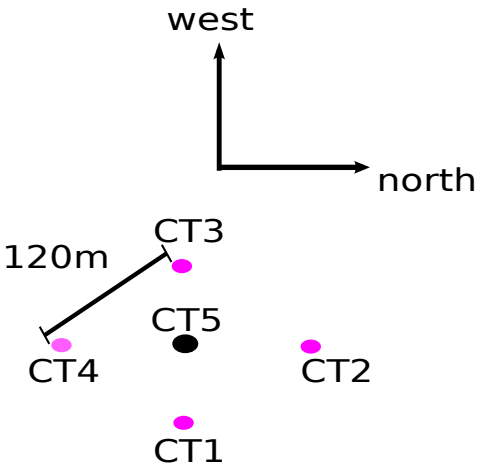

(c) Layout of the telescope array

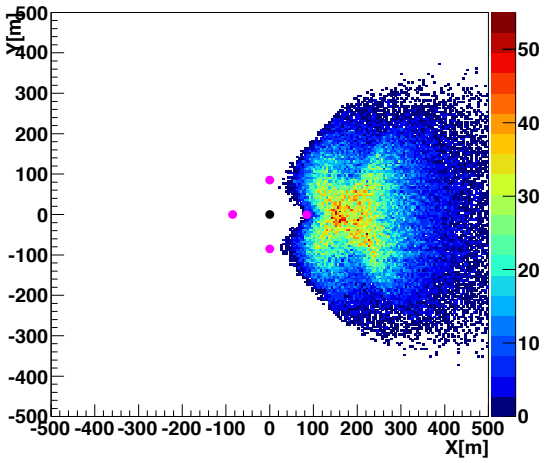

(d) 2.5° offset

Figure 3.8: Distributions of true *core* positions of events simulated at 30° zenith angle and different offsets. The magenta dots denote the positions of the Phase-I telescopes. The black dot denotes the array center where CT5 is situated.

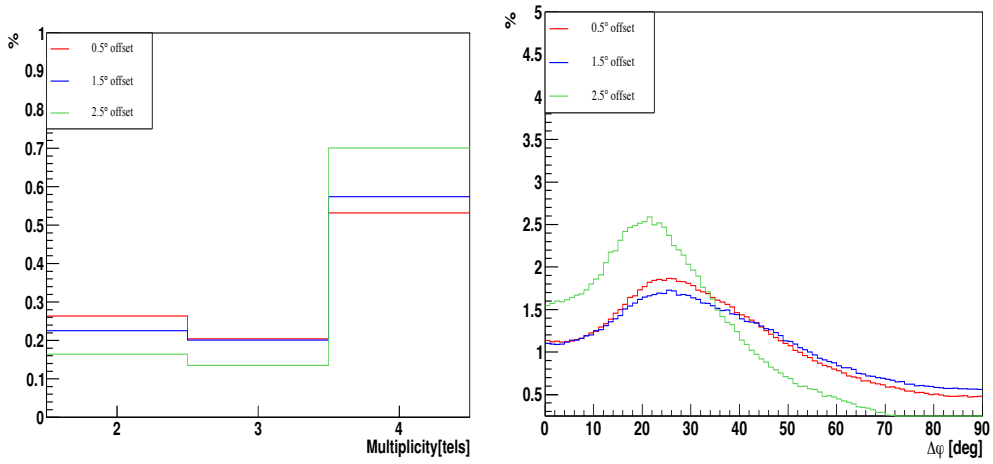

(a) (b)

Figure 3.9: (a) Multiplicity (b) $\Delta\varphi$ distribution for events simulated at 0.5°, 1.5°, and 2.5° offsets. $\Delta\varphi$ is the angle between images axes of two telescopes.

results in a distortion on the shower image and rotates the major axis away from the shower direction. This also leads to poorer direction reconstruction of showers from the South. Figure 3.10 shows the difference on the 68% containment radius for the showers from the North and South at different zenith angle. The largest difference occur at $40° - 50°$ zenith angle, consistent with Figure 3.11.

PSF dependency on the muon efficiency

A lower muon efficiency means a smaller *image size* for the same Čerenkov intensity. Decreasing muon efficiency results in a selection effect that higher energy and more nearby events are more likely to be detected. This means a smaller effective detection area for low energy events and an increasing on energy threshold. Since the PSF of higher energy events is narrower, the PSF of muon phase with lower muon efficiency is narrower. This effect is not large: only 10% difference between muon phase 100 and 101.

PSF dependency on the source spectrum

As shown in Figure 3.12, the angular resolution changes with the energy. PSF lookups are filled in energy bins with the assumed spectral index of -2. A weighting procedure [Gast, 2011] is taken to calculate the averaged PSF for a given spectral index of a real source. Since the PSF for low energy events are

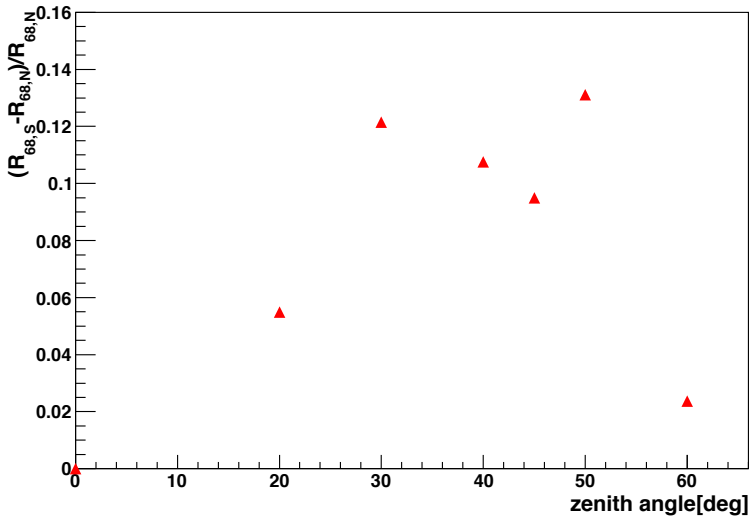

Figure 3.10: Relative difference of angular resolution for showers from the North and South.

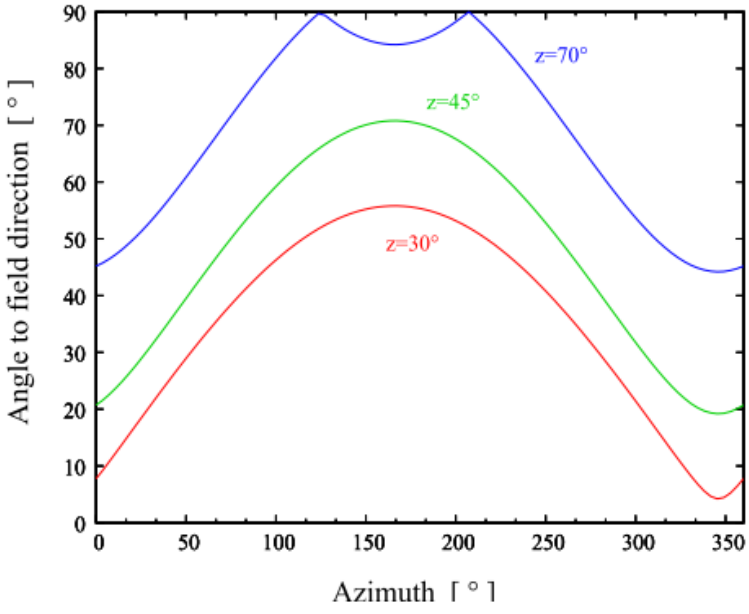

Figure 3.11: Angles between B field and shower direction versus shower azimuth angle for different zenith angles. Taken from Bernloehr [2005].

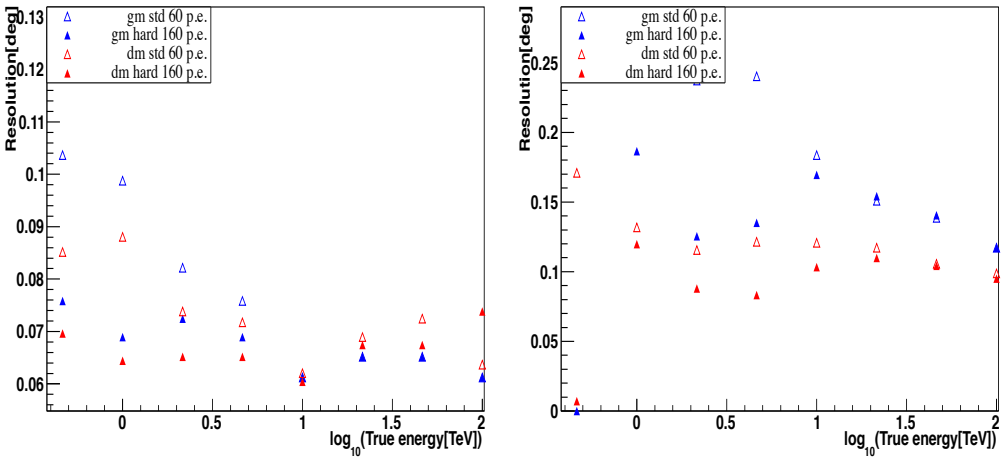

(a) 30° zenith angle (b) 60° zenith angle

Figure 3.12: Angular resolution R_{68} versus energy at 30° and 60° zenith angles for std_{ζ}, $std_{\zeta,\mathrm{dm}}$, $hard_{\zeta}$ and $hard_{\zeta,\mathrm{dm}}$ configurations.

wider, the averaged PSF of a source with a soft spectrum is wider than of a source with hard spectrum. Figure 3.13 shows the difference on the containment radius resulted from the assumed spectral indices for different configurations. For a typical detection of a source, the statistical uncertainty of the power index usually amounts up to ± 0.3 within 1σ. The uncertainty on the power index of 0.6 will lead to a less than 5% uncertainty on the PSF.

3.2.2 Comparison of γ efficiency and Q factor

Since all the variables used for γ-hadron separation are dependent on the reconstructed parameters (e.g.: direction, *impact distance* and energy), the optimized $\epsilon_r(\zeta)$ and the performance on γ-hadron separation change for TMVA+DM configurations. The comparison of γ efficiency and quality factor (Q factor) between the new and old reconstruction methods is addressed here.

The γ efficiency η_γ and background efficiency η_{bg} are defined as:

$$\text{with} \qquad \eta_\gamma = \frac{\hat{\mathrm{N}}_\gamma}{\mathrm{N}_\gamma}, \eta_{\mathrm{bg}} = \frac{\hat{\mathrm{N}}_{\mathrm{bg}}}{\mathrm{N}_{\mathrm{bg}}} \tag{3.2}$$

where $\hat{N}_\gamma$ and $\hat{N}_{\mathrm{bg}}$ are the number of γ-ray and background events passing a certain cut ; N_γ and N_{bg} are the number of events before the cut. The quality

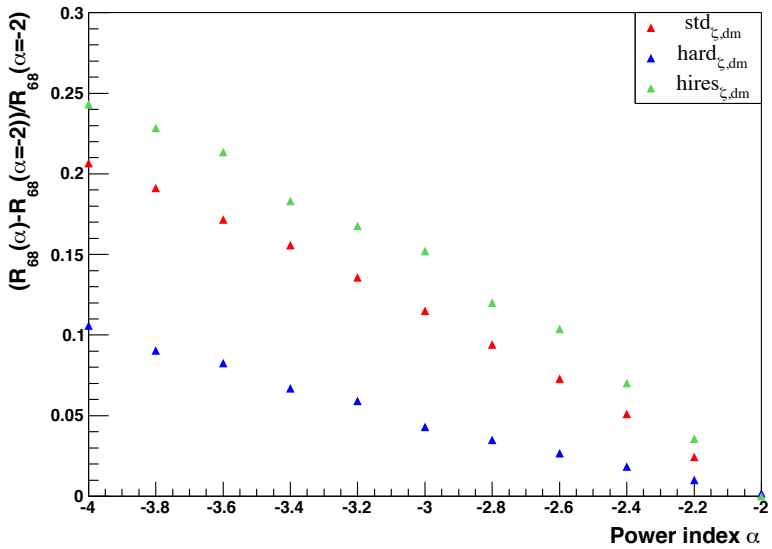

Figure 3.13: Angular resolution R_{68} versus the assumed power-law spectral indices at a mean zenith angle of 47°.

factor Q is defined as:

$$Q = \frac{\eta_\gamma}{\eta_{\rm bg}}, \tag{3.3}$$

Figure 3.14 shows the relative γ efficiency, $\eta_{\gamma,\rm dm}/\eta_{\gamma,\rm gm}$ after *post-selection*, versus the zenith angle. The changes on the relative γ efficiency and Q are related to two factors: 1.The different $\epsilon_\gamma(\zeta)$ cuts. 2. The different event reconstruction quality. As listed in Tables 3.3 and 3.4, the cuts on $\epsilon_\gamma(\zeta)$ are slightly stricter for TMVA+DM configurations. Nevertheless, the relative γ efficiency remains around 1 due to the compensation of better event reconstruction which keeps more events in the *On-region*. Because of the rapid change of the PSF with the zenith angle, the optimized θ^2 cut at 0.5° offset and 20° zenith angle for TMVA configurations is obviously too small for larger zenith angles (see Figure 3.3). The changing on the PSF for TMVA+DM configurations is more moderate. This results in a significant increasing of relative γ efficiency above 45° zenith angle for *std* configuration and 55° for *hard* configuration, where the resolution for TMVA configurations exceeds the *theta*^{2} cut. The relative γ efficiency drops with the increasing offset. This implies the distribution of variables used in the MVA classification of TMVA+DM configurations are more sensitive to the offset than that of TMVA configurations. Training in offset bands may improve the performance of TMVA+DM configuration at larger offsets.

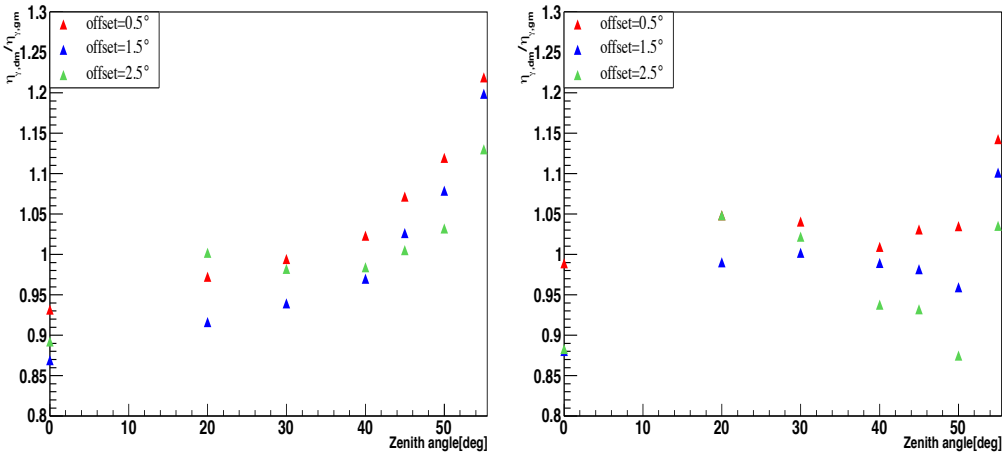

(a) *std* configuration (b) *hard* configuration

Figure 3.14: Relative γ efficiency ($\eta_{\gamma,\mathrm{dm}}/\eta_{\gamma,\mathrm{gm}}$) of *std* and *hard* configurations.

The relative Q factor, $Q_{\mathrm{dm}}/Q_{\mathrm{gm}}$ is shown in Figure 3.15. Given the relatively higher γ efficiency and background rejection efficiency resulted from the stricter cuts on ζ, Q_{dm} is larger than Q_{gm}.

3.2.3 Energy bias and resolution

The bias on the reconstructed energy is assessed by the relative error on the reconstructed energy $\Delta E/E \equiv (E_{\mathrm{reco}} - E_{\mathrm{true}})/E_{\mathrm{true}}$. Figure 3.16 shows the $\langle \Delta E/E \rangle$ profile of Monte-Carlo simulated γ ray events at 30° zenith angle and 0.5° offset passing *post-selection*. The distribution has a positive bias at low energies which is a selection effect: Only events with *image size* fluctuating upward can trigger the telescope system and pass the *image size* cut. The distribution of $std_{\zeta,\mathrm{dm}}$ configuration has a slightly larger bias due to the bias in the *impact distance* lookup table: For very small *impact distances* ($< 25\,\mathrm{m}$), the mean value in the lookup table is upward biased because there are no negative *impact distances* in the distributions. Thus the resulted *impact distance* in this regime are slightly overestimated. At the very large energies, there is a negative bias in the reconstructed energy due to the downward bias in the energy lookup table resulted from a similar reason: There are no energy values larger than the upper bound energy used in the simulation. Besides, image truncations by the read-out window and camera edges also results in underestimation on the energy because of the reduced *image size*. At the moderate energies, the bias is close to zero for all configurations. For doing spectral analysis, energy ranges with large bias should

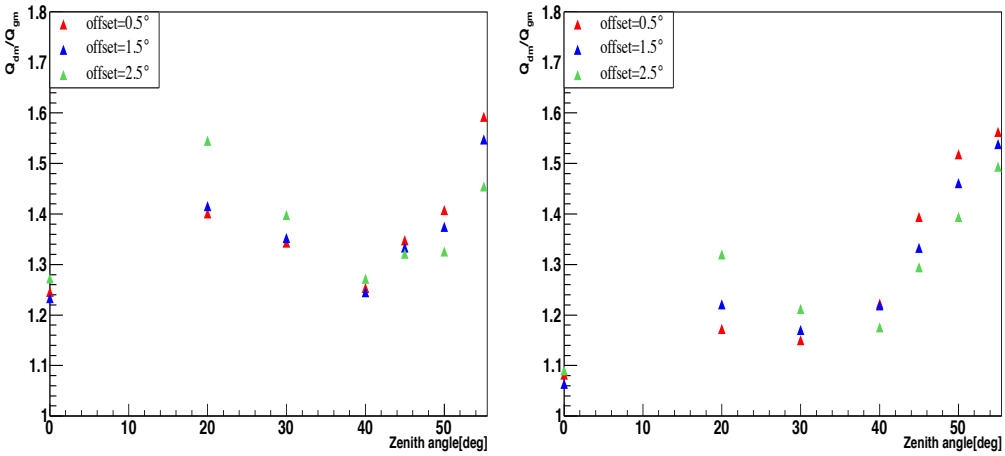

(a) *std* configuration (b) *hard* configuration

Figure 3.15: Relative Q-factor (Q_{dm}/Q_{gm}) of *std* and *hard* configurations.

be excluded. This range is defined by the *safe energy threshold*, which is defined as the upper edge of the first bin in the energy bias profile for which the bias falls below 10%. The *safe energy threshold* of each configuration is denoted by a vertical line in Figure 3.16. The *hard* configurations have much higher *safe energy thresholds* than *std* configurations due to the stricter *image size* cuts. In Figure 3.17(a), the *safe energy threshold* versus the zenith angle is plotted. The energy threshold increases with the zenith angle because the lateral Čerenkov light density of the same shower energy which translates into the *image size* gets lower as the light pool enlarges (as shown in Figure 1.5. Figure 3.17(b) shows the energy resolution defined as the RMS of $\Delta E/E$ distribution as a function of energy. The best energy resolution reaches about 12% in the TeV regime and is slightly improved due to better *impact distance* reconstruction by the *Disp method*. It gets poorer below the *safe energy threshold* and above 40 TeV where the bias appears.

3.2.4 Effective detection area

After event reconstruction and background subtraction, the differential flux of a $\gamma-$ray source can be calculated. It is defined as the number of γ-ray excess per unit area, energy and time:

$$F(E) = \frac{1}{A_{\text{eff}}(E, \phi_z, \psi, \nu_{\text{az}})} \frac{d^2 N_\gamma}{dE dt}, \tag{3.4}$$

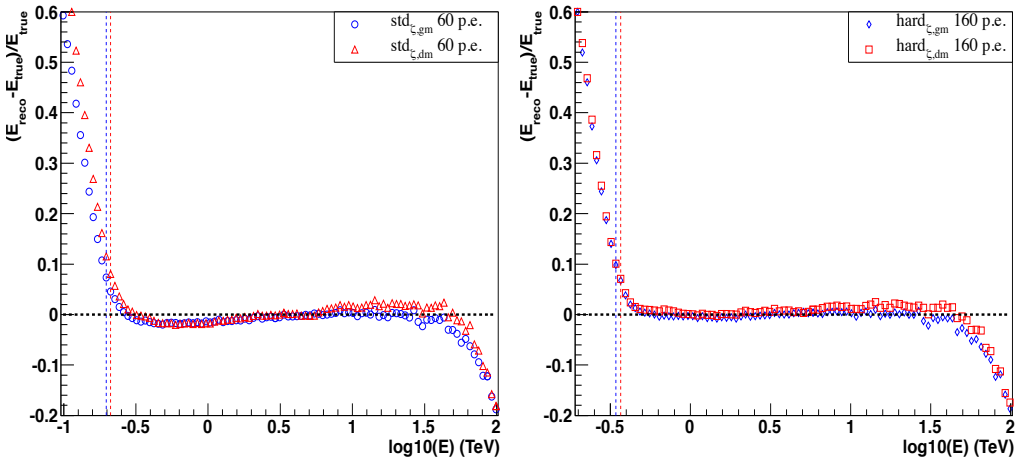

(a) *std* configurations (b) *hard* configurations

Figure 3.16: Bias in percentage of reconstructed energy versus the true energy. The dashed vertical lines denotes the *safe energy threshold* above which the bias of reconstructed energy is smaller than 10%.

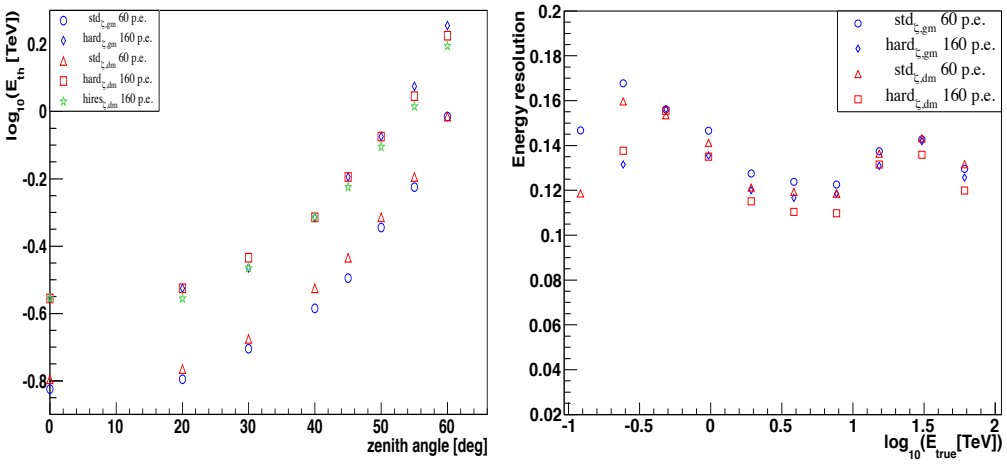

(a) *Safe energy threshold* (b) Energy resolution

Figure 3.17: (a) The *safe energy threshold* as a function of the zenith angle. (b) The energy resolution as a function of the true energy.

In this equation, $d^2N_\gamma/dEdt$ is the number of excess events per unit energy bin and time. E, ϕ_z, ψ, and $\nu_{\rm az}$ are the energy, zenith angle, offset and azimuth angle of the events. The detection effective area $A_{\rm eff}$ is the total collection area for 100% efficient γ-ray detection multiplied by the selection efficiency $A_{\rm eff}(E, \phi_z, \psi, \nu_{\rm az}) \equiv \epsilon(E, \phi_z, \psi, \nu_{az}) A(E, \phi_z, \psi, \nu_{az})$. The selection efficiency and total collection area have to be derived from Monte-Carlo simulation and are combined together as $A_{\rm MC}$. Then the effective detection area is calculated by:

$$A_{\rm eff}(E, \phi_z, \psi, \nu_{\rm az}) = \frac{N_\gamma^{\rm sel}(E, \phi_z, \psi, \nu_{\rm az})}{N_\gamma^{\rm MC}(E, \phi_z, \psi, \nu_{\rm az})} A_{\rm MC}(E, \phi_z, \psi, \nu_{\rm az}). \tag{3.5}$$

The effective detection area for *std* and *hard* configurations is shown in Figure 3.18 and the difference between TMVA and TMVA+DM configurations is plotted in Figure 3.19. The steep decline in the effective detection area at the lowest energies is due to the selection of the telescope system trigger and the *image size* cut. Above the *safe energy threshold*, the effective detection area changes slowly with the energy and the difference between different configurations is small. The effective detection area of the $std_{\zeta,{\rm dm}}$ configuration at the highest energy drops more quickly because the *Disp Method* is more sensitive to the image truncation effect by the read-out window and camera edge which leads to underestimation of *disp*. Because of better direction reconstruction, more γ-ray events are collected in the *On-region*. The increase in γ efficiency yields an increase in effective detection area. This effect is larger for moderate energy events above the *safe energy threshold* as shown in Figure 3.12 and translates into the small bump at $300\,GeV$ in Figure 3.19(a). For larger zenith angle, this effect is significantly larger as shown in Figure 3.19(b) where the effective detection area is 20% to 40% enlarged.

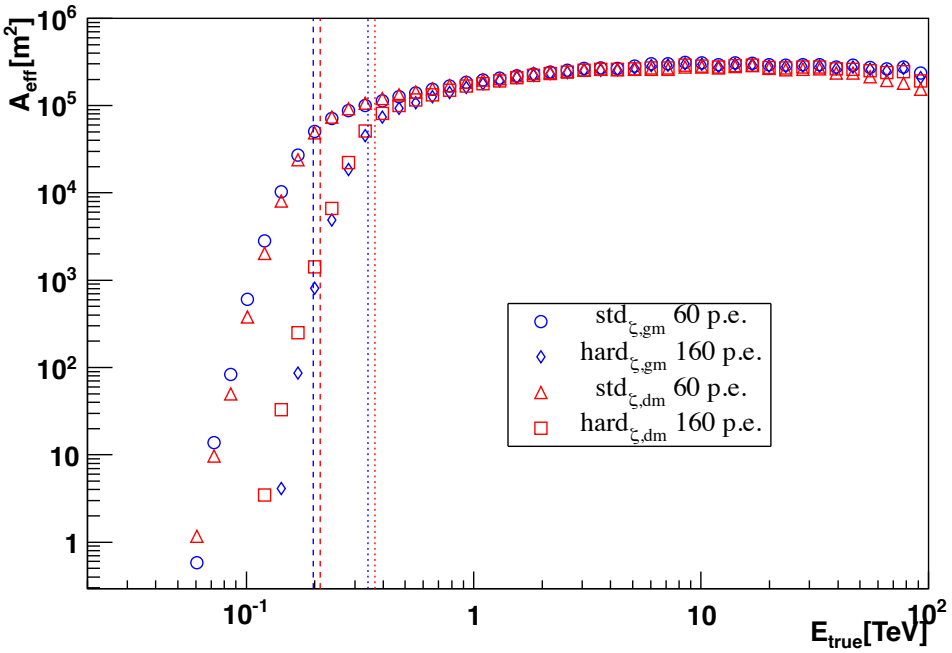

Figure 3.18: Effective detection area of TMVA and TMVA+DM configurations.

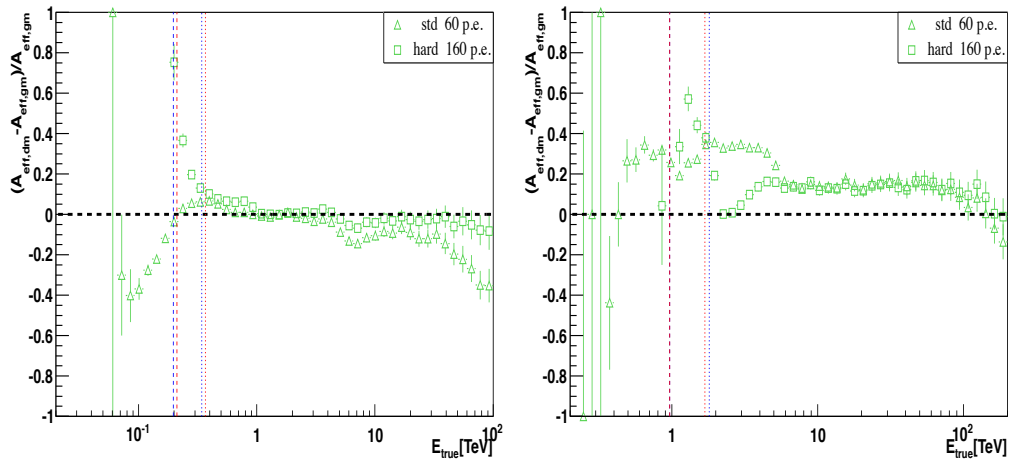

(a) 30° zenith angle

(b) 60° zenith angle

Figure 3.19: Difference in the effective detection area between TMVA and TMVA+DM configurations at 30° and 60° zenith angle at 0.5° offset.

3.3 Direction uncertainty and the $hires_{\zeta,\mathrm{dm}}$ configuration

Figure 3.20(a) shows the distribution of direction uncertainty, σ_P as defined in Eq. (2.14) for zenith angles from 0° to 60°. One can see that the distribution varies slightly with the zenith angle. For larger zenith angles, the uncertainties tend to be larger. Figure 3.20(b) shows the angular resolution with respect to the direction uncertainty. The resolution shows a good correlation with the uncertainty except at the 60° zenith angle. *Dist method* uses the *impact distance* from the *Geometrical reconstruction* as an input parameter of the lookup tables. Since *impact distance* is a reconstructed parameter, it has an uncertainty. This uncertainty is taken into account in error propagation. However, for some extreme cases, if the event direction and the core position are reconstructed in the wrong direction of the left-right ambiguity by *Geometrical reconstruction*, the estimation of *impact distance* will be severely biased. The value of *disp* taken by this *impact distance* will yield a resulted event direction falling far away from the real position and the calculation of the uncertainty can not be correct. This kind of cases happen more frequently at higher zenith angles.

The correlation between the direction uncertainty and resolution suggest that one can apply a cut on the direction uncertainty to improve the resolution to an desired value. Figure 3.21 shows the resolution one can obtain by applying this extra cut on the $hard_{\zeta,\mathrm{dm}}$ configuration at different zenith angles and offsets. In this work, a cut of $\sigma_P < 0.08\,\mathrm{deg}$ is made and named as $hires_{\zeta,\mathrm{dm}}$ configuration. This cut reduces the γ efficiency η_γ as shown in Figure 3.23(a) but still keep about 70% relative Q factor as shown in Figure 3.23(b) because it rejects even more background events at the mean time. The resulted resolution values of all zenith angles are shown in Figure 3.22. The variation with the zenith angle is very small. Figure 3.24 shows the $\langle \Delta E/E \rangle$ profile of Monte-Carlo simulated γ ray events at 30° zenith angle and 0.5° offset passing the $hires_{\zeta,rmdm}$ *post-selection* cut. The behavior of this profile is quite similar to the ones of *std* and *hard* configurations. The energy threshold as a function of zenith angle and the energy resolution as a function of energy are plotted in Figure 3.25(a). The plots of $hard_{\zeta,rmdm}$ configuration are also shown for comparison. The energy threshold is only slightly increased and the energy resolution is about 15% improved after the direction uncertainty cut. The effective detection area and the difference to the $hard_{\zeta,rmdm}$ configuration are shown in Figures 3.26(a) and 3.26(b). Although the *safe energy threshold* does not significantly increase, the drop in effective detection area is large below 1 TeV.

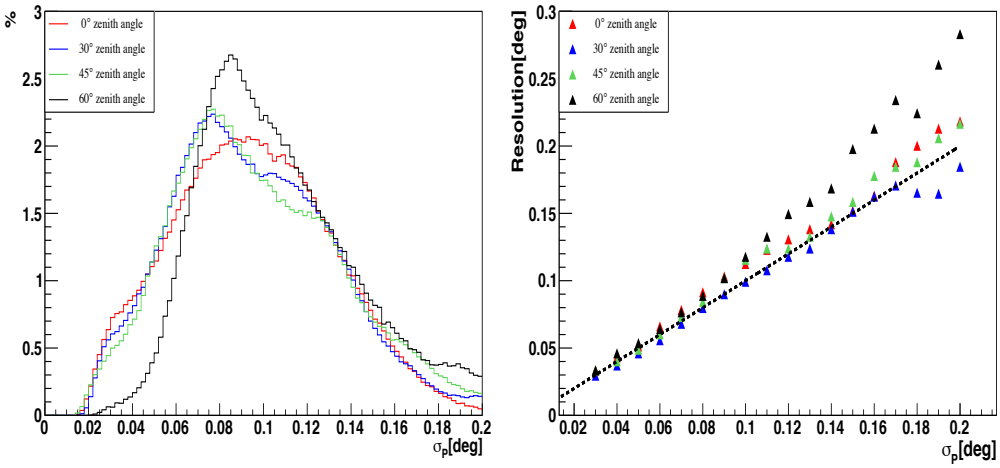

(a) (b)

Figure 3.20: (a) Direction uncertainty distribution (b) Angular resolution R_{68} versus direction uncertainty at 0° to 60° zenith angles at the 0.5° offset.

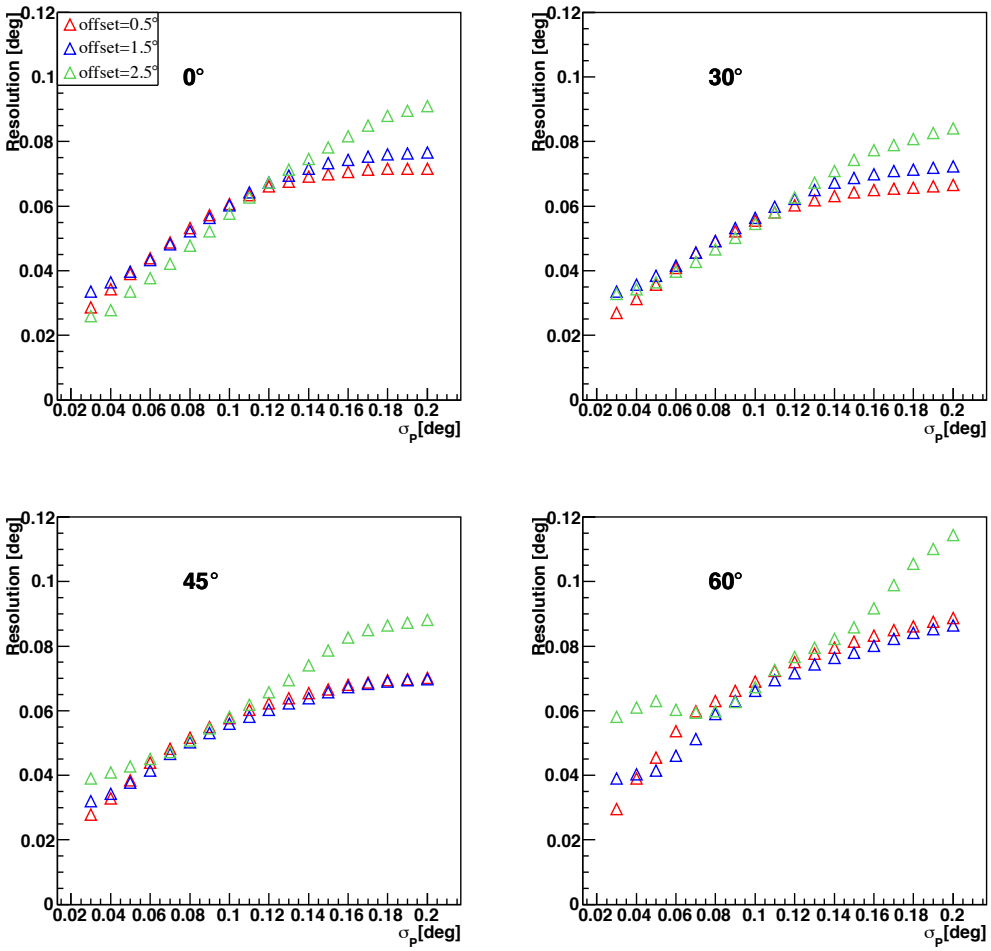

Figure 3.21: Angular resolution R_{68} versus direction uncertainty cuts on the $hard_{\zeta,\mathrm{dm}}$ configuration at 0° to 60° zenith angles and 0° to 2.5° offsets.

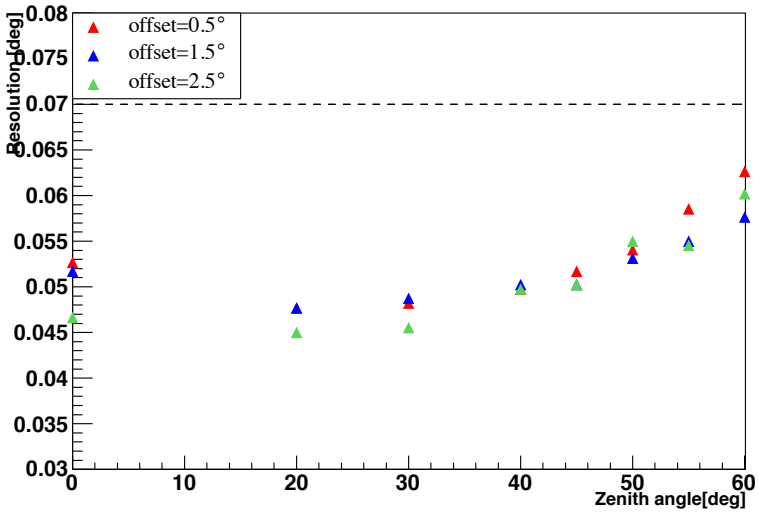

Figure 3.22: Resolution of the $hires_{\zeta,\mathrm{dm}}$ configuration versus zenith angle at different offsets.

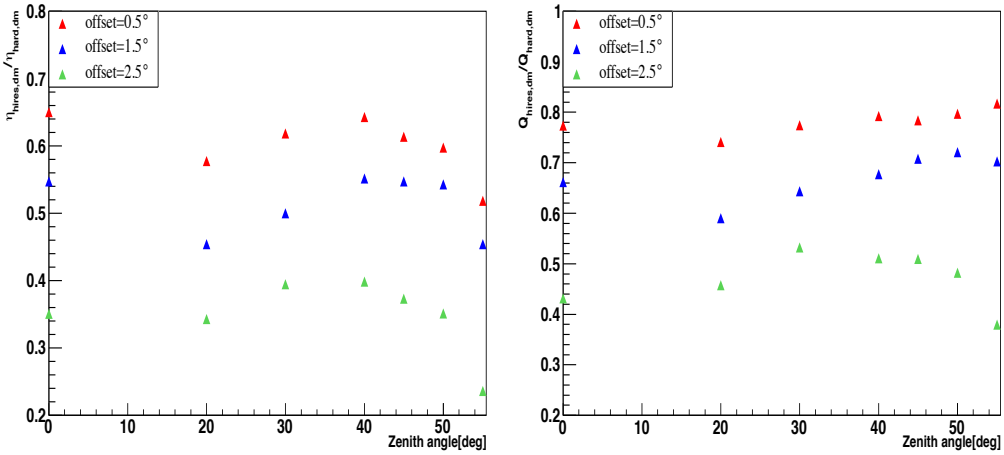

(a) (b)

Figure 3.23: (a) Relative γ efficiency and (b) Relative Q factor versus zenith angle at different offsets of $hires_{\zeta,\mathrm{dm}}$ with $hard_{\zeta,\mathrm{dm}}$ configuration.

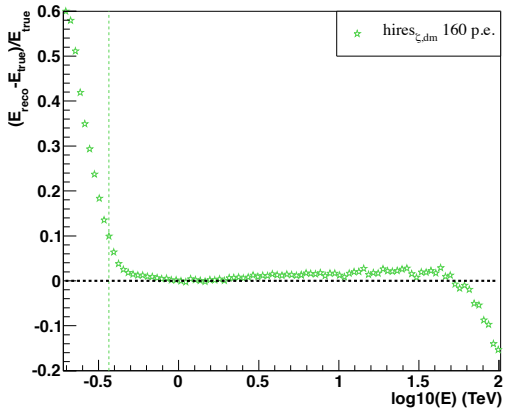

Figure 3.24: Bias in percentage of reconstructed energy versus the true energy. The dashed vertical lines denotes the *safe energy threshold* above which the bias of reconstructed energy is smaller than 10%.

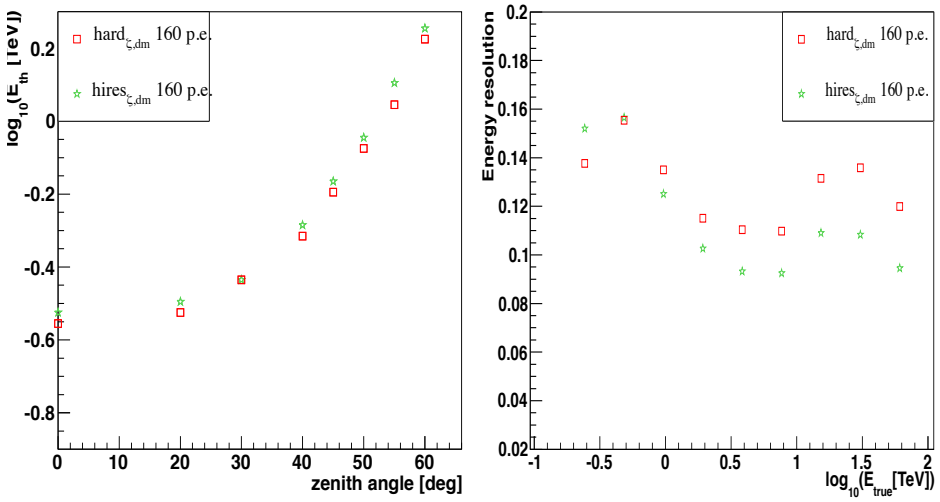

(a) *Safe energy threshold* (b) Energy resolution

Figure 3.25: (a) The *safe energy threshold* as a function of the zenith angle. (b) The energy resolution as a function of the true energy.

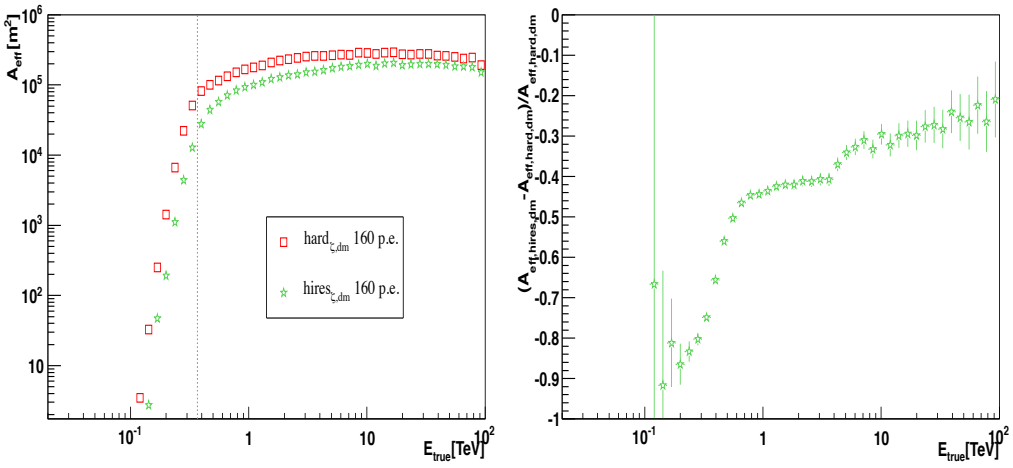

(a) (b)

Figure 3.26: (a) The effective detection area of the $hires_{\zeta,\mathrm{dm}}$ configuration. (b) The difference in the effective detection area between $hard_{\zeta,\mathrm{dm}}$ and $hires_{\zeta,\mathrm{dm}}$ configurations.

3.4 Spectrum fitting for the Crab nebula

The Crab nebula is a young (with an age of $\sim$ 950 years) pulsar wind nebula at a distance of 2 kpc. The VHE γ-ray emission from the Crab nebula was first detected by Whipple in 1989 [Weekes et al., 1989]. Given its relatively high and steady flux, the Crab nebula is commonly use as a standard candle for VHE γ-ray telescopes. For verification of the new analysis, differential energy spectrum reconstruction and fits are performed for different configurations with the dataset similar to the one used in the H.E.S.S. published result of Crab [Aharonian et al., 2006].

The participation of at least three telescopes and the atmospheric quality for spectral analysis are required for the run selection. To avoid the systematic uncertainties at larger offset, the dataset is restricted to the maximum offset of 1.5°. The resultant dataset contains 51 runs with a livetime of 21.48 hours taken between March 2003 and January 2005 (muon phase 1 and 1b) in *wobble mode*. Due to its northern-hemisphere-declination position on the sky ($05^{\mathrm{h}}34^{\mathrm{m}}31.94^{\mathrm{s}}$,22°00′52.20“, J2000), the Crab nebula can only be observed at zenith angles larger than 45°. The range of the zenith angle of this dataset is between 45° to 65° with a mean of 50.4°. The range of the offset angle is between 0.5° to 1.5° with a mean of 0.6°.

The signal and background statistics of all the configurations are summarized in Table 3.5. The significance of the TMVA+DM configuration is improved due to greater γ efficiency resulting from better direction reconstruction. Also note that there are almost no background events after the $hires_{\zeta,\mathrm{dm}}$ cut.

The differential energy spectra is fit with the forward-folding maximum likelihood method. The function used here for the fitting is a power law with an exponential cutoff:

$$\frac{dN_\gamma}{dE} = I_0 \left(\frac{E}{\mathrm{TeV}}\right)^{-\alpha} \exp\left(-\frac{\mathrm{E}}{\mathrm{E_c}}\right). \tag{3.6}$$

The differential energy spectra are presented in Figure 3.27. The fit function with its uncertainty is plotted as the shaded region. As seen in the residual plots, the spectra are well described by the fit function. Note that the data points $\sim 3\sigma$ deviating from the fitted functions in the spectra at 0.5 TeV of *std* configuration and at 1 TeV of *hard* configuration are due to the artifacts in the effective detection area lookup tables as shown in Figure 3.27(f). The TMVA trainings are performed in 6 energy bands which result in the discontinuities on the effective detection area at the boundaries between energy bands. The histograms of effective detection area are fitted with polynomial functions to reduce statistical fluctuations. The fit may fail to describe the histogram when there are too few bins (e.g. in some cases, only two bins) between the *safe energy*

Config.	N_{On}	$N_{\mathrm{Off}} \cdot \alpha$	excess	Sig.$[\sigma]$	Sig.$[\sigma]/\sqrt{t[h]}$
std_{paper}	8601	935	7666	124	27.0
std	8145	958	7187	132	28.5
std_{ζ}	8076	701	7375	144	31.0
$std_{\zeta,\mathrm{dm}}$	8569	504	8065	161	34.8
$hard_{\mathrm{paper}}$	3058	72	2986	94	20.5
$hard$	2781	77	2704	104	22.5
$hard_{\zeta}$	3653	129	3527	116	25.1
$hard_{\zeta,\mathrm{dm}}$	3564	79	3485	121	26.2
$hires_{\zeta,\mathrm{dm}}$	2055	17	2038	104	22.4

Table 3.5: The statistics of γ-ray-like events passing *post-selection* of different configurations. The quantities listed here are defined in Section 2.4. Note that the dataset used here is similar but not completely the same as the dataset used in Aharonian et al. [2006] due to the different calibration and data quality cuts.

threshold and the boundary. Nevertheless, the influence on the spectrum fitting is small.

The best fit parameters are summarized in Table 3.6. All the fit parameters of the *std* configurations are consistent with each other in 2σ. This is also true for the *hard* configurations. Nevertheless, the *hard* configurations have on average softer α and larger $F_{>1\,\mathrm{TeV}}$ as also seen in the published result. The $hires_{\zeta,dm}$ configuration overestimate the differential flux and integrated flux by 10% although the value is still consistent with that of other configurations in 2σ. Despite of similar *safe energy threshold* as the $hard_{\zeta,dm}$ configuration, the effective detection area of $hires_{\zeta,dm}$ configuration changes relatively rapidly as shown in Figure 3.26(a). This behavior suggests that this configuration is not ideal for spectral analysis.

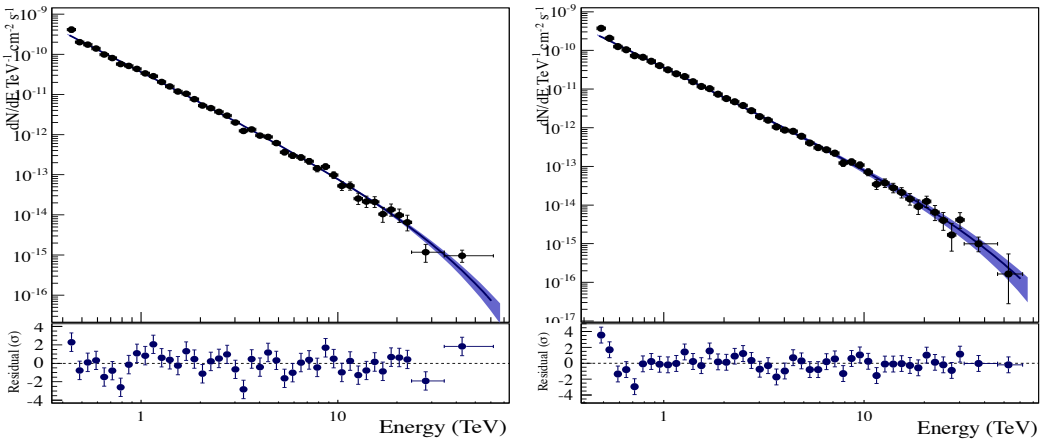

(a) std_{ζ}

(b) $std_{\zeta,\mathrm{dm}}$

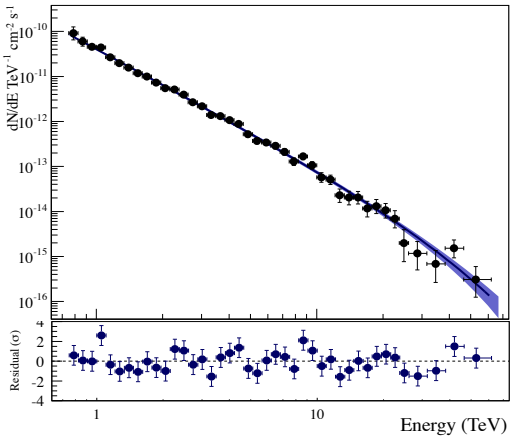

(c) $hard_{\zeta}$

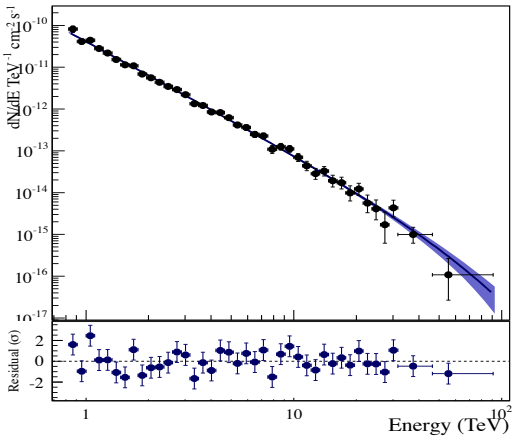

(d) $hard_{\zeta,\mathrm{dm}}$

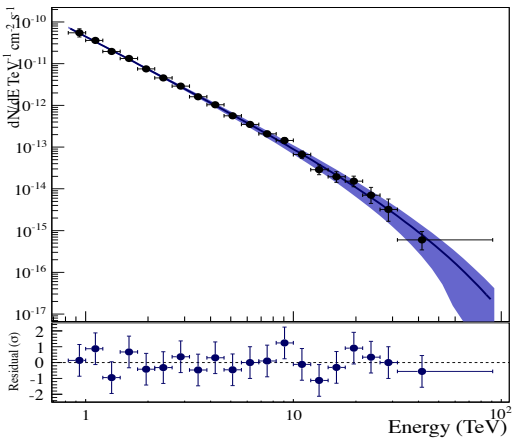

(e) $hires_{\zeta,\mathrm{dm}}$

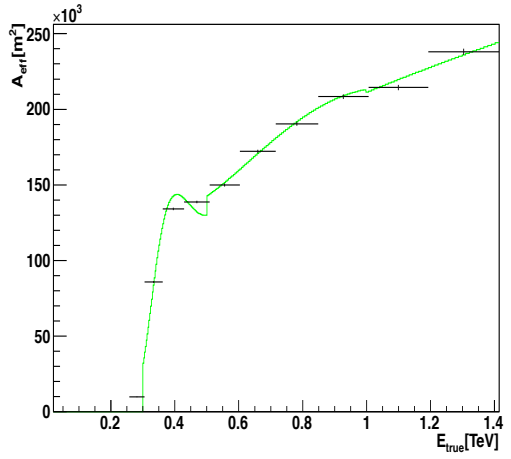

(f) Artifacts in A_{eff} lookup tables

Figure 3.27: Spectra of Crab for different configurations.

Config.	E_{min} [TeV]	$I_0(1\,\mathrm{TeV})$ ($\times 10^{-11}\mathrm{cm}^{-2}\mathrm{s}^{-1}\mathrm{TeV}^{-1}$)	α	E_c [TeV]	$F_{>1\,\mathrm{TeV}}$ ($\times 10^{-11}\mathrm{cm}^{-2}\mathrm{s}^{-1}$)
std_{paper}	0.41	3.76 ± 0.07	2.39 ± 0.03	14.3 ± 2.1	2.26 ± 0.08
std	0.46	3.79 ± 0.06	2.43 ± 0.04	16.8 ± 3.0	2.43 ± 0.04
std_{ζ}	0.42	3.62 ± 0.05	2.47 ± 0.03	19.8 ± 3.7	2.28 ± 0.04
$std_{\zeta,\mathrm{dm}}$	0.46	3.60 ± 0.05	2.52 ± 0.03	25.9 ± 5.2	2.25 ± 0.03
$hard_{\mathrm{paper}}$	0.73	4.06 ± 0.12	2.53 ± 0.05	20.3 ± 4.5	2.36 ± 0.12
$hard$	1.00	4.14 ± 0.17	2.56 ± 0.07	25.1 ± 7.3	2.49 ± 0.12
$hard_{\zeta}$	0.75	4.02 ± 0.14	2.60 ± 0.05	30.1 ± 9.1	2.40 ± 0.17
$hard_{\zeta,\mathrm{dm}}$	0.83	4.11 ± 0.13	2.65 ± 0.05	47.62 ± 19.7	2.40 ± 0.10
$hires_{\zeta,\mathrm{dm}}$	0.83	4.49 ± 0.19	2.57 ± 0.07	29.37 ± 10.1	2.73 ± 0.15

Table 3.6: Fit parameters of the Crab nebula. E_{min} is the minimum energy used in the fitting. $I_0(1\,\mathrm{TeV})$ is the differential flux at 1 TeV,$F_{>1\,\mathrm{TeV}}$ is the integrated flux above 1 TeV, α is the power index of the differential spectrum and E_c is the cutoff energy as defined in Eq. (3.6).

3.5 Position fitting for known sources

The H.E.S.S. PSF lookup tables are generated from Monte-Carlo simulations. How well they can describe the real data is an important issue for morphology studies. The datasets of two known strong sources: the Crab nebula and PKS 2155-304 are used in this work to test the modeling of the PSF. The datasets are selected passing the atmospheric-quality cut for spectral analysis [Hahn, 2012]. The offset angle between the target and the pointing direction is restricted to less than 1° to avoid systematic effects introduced by large offset angles. The whole dataset is divided into small zenith angle bands to investigate the systematic uncertainties on the PSF as a function of the zenith angle.

PKS 2155-304 is a BL Lac-type AGN at a redshift $z = 0.117$. The VHE γ-ray emission from PKS 2155-304 was first discovered by the Mark 6 telescope [Chadwick et al., 1999]. Because of its high flux and the interesting physics behind the highly variable characteristics, H.E.S.S. has conducted regular observations on this source for years and accumulated large amounts of data over a broad range of zenith angles from 0° to 50°. The spectral index of PKS 2155-304 is very soft. The flux and spectral index changes rapidly in the flaring period (see, for example, Aharonian et al. [2005]; H.E.S.S. Collaboration et al. [2010]). The dataset used here excludes all the flaring runs to avoid introducing extra uncertainties for PSF calculation where an assumed spectral index is required.

The expected PSF is calculated with a differential energy spectrum following a power law function with the spectral index taken from the published paper: $\alpha = -2.63$ for the Crab nebula [Aharonian et al., 2006] and $\alpha = -3.53$ for PKS

2155-304 [H.E.S.S. Collaboration et al., 2010]. As discussed in subsection 3.2.1, the dependency of the PSF on the power index is quite mild within $\Delta\alpha \sim 0.6$. The fitting with the PSF calculated with the dataset's own fit spectral index is also tested and does not show large difference from the results presented here.

The fitting is performed with a symmetric Gaussian convolved with the PSF. There are four free parameters in the fitting: the right ascension, declination of the source position, the normalization factor and the extension. The extension of the source is characterized by the fit Gaussian width. Since PKS 2155-304 and the Crab nebula are thought to be point-like, the fit widths are expected to be very close to zero.

The best fit positions of the two sources are plotted in Figure 3.28 and compared with the positions determined by radio observation: ($21^{\rm h}58^{\rm m}52.07^{\rm s}$,$-30°13'32.12''$, J2000) or (329.7169,−30.2256, J2000) [Fey et al., 2004] for PKS 2155-304 and ($05^{\rm h}34^{\rm m}31.94^{\rm s}$,$22°00'52.18''$, J2000) or (83.6331,22.0145, J2000) [Lobanov et al., 2011] for the Crab pulsar. Each data point represents a zenith-angle binned dataset with colors for different configurations. For PKS 2155-304, the best fit positions are consistent with the radio position within $\sim 30''$ and are almost isotropically distributed around the radio position. Figure 3.29 shows that all best fit positions are consistant with the radio position within 2σ statistical uncertainties. The shift between the fit position and the radio position has no dependency on the zenith angle. For the Crab nebula, nevertheless, the best fit positions of all configurations have a tendency to shift towards the Northwest (descending right ascension and increasing declination) to the pulsar position. Figure 3.29 shows that the shifts between the radio position to the fit position are typically $\sim 30''$ and up to $40'' - 55''$ at zenith angles larger than 50°. Combining the data-subsets with zenith angle smaller than 50° yields the best fit positions presented in Figure 3.30 overlapping with the Chandra X-ray map. The best fit positions of all configurations are consistent with each other within 2σ statistical uncertainty with a $25''$ shift northwest to the radio position of the pulsar. The fit Gaussian width characterizing the extension of the source is plotted in Figure 3.31. For PKS 2155-304, the fit widths of the std_ζ configurations are consistent with zero within 2σ statistical uncertainties. The fit widths of the $hard_\zeta$ configurations are slightly larger than of the std_ζ configurations. The possible reason is that configurations with higher angular resolution are more sensitive to the systematic bias. No clear dependency on the zenith angle is seen except the $hires_{\zeta,\rm dm}$ configuration, which has an on-average fit width of $\sim 0.025°$. The possible explanation for this will be addressed later in the discussion section. The fit for the Crab nebula shows a slight extension of $\sim 0.02°$ ($1.2'$) for all configurations. This issue will also be discussed later.

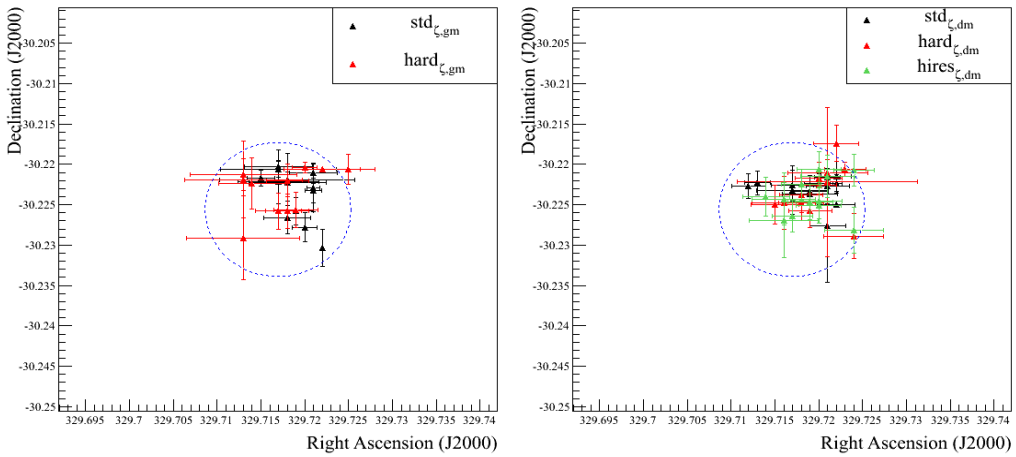

(a) (b)

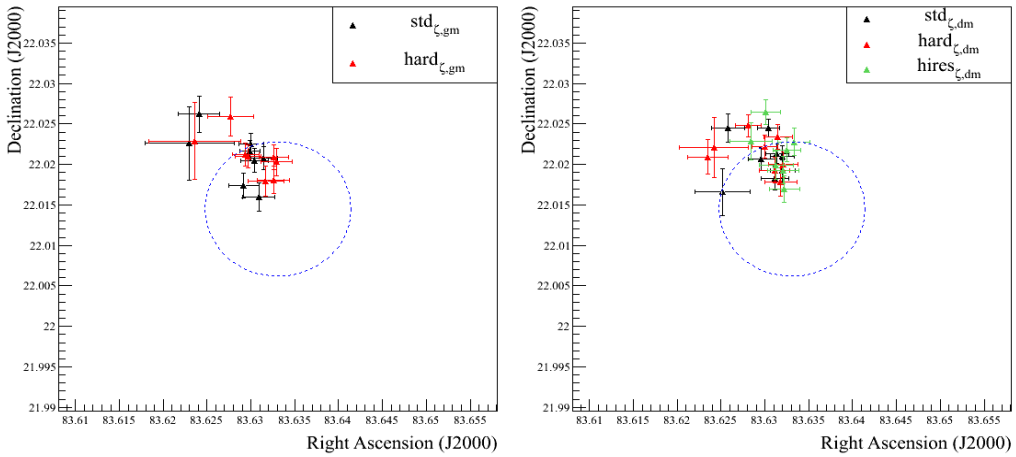

(c) (d)

Figure 3.28: Best fit positions of PKS 2155-304 (upper panel) and the Crab nebula (lower panel). The error bars denotes the 1σ systematic uncertainty and the dashed circle denotes an angular distance of $30''$ to the nominal position.

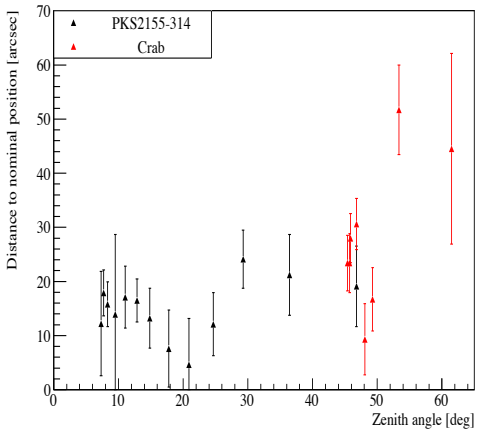

(a) std_{ζ}

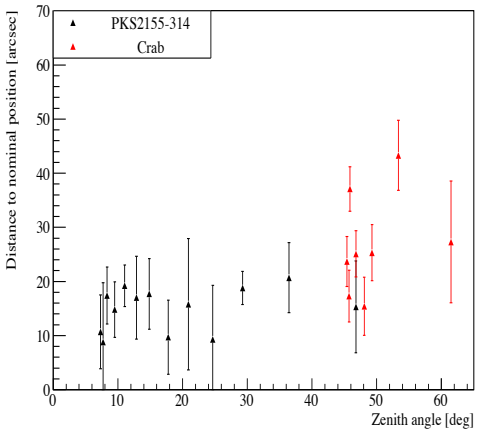

(b) $std_{\zeta,\mathrm{dm}}$

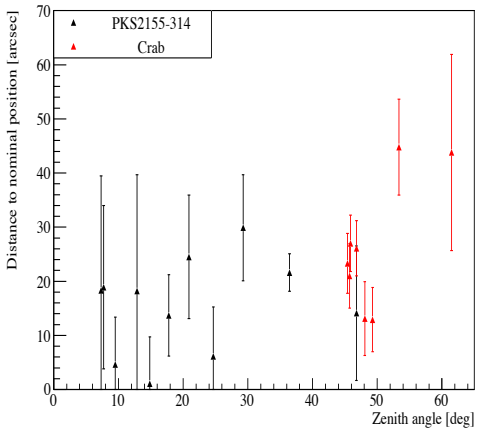

(c) $hard_{\zeta}$

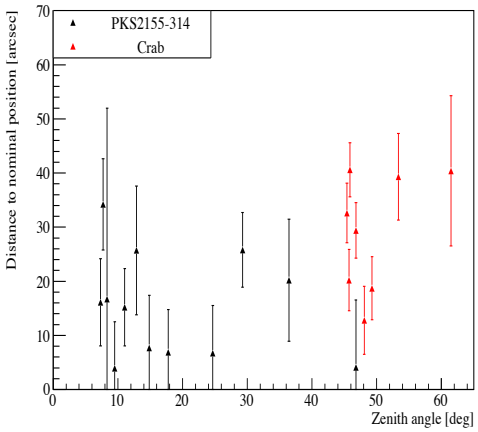

(d) $hard_{\zeta,\mathrm{dm}}$

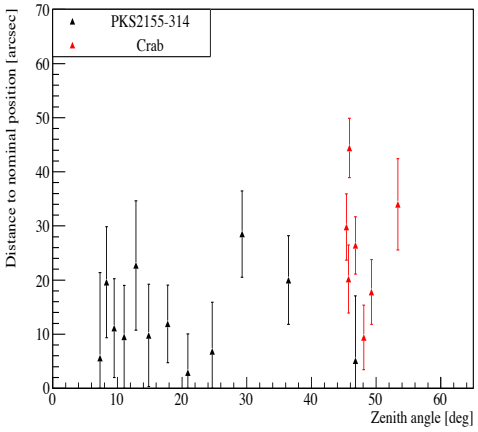

(e) $hires_{\zeta,\mathrm{dm}}$

Figure 3.29: The difference between fit position and nominal position of PKS 2155-304 and the Crab nebula versus the zenith angle.

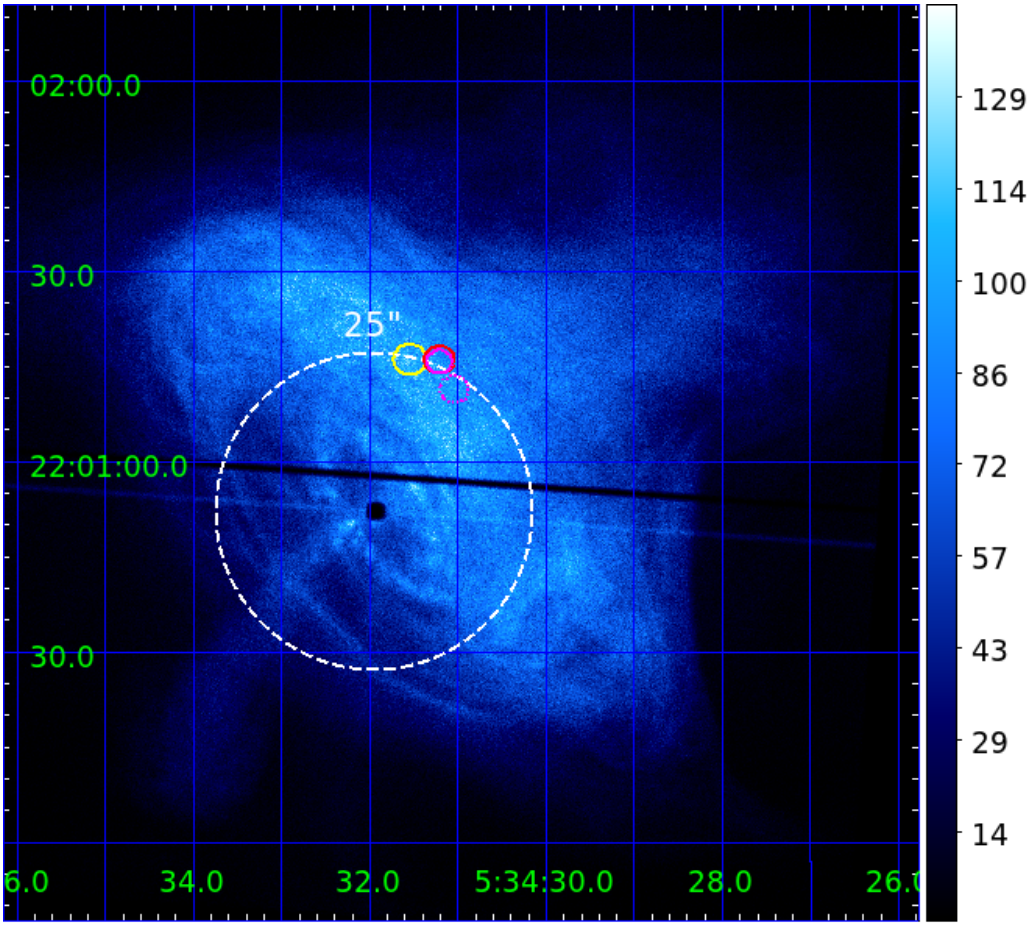

Figure 3.30: Best fit positions of the VHE γ-ray emission from the Crab nebula on top of the $0.3-10$ keV X-ray image in J2000 coordinates by the Chandra satellite. The colored circles denote the best fit positions with different configurations: red solid circle: $hard_{\zeta,\mathrm{dm}}$, red dashed circle: $hard_{\zeta}$, magenta solid circle: $std_{\zeta,\mathrm{dm}}$, magenta dashed circle: std_{ζ}, and yellow solid circle: $hires_{\zeta,\mathrm{dm}}$. The white dashed circle denotes a shift to the radio position of the pulsar of $25''$. X-ray image credit: NASA/CXC/SAO/F. Seward

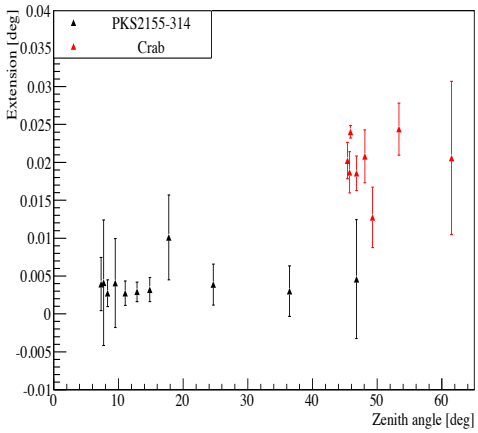

(a) std_{ζ}

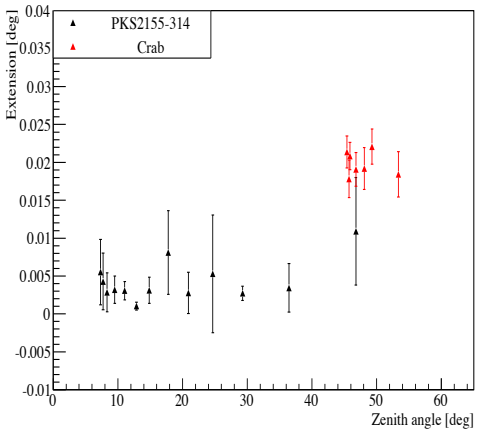

(b) $std_{\zeta,\mathrm{dm}}$

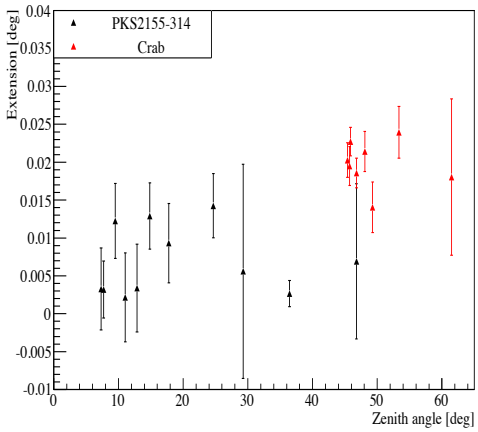

(c) $hard_{\zeta}$

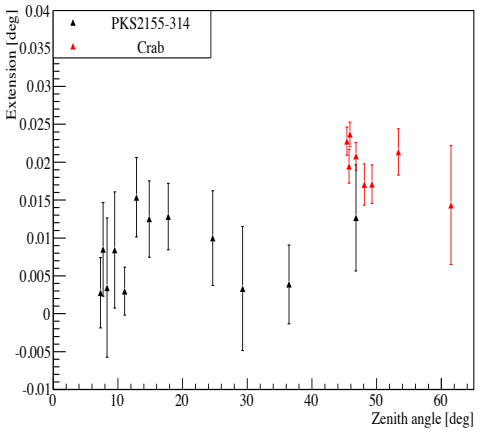

(d) $hard_{\zeta,\mathrm{dm}}$

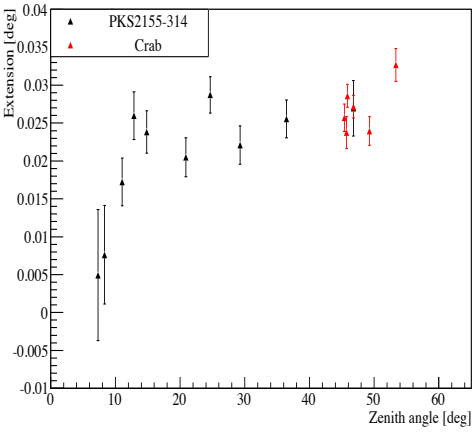

(e) $hires_{\zeta,\mathrm{dm}}$

Figure 3.31: The extension derived by the fittings with a Gaussian convolved with the PSF for PKS 2155-304 and the Crab nebula versus the zenith angle.

3.6 Discussion

3.6.1 The impact of broken pixels on the PSF

The H.E.S.S. PSF is modeled by Monte-Carlo simulations under the assumption of a perfectly functioning instrument. In reality, camera pixels may be switched off intentionally to avoid the light from bright stars or due to hardware problems. These deactivated pixels are called broken pixels and will be ignored in data analysis. An observation run is excluded when more than 10% of the total 960 pixels in a camera are broken. Broken pixels due to hardware problems usually arise as a group while a drawer or an Analogue Ring Sampler (AMS) does not function. Compared with randomly-distributed broken pixels, a group of adjoining broken pixels will have larger impact on the data analysis because in these cases the Hillas parameters could be incorrectly calculated. Figure 3.33 shows two Monte-Carlo simulated events with and without including broken pixels.

In the upper panel, one can see the orientation of the Hillas ellipse of this event is much rotated due to the broken pixels, and in the lower panel for another event with a small image size, the hillas *length* and *size* are much reduced.

It is suggested by Sanchez and Marandon [2012] that broken pixels may have an impact on the performance of PSF. This bias on the parameterization is expected to have larger impact on the $hires_{\zeta,\mathrm{dm}}$ configuration where an extra cut on the direction uncertainty is applied. Figure 3.32 shows the θ^2 distributions of events from a Monte-Carlo simulated point source. A considerable amounts of events from the head of the distribution are lost due to broken pixels, resulting a poorer PSF. Figure 3.34(a) shows that with the presence of broken pixels, the direction uncertainty distribution is also slightly distorted. Although the difference is not very large, given the small angular resolution of $hires_{\zeta,\mathrm{dm}}$ configuration, it introduces up to a 15% increase on the PSF size as shown in Figure 3.34(b). The increase on the PSF size shows a mild dependency on the zenith angle, peaking at 45°. This effect is much more significant for $hard_{\zeta,\mathrm{dm}}$ and $hires_{\zeta,\mathrm{dm}}$ configurations than the $hard_{\zeta,\mathrm{dm}}$ configuration, with a good agreement with the increasing fit width seen in Figure 3.31.

3.6.2 The position and extension of the emission from the Crab nebula

A large fraction of H.E.S.S. sources in the galactic plane are related to pulsar wind nebulae. It is believed that the main contribution to the VHE γ-ray emission of these sources originate from the pulsar wind nebula instead of the pulsar. Until now, pulsed VHE γ-ray emission is only been observed from Crab pulsar by MAGIC above 25 GeV [Aliu et al., 2008] and VERITAS above 100 GeV [VERI-

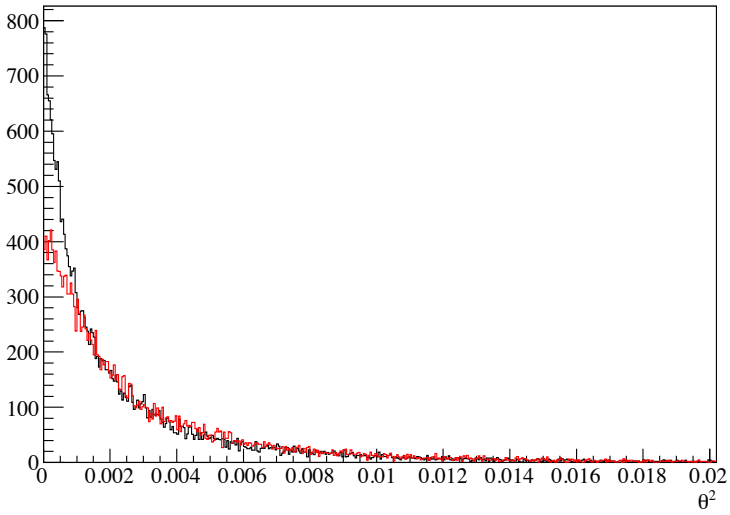

Figure 3.32: θ^2 distributions of events from a Monte-Carlo simulated point source at 45° zenith angle and 0.5° offset with (red) and without (black) broken pixels.

TAS Collaboration et al., 2011]. The flux from the pulsar is quite low ($\sim 1\%$ of the total Crab flux) compared with the the flux from the nebula. The spectrum is best fit with a power law with an exponential cut-off. A simple power law fit gives a very soft spectral index of ~ -3.8. The extension of the Crab nebula is about $3'$ in diameter in the X-ray band [Weisskopf et al., 2000] and $6'$ in diameter in the radio band. The extension observed in the X-ray and radio band does not neccessarily reflect the extension in the VHE γ-ray band, but given these facts it will not be surprising to find the VHE γ-ray emission slightly extended or shifted from the pulsar position. Nevertheless, these conclusions can not be easily drawn with the available data and studies. It is not clear if the extension and shifted position seen in this work originates from systematic bias which are still under investigation.

Although it is shown in section 3.5 that the fit width of the Crab nebula is slightly larger than the fit width of PKS 2155-304, one has to keep in mind that these two sources have quite different spectral indices: -2.6 versus -3.5 respectively, which may lead to different sensitivities to the systematic bias. Furthermore, the large spread in observation time may also introduce different systematic effects due to the instrument's varying condition such as the change of the optical efficiency. The observation on PKS 2155-304 is mostly performed at less than 40° zenith angles. The data point at 47° in Figure 3.31 contains only 38 runs corresponding to a livetime of 18 hr and thus has quite large statistical

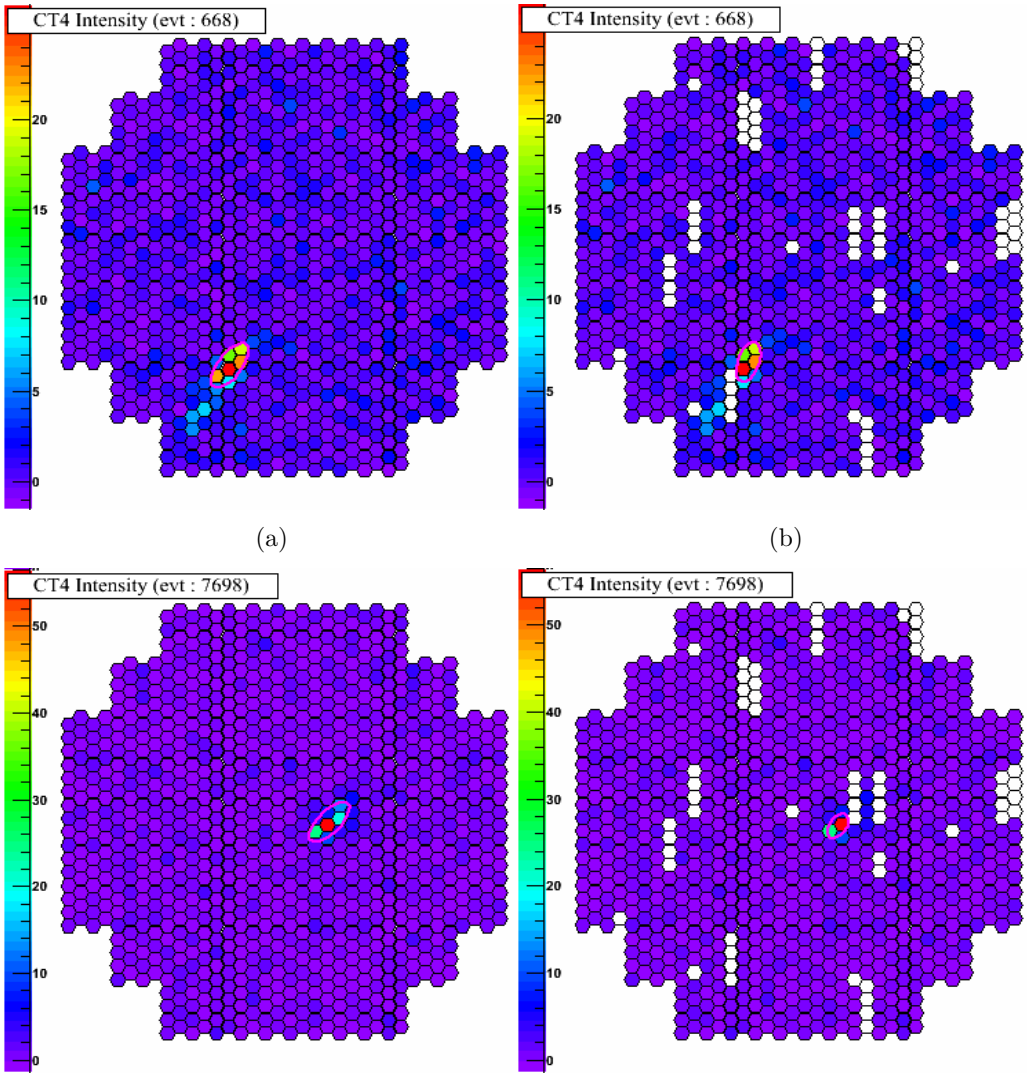

(a) (b)

(c) (d)

Figure 3.33: Shower images of two Monte-Carlo events of CT4, without broken pixel (left) and with the broken pixel pattern of the run 47997 (right). The blue ellipse is the Hillas ellipse of the image with the size doubled for visibility purposes. Taken from [Sanchez and Marandon, 2012].

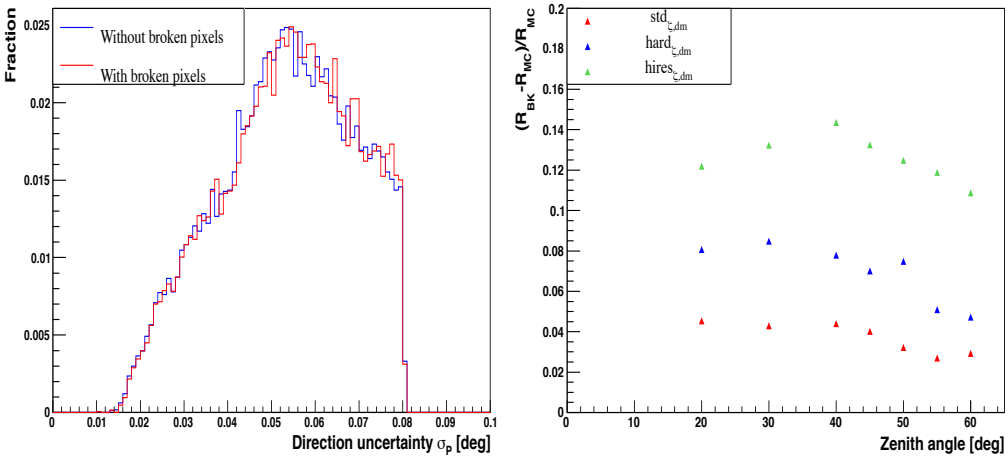

(a) Direction uncertainty distribution

(b) Difference in angular resolution

Figure 3.34: (a) Direction uncertainty distributions with/without broken pixels. The upper bound of the distribution is the direction uncertainty cut of $hires_{\zeta,\mathrm{dm}}$ configuration. (b) The difference in angular resolution versus zenith angle of Monte-Carlo simulated events with/without broken pixels. R_{MC} is the angular resolution calculated without broken pixels and R_{BK} is the angular resolution calculated with broken pixels.

uncertainty. More dedicated observation of these two sources under similar observation conditions will probably reduce the influence of the systematic effects and help to provide a clearer interpretation on the nature of the VHE γ-ray emission from the Crab nebula.

Chapter 4

VHE γ-ray observation on the Large Magellanic Cloud

4.1 The origin of VHE γ rays

VHE γ-ray production can be separated into two kinds of categories: by top-down processes such as the decay of heavy particles, and by interactions of accelerated high energy charged particles (i.e. nuclei or electrons) with the ambient matter and radiation field. The first category is beyond the scope of this work and the second one is discussed here.

4.1.1 Particle acceleration

In 1949, Fermi [Fermi, 1949] proposed the so-called *second order Fermi acceleration* mechanism. In this theory, charged particles are reflected by magnetized clouds serving as magnetic mirrors moving randomly with the speed u through the interstellar medium (ISM). The detailed calculation can be followed, for example, in Longair [1992b]. To summarize, particles only gain energies through head-on collisions. Because the probability of head-on collisions is slightly larger than the tail-on collisions, the resulted average change in particle energy per cycle (two collisions) is a gain:

$$\frac{\Delta E}{E} = \frac{8}{3}\left(\frac{u}{c}\right)^2. \tag{4.1}$$

As the gain in energy is second order in u/c, this process is not sufficiently efficient to accelerate particles to the observed energies of $\mathcal{O}$(PeV) within the given lifetime of the expected accelerators such as supernova remnants (SNRs) and pulsar wind nebulae (PWNs).

The efficiency of the process can be enhanced in strong shock waves in the

SNRs and PWNs. The following description follows the derivation in Longair [1992b]. This process is conventionally called as the *first order Fermi acceleration* because the gain in energy is first order in u/c.

Assuming a SNR shock wave with speed u much larger than the speed of sound moving through the ISM, under the fully-ionized monatomic gas assumption, the adiabatic index 5/3 yields a compression ratio of 4. To fulfill the mass conservation condition, the densities and velocities of gas in the shock's upstream (unshocked) and downstream (shocked) region are related by:

$$\frac{v_u}{v_d} = \frac{\rho_d}{\rho_u} = 4, \tag{4.2}$$

so

$$v_d = \frac{1}{4} v_u = \frac{1}{4} u. \tag{4.3}$$

In the downstream rest frame, the particles in the upstream region are traveling with the velocity of $V = \frac{3}{4}u$ across the shock front, colliding head-on and gaining energies. After crossing the shock front, particles are scattered by the random irregularities in the magnetic field so that their velocity distributions become isotropic with respect to the flow. The situation observed from the rest frame of upstream is exactly the same. The average energy gain per cycle in this scenario is:

$$\frac{\Delta E}{E} = \frac{4}{3}\frac{V}{c}, \tag{4.4}$$

and the ratio between the new energy and original energy is:

$$\frac{E'}{E} = 1 + \frac{4}{3}\frac{V}{c} = 1 + \frac{u}{c} \equiv \beta \tag{4.5}$$

For planar shocks, particles in the upstream region do not leave the acceleration process, but the ones in the downstream region are gradually swept away from the shock. The probability of particles staying in the acceleration site after one cycle is

$$P = 1 - \frac{u}{c}. \tag{4.6}$$

Assuming initially, there are N_0 particles with an energy E_0. After j cycles, the number and energy of the particles evolve as: $N = N_0 P^j$ and $E = E_0 \beta^j$. Combining these two equations, one will find

$$\frac{N}{N_0} = \left(\frac{E}{E_0}\right)^{\frac{\ln P}{\ln \beta}}. \tag{4.7}$$

Thus the energy distribution of accelerated particles follows a power-law:

$$\frac{dN}{dE} \sim E^{-\alpha} \qquad \text{with}\, \alpha = 1 - \frac{\ln \mathrm{P}}{\ln \beta} \sim 2\, \text{as}\, \frac{\mathrm{u}}{\mathrm{c}} \ll 1. \tag{4.8}$$

The scenario described above is simplified. The acceleration process in reality could be much more complicated. For example, as will be discussed in the case of SN 1987a, the shock is considered to be modified by the accelerated cosmic rays and the magnetic field is amplified, making the acceleration more efficient due to the larger diffusion rate.

4.1.2 Hadronic scenario of VHE γ-ray production

High-energy protons and nuclei interact with the nuclei in the ambient medium produce π-mesons. The charged pions decay into muons and neutrinos and the neutral pion (π^0) decays into two γ rays. The production rate of γ rays depends on the proton-proton ($p-p$) collision cross-section and the ambient target density. Under the simplified assumption that all proton-proton collision result in only π productions, and 1/3 of the remaining energy is given to a π^0, which splits into two photons. The γ-ray production rate is associated with the $p-p$ collision cooling time τ_{pp}, after which on average every proton loses $1-1/e$ of the initial energy, namely, $E(t) = E_0 e^{-t/\tau_{\mathrm{pp}}}$. With the ambient medium density n_0, the $p-p$ collision cross-section σ_{pp}, and $f \sim 0.5$ for taking into account that half of the primary energy is carried away by the nucleon,

$$\tau_{\mathrm{pp}} = \frac{1}{n_0 \sigma_{\mathrm{pp}} f c} \tag{4.9}$$

For protons with energies above a few GeV, $\sigma_{\mathrm{pp}} \sim 35\,\mathrm{mb}$ is only logarithmically dependent on the energy, and the cooling time is given by Hinton and Hofmann [2009]:

$$\tau_{\mathrm{pp}} \sim 3 \cdot 10^7 \left(\frac{n_0}{1\mathrm{cm}^{-3}}\right)^{-1} \mathrm{yr}. \tag{4.10}$$

The total energy in the accelerated protons W_p can be then calculated by

$$W_p = L_\gamma \cdot 3 \cdot \tau_{\mathrm{pp}}, \tag{4.11}$$

where L_γ, the γ-ray luminosity, can be obtained by the observed γ-ray flux F_γ and the known distance D of the source:

$$L_\gamma = 4\pi D^2 F_\gamma. \tag{4.12}$$

4.1.3 Leptonic scenario of VHE γ-ray production

Inverse Compton radiation

When energetic electrons interact with the ambient photon field, low energy photons can be up-scattered to very high energies through the inverse Compton (IC) process. The process is characterized by the Klein-Nishina cross-section:

$$\sigma_{\rm KN} = \pi r_e^2 \frac{1}{\varepsilon}\left\{\left[1-\frac{2(\varepsilon+1)}{\varepsilon^2}\right]\ln(2\varepsilon+1)+\frac{1}{2}+\frac{4}{\varepsilon}-\frac{1}{2(2\varepsilon+1)^2}\right\}, \tag{4.13}$$

where $\varepsilon = \hbar\omega/m_e c^2$ and r_e is the classical electron radius. When the photon energy in the center of mass frame is much lower than the rest mass of the electron, namely, $\varepsilon \ll 1$, the Klein-Nishina cross-section becomes almost independent of energy and equals to the Thomson cross-section :

$$\sigma_{\rm KN} = \frac{8\pi}{3} r_e^2 (1-2\varepsilon) \sim \frac{8\pi}{3} r_e^2 = \sigma_T. \tag{4.14}$$

In the ultra-relativistic limit, it becomes

$$\sigma_{\rm KN} = \pi r_e^2 \frac{1}{\varepsilon}(\ln 2\varepsilon + \frac{1}{2}). \tag{4.15}$$

The cross-section reduces roughly with $1/\varepsilon$. The main target fields for electrons with energies of $1-100$ TeV are the Cosmic Microwave Background (CMB, $kT \sim 2.35 \cdot 10^{-4}$ eV), far infrared radiation such as the diffuse galactic dust background ($kT = 0.02$ eV), and the optical star light ($kT = 1.5$ eV). For higher energy target photons, the cross-section is strongly suppressed as known as the *Klein-Nishina effect*.

In the Thomson limit, an electron of energy E_e scattering off a target photon of energy E_T yields a up-scattered photon with an energy of:

$$E_{\rm IC} \sim 5 \left(\frac{E_T}{1{\rm meV}}\right)\left(\frac{E_e}{1{\rm TeV}}\right)^2 {\rm keV}. \tag{4.16}$$

The energy loss rate of an electron with velocity v via this process under a radiation field with an energy density $U_{\rm rad}$ is, according to the derivation in Longair [1992b]:

$$\frac{dE}{dt} = \frac{4}{3}\sigma_T c U_{\rm rad} \frac{v^2}{c^2}\gamma^2, \tag{4.17}$$

where γ is the electron Lorentz factor. In the Klein-Nishina regime, the inverse

scattering cooling time, according to Moderski et al. [2005], can be calculated by:

$$\tau_{\rm IC} = 3.1 \cdot 10^5 f_{\rm KN}^{-1} \left(\frac{U_{\rm rad}}{1{\rm eV\,cm^{-3}}} \right)^{-1} \left(\frac{E_e}{1{\rm TeV}} \right)^{-1}, \tag{4.18}$$

where $f_{\rm KN}$ is the Klein-Nishina suppression factor approximated as:

$$f_{\rm KN} \sim \left[1 + 40 \left(\frac{E_e}{1{\rm TeV}} \right) \left(\frac{kT}{1{\rm eV}} \right) \right]^{-1.5} \ {\rm for} \frac{4{\rm E_e E_T}}{{\rm m_e^2 c^4}} < 10^4, \tag{4.19}$$

where T is the black-body temperature of the radiation field. This correlation allows the determination of the magnetic field strength when $U_{\rm rad}$ is known.

Synchrotron radiation

When an electron with energy E_e travels in a magnetic field of strength B, it is deflected and emits synchrotron radiation with energy $E_{\rm syn}$:

$$E_{\rm syn} = 0.2 \left(\frac{B}{10\mu{\rm G}} \right) \left(\frac{E_e}{1{\rm TeV}} \right)^2 {\rm eV}, \tag{4.20}$$

with an energy loss rate

$$\frac{dE}{dt} = \frac{4}{3} \sigma_T c U_{\rm mag} \frac{v^2}{c^2} \gamma^2, \tag{4.21}$$

where $U_{\rm mag} = B^2/2\mu_0$ is the energy density of the magnetic field. The synchrotron cooling time is:

$$\tau_{\rm syn} = 1.3 \cdot 10^7 \left(\frac{B}{1\mu G} \right)^{-2} \left(\frac{E}{1{\rm TeV}} \right)^{-1} {\rm yr}. \tag{4.22}$$

These two equations are very similar to Eq. (4.16) and (4.17) because these two processes actually follow the same Feynman diagram. Combining Eq. (4.16) and (4.20), one can get the correlation between the energy of the IC scattered photon and synchrotron photon by an electron with energy E_e:

$$E_{\rm syn} \approx 0.07 \left(\frac{E_{\rm IC}}{1{\rm TeV}} \right) \left(\frac{B}{10\mu{\rm G}} \right) {\rm keV}. \tag{4.23}$$

The ratio of the energy fluxes at energies related by Eq. (4.23) can be calculated as:

$$\frac{F_{\rm IC}}{F_{\rm syn}} = \frac{U_{\rm rad}}{U_B}. \tag{4.24}$$

With the assumption that the IC and synchrotron emission comes from the same electron population, the magnetic field strength in the source can be determined

by this relation when the target radiation field is known.

SED of IC and synchrotron photons

According to Eq. (4.16) and (4.20), the photon energy scales with the parent electron energy. The IC and synchrotron spectrum is thus harder than the electron spectrum. Assuming isotropic distributions of electrons and photons, electrons with a power-law energy distribution $N_e(E) \sim E_e^{-\Gamma_e}$ will generate a IC spectrum of an index $\Gamma_\gamma = (\Gamma_e + 1)/2$ in the Thomson regime and a synchrotron spectrum of the same shape at lower energies. In the Klein-Nishina regime, the IC spectrum will be steepen by $\Delta\Gamma_\gamma = (\Gamma_e + 1)/2$. Thus, the IC spectrum generated by a power-law distributed electron population will have a break corresponding to the transition to the Klein-Nishina regime.

The shape of SEDs get more complicated when electron cooling is considered. Energy losses due to IC and synchrotron processes will modify the electron spectrum above the energy where the corresponding cooling time gets comparable with the age of the electron population. Assume a continuous electron injection with a power law distribution: $N_e(E) \sim E_e^{-\Gamma_i}$. In the case where the synchrotron loss or IC loss in the Thomson regime dominate, the energy loss of electrons can be expressed as $(dE/dt)_{\rm sync+IC} = -\kappa E^2$. After time T, the cooling effect will introduce a spectral break in the electron energy distribution at the energy $E = 1/(\kappa T)$, the energy where the radiative lifetime equals the age T, with the index above this energy increasing by 1 [Kardashev, 1962] and a break with index change $\Delta\Gamma_\gamma = 1/2$ in IC and synchrotron spectra at the corresponding energies calculated with Eq. (4.16) and (4.20).

In the case where the IC loss dominates, another break will be introduced in the Klein-Nishina regime by the reduced electron energy loss. The spectrum will be harder than the one discussed above, with $\Gamma_e \approx \Gamma_i + 1 + \Delta\Gamma$, where $\Delta\Gamma \approx -1.5 \sim -1$, and $\Gamma_\gamma \approx \Gamma_i$. Since the IC loss scales slower than E_e^2, the synchrotron loss will dominate above a certain energy again, causing another break with $\Gamma_\gamma \approx \Gamma_i + 2$.

Figure 4.1 shows the time-evolved SEDs of IC and synchrotron photons generated by a population of electrons with an E^{-2} injection spectrum and an exponential cutoff at 100 TeV. The features discussed above can be seen in this figure.

4.2 The Large Magellanic Cloud

The Large Magellanic Cloud (LMC) is a satellite galaxy of the Milky Way with the estimated distance to the Earth of about 48 kpc [Macri et al., 2006]. Figure

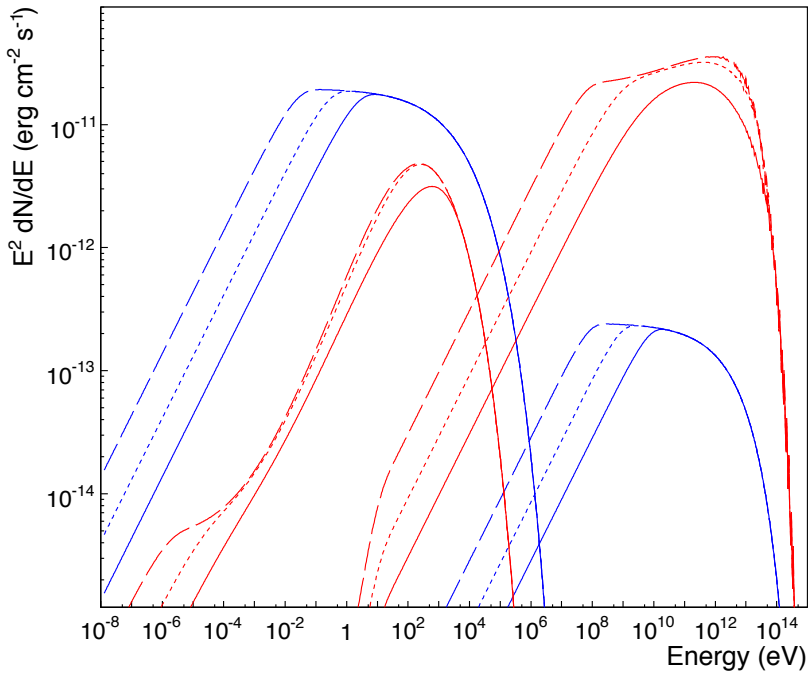

Figure 4.1: SEDs for continuous injection and cooling of a population of electrons with an E^{-2} injection spectrum and an exponential cutoff at 100 TeV. Solid, short-dashed and long-dashed curves show injection timescales of 10^4 years, 3×10^4 years, and 10^5 years, respectively. The blue curves show synchrotron and IC emission in the case of synchrotron-dominated cooling, with $B = 30\,\mu$G and the CMB radiation as the target for IC. The red curves illustrate the effects of IC-dominated cooling with a lower magnetic field $B = 3\,\mu$G and a higher-energy radiation field: black-body photons with $kT = 1.5\,$eV, and energy density 1000 eV cm-3 where Klein-Nishina effects become important. Taken from Hinton and Hofmann [2009].

4.2 shows the optical image of LMC. It has an apparent extension of about 10° and an inclination angle of 31° [Nikolaev et al., 2004].

The EGRET telescope first detected GeV γ-ray emission from the LMC with an integrated γ-ray flux of $(1.9 \pm 0.4) \times 10^{-7} cm^{-2} s^{-1}$ above 100 MeV [Sreekumar et al., 1992]. Due to the limited angular resolution, no individual object or structure of the emission could be resolved. The 11-month data from Fermi satellite detects an integrated γ-ray flux of $(2.6 \pm 0.2) \times 10^{-7} cm^{-2} s^{-1}$ above 100 MeV. The emission peaks at the 30 Doradus (also known as the Tarantula Nebula, 30 Dor, or NGC 2070) region. No point source can be identified for the contribution to the emission. Cosmic-ray interactions with the interstellar medium and radiation field are considered as the possible origin for the observed emission [The Fermi/LAT collaboration and Abdo, 2010].

The 30 Dor region as indicated by the white box in Figure 4.2 is the most luminous extragalactic HII-region in the local group. It centers on ($05^{\mathrm{h}}38^{\mathrm{m}}38^{\mathrm{s}}, -69°05'42''$, J2000) or ($l = 279.459°, b = -31.679°$, Gal.), with a size of $40' \times 25'$ [Bica et al., 1999]. Given the known distance to the Earth and intensive observations at other wavelengths, this region is ideal for studying the activities of high energy particles. Figure 4.3 shows the Chandra X-ray image of the 30 Dor region. As labeled in the figure, X-ray emission is found from several objects in this region: The young supernova remnant SN 1987a, the superbubble 30 Dor C, the supernova remnant N 157B, the star cluster RMC 136. Given that non-thermal X-ray emissions are usually an indication of high energy particle interactions, these X-ray emitters are good candidates of VHE γ-ray emission.

4.3 The H.E.S.S. dataset and analysis

The H.E.S.S. observations of the LMC start from 2003. The initial purpose of the observation was to investigate the very young supernova remnant SN 1987a. The observations were carried out using the 3-telescope system in November and December of 2003 while the construction of CT1 was not finished yet. Due to trigger problems of CT3, only images from CT2 and CT4 were usable for reconstruction. The result with a livetime of 3.44 hours (8 runs) was presented by Rowell et al. [2005].

As shown in Figure 3.2, a low multiplicity yields a poor point spread function. Since now the dataset has been significantly expanded, 2-telescope runs are excluded in the current analysis. The dataset used in this work starts from December of 2004 until January of 2012, focusing on the 30 Dor region. The observations are conducted during the rain season (October till next February) in Namibia. In total, 564 runs were taken, of which 497 runs pass the data quality cut but only 391 runs corresponding to a livetime of 169 hours remain after the

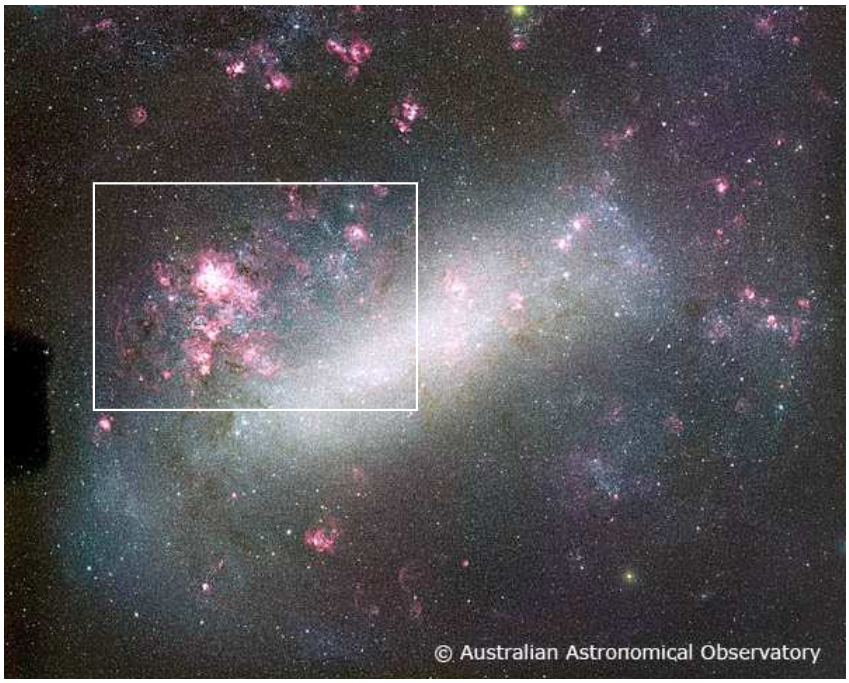

Figure 4.2: The optical image of the whole LMC. The white box indicates the region where H.E.S.S. observations focus. Credit: Australian Astronomical Observatory.

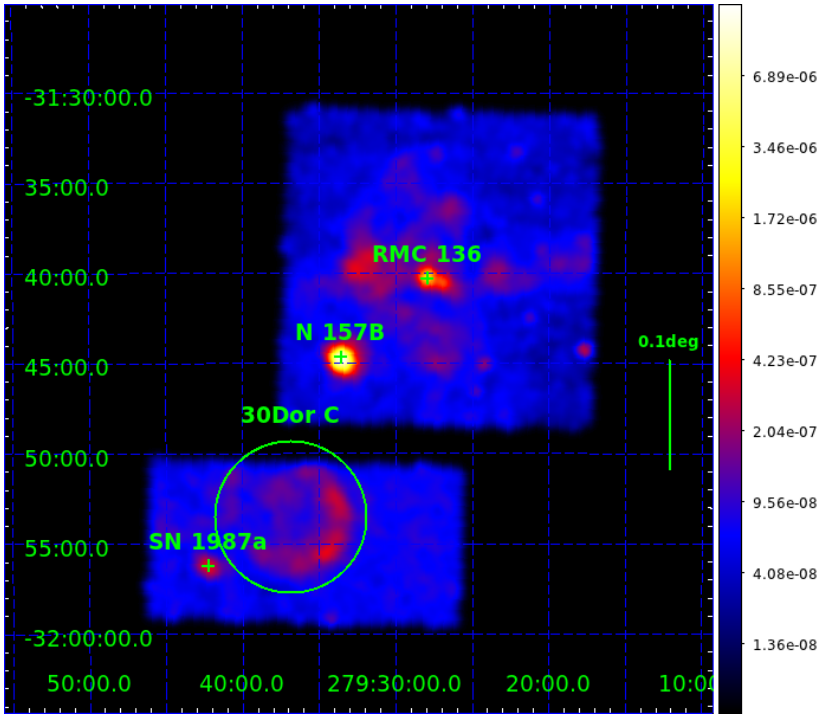

Figure 4.3: The X-ray Chandra image of the 30 Dor region. The X-ray emitters are labeled: The young supernova remnant SN 1987a, the superbubble 30 Dor C, the supernova remnant N 157B, the star cluster RMC 136

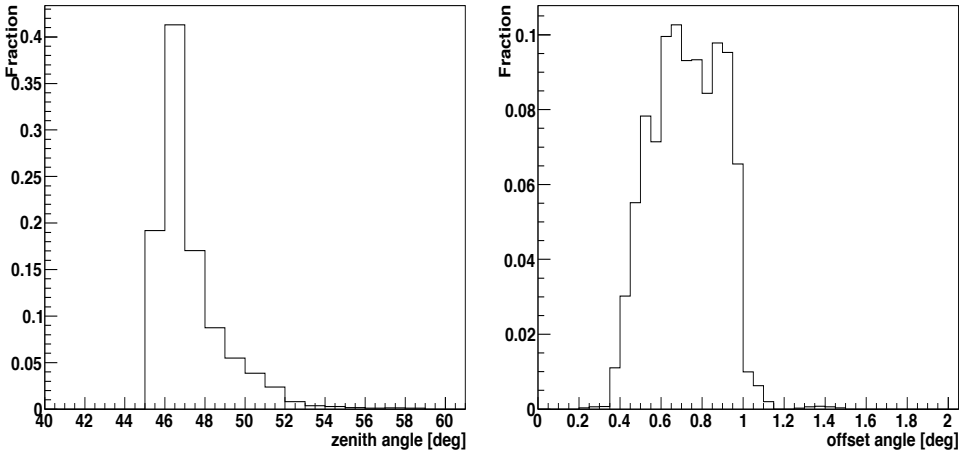

(a) zenith angle distribution (b) offset angle distribution

Figure 4.4: Zenith and offset angle distribution of events in a 0.1° circle centering on the position of PSR J0537-6910, the central pulsar in N 157B, which is one of the main targets in the H.E.S.S. observations of the 30 Dor region.

Config.	$E_{\rm th}$[TeV]	Resolution$_{\rm MC}$[deg]
std_{ζ}	0.75	0.147
$std_{\zeta,\rm dm}$	0.75	0.109
$hard_{\zeta}$	1.0	0.096
$hard_{\zeta,\rm dm}$	1.0	0.075
$hires_{\zeta,\rm dm}$	1.30	0.057

Table 4.1: Energy threshold and angular resolution of the LMC observation for different configurations.

atmospheric-quality cut for spectral analysis [Hahn, 2012]. The observation was conducted in the *wobble mode* with an offset of 0.7° around the position of the 30 Dor region, resulting a smooth exposure on the interested region. Due to its high declination, this region is only visible at large zenith angles. The zenith angle and offset angle distribution of the events in the region of interest are plotted in Figure 4.4. The dataset has a mean zenith angle of 47° and a mean offset angle of 0.68°, yielding the safe energy thresholds and angular resolutions as listed in Table 4.1 for different analysis configurations. The *Ring background method* and *Reflected background method* are used to derive the sky map and differential energy spectra. The inner ring radius is chosen to be 0.6°. Two exclusion regions are used to avoid signal contamination: a circular area with a radius of 0.3° at

the N 157B region and a circular area with a radius of 0.25° at the N 132D region.

The overall H.E.S.S. maps of the 30 Dor region of all the configurations are presented in Figure 4.5 and 4.6. The region is at a high declincation ($\sim -69°$, J2000), all images are produced with the Galactic coordinate system to avoid image distortion by the projection effects at high declinations. A bright emission is found at the position of the supernova remnant N 157B. The nature of the emission will be discussed later. No point-like emission is seen in the direction of SN1987a. An upper limit on this target will be derived.

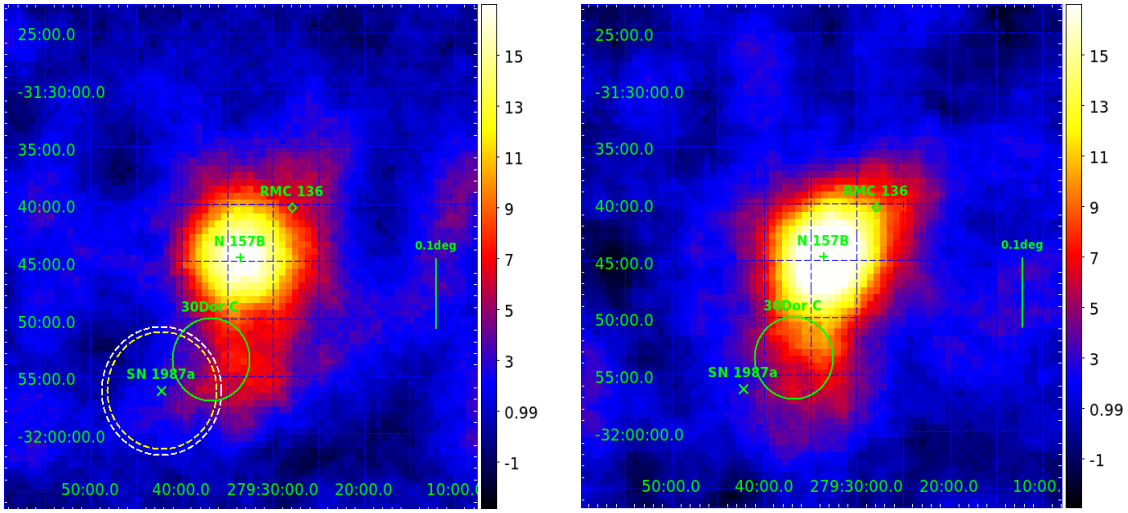

(a) std_{ζ}

(b) $std_{\zeta,\mathrm{dm}}$

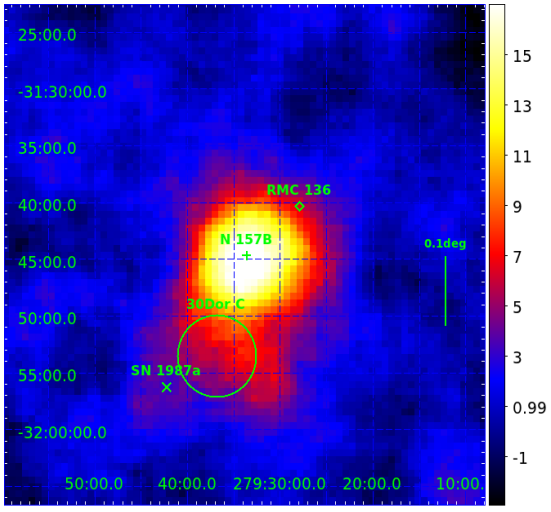

(c) $hard_{\zeta}$

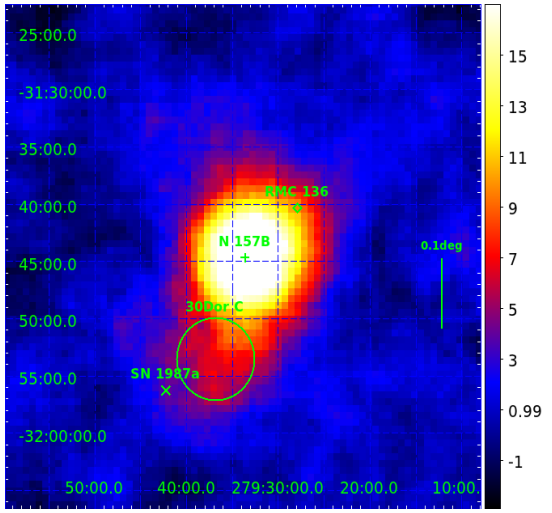

(d) $hard_{\zeta,\mathrm{dm}}$

Figure 4.5: The significance map in Galactic coordinates for *std* and *hard* configurations of the 30 Dor region. The significance is calculated with a correlation radius of 0.07°.The white and yellow dashed circle in (a) denotes the *On-region* for the *std* and *hard* configurations.

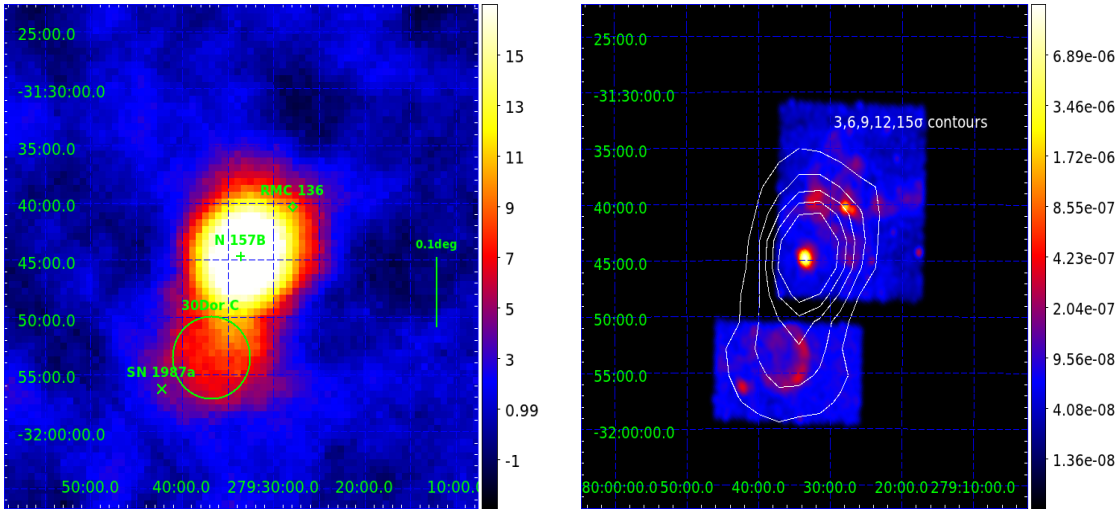

(a) $hires_{\zeta,\mathrm{dm}}$ (b) $hires_{\zeta,\mathrm{dm}}$ contours with X-ray image

Figure 4.6: (a) The significance map in Galactic coordinates for the $hires_{\zeta,\mathrm{dm}}$ configuration of the 30 Dor region. The significance is calculated with a correlation radius of 0.07°. (b) The contours corresponding to the map in (a) overlapping with the Chandra X-ray image.

4.4 The young supernova remnant SN 1987a

SN 1987a, a very young supernova remnant, was discovered independently by Ian Shelton at the University of Toronto Southern Observatory, Oscar Duhalde at the Las Campanas observatory in Chile, and Albert Jones, Nelson in New Zealand (IAU Circular 4316) at the night of February. 24th, 1987, one day after the first light of its explosion reached the Earth. Figure 4.7 shows the optical image before and after the explosion. The apparent brightness after discovery started from a magnitude of about 5, peaked in May at about 3. and started declining in the following months. It was the first time that astronomers have the chance to monitor the spatial evolution of a close-by and bright supernova remnant in its early stages. The progenitor star, the blue supergiant Sanduleak $-69 \circ 202$ was also observed before its explosion, which provides an understanding on the object's ambient environment.

Since discovery, this object has been extensively studied by modern instruments in every band of the electromagnetic spectrum. It was also the first time that the neutrino burst from a supernova explosion was detected [Koshiba et al., 1987]. Figure 4.8 shows the images of SN 1987a in radio, optical and X-ray wavelengths. The supernova remnant has a shell-like feature, with X-ray and radio emission peaking just inside the optical inner ring. The radio and X-ray emis-

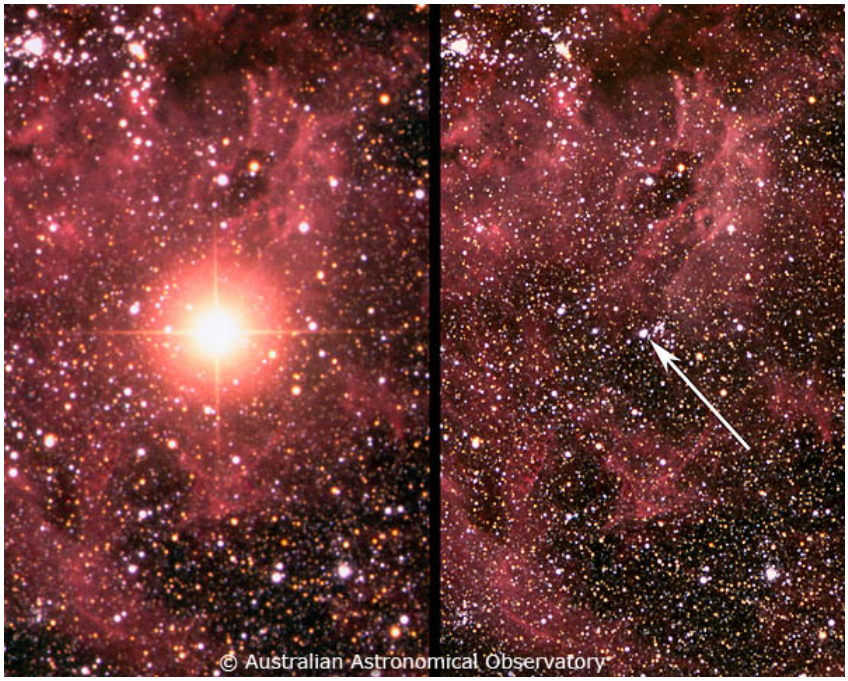

Figure 4.7: The field around SN 1987a before (right panel) and after (left panel) the explosion. In each image, the top-left is the North-West and the width of each image is about $8'$. The image in the right was taken in February 5th 1984 where the progenitor star Sanduleak $-69 \circ 202$ was labeled by the white arrow and the one in the left was taken in March 8th 1987, about 15 days after the explosion. The difference in image quality between these two photos is due to the effect of the Earth's atmosphere. Credit: Australian Astronomical Observatory, photographed by David Malin.

sion is interpreted as the synchrotron emission from the heated TeV electrons downstream of the outer SN shock. The concentration of the highest energy electrons in a very thin shell just behind the shock indicates the presence of a strong magnetic field [Berezhko and Ksenofontov, 2006].

4.4.1 Theoretical prediction of the VHE γ-ray flux

Radio and X-ray spectral energy distributions (SED) are fitted to theoretical models to give predictions on the VHE γ-ray flux by Berezhko and Ksenofontov [2000], Berezhko and Ksenofontov [2006], and Berezhko et al. [2011], hereafter referred to as BK2000, BK2006, and BK2011 respectively. In these studies, an approximate spherically symmetric model of the pre-explosion environment of

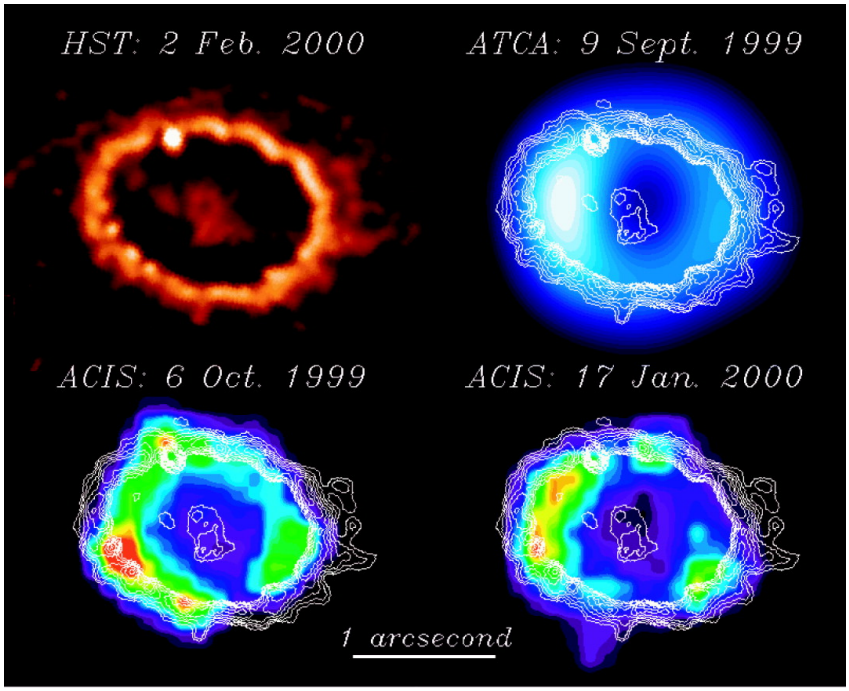

Figure 4.8: Top left: The optical Hubble Space Telescope image colored with log scaling taken on 2000 February 2nd. Top right: The deconvolved radio ATCA 8 GHz image colored with square-root scaling taken on 1999 September 9th. Bottom left: The deconvolved X-ray ACIS (Advanced CCD Imaging Spectrometer) image colored with linear scaling taken on 1999 October 6th. Bottom right: The deconvolved X-ray ACIS image with linear scaling taken on 2000 January 17. The images were made with identical pixel size and the orientation with North to the up side. The contour overlays in the top right-hand panel and in the bottom panels are the optical ring from the top left-hand panel. Taken from Burrows et al. [2000].

SN 1987a is assumed, combined with a spherically symmetric nonlinear model for the nonthermal evolution which couples the particle acceleration process with the hydrodynamics of the thermal gas. The model predictions show a hadronic dominant VHE γ-ray emission from SN 1987a at the observable level for H.E.S.S.. These predictions vary slightly according to the improvement of the models and the increase of observation data.

In the BK2000 work, only the radio data are used to fit the model. The extra-soft radio spectral index, $\alpha \approx 1$ compared with $\alpha \approx 0.5$ of a typical SNR suggests the shock is strongly modified by the accelerated cosmic rays. The proton injection rate, defined as the fraction of protons of the swept-up medium injecting into acceleration, is required to be as large as $\eta \sim 10^{-2}$ to reach the degree of shock modification. The prediction of the continuous increase of radio emission with a roughly constant rate during the period from 1999 to 2006 is also confirmed by further measurements. In the BK2006 work, radio data for a more extended period together with the Chandra X-ray measurements are used. The X-ray data provide a strong constraint on the amount of the nonthermal synchrotron emission at the energies of $0.5 - 10$ keV which provides the evidence of strongly amplified magnetic field inside the SNR and a better fit of radio data than in the previous study.

A renormalization factor, f_{re}, is introduced in this work to renormalize the hadronic SED. This factor takes into account a more realistic geometry in the circumstellar environment and reduces the number of accelerated CRs calculated with the spherically symmetric approach: Nuclear particles can only be effectively injected into the diffusive acceleration process in regions where the shock normal makes an relatively small angle with the local upstream magnetic field direction. The value of f_{re} is considerably smaller than unity and may introduce an acknowledged uncertainty in the predicted overall γ-ray flux. Following the previous analyses of other SNRs, $f_{re} = 0.2$ is chosen in this work, and the predicted flux is thus a factor of 5 lower than the BK2000 prediction. BK2011 work extends the previous studies by including more subsequent radio and X-ray data. Furthermore, as the injection parameters are assumed being constant in the previous work, their temporal evolution is considered in this work. Substantial time variations of these parameters are expected since the SN shock propagates through a strongly nonuniform circumstellar material (CSM) whose physical parameters at the shock front are expected to change with time. Their values are determined from the fit to the measured synchrotron data and the time-dependent VHE γ-ray flux is predicted as shown in Figure 4.9. The γ-ray emission at the current epoch is dominated by the π^0-decay hadronic origin. Since the SN shock is strongly modified, the γ-ray spectrum at energies larger than 0.1 TeV is very hard: $F_\gamma \propto \epsilon_\gamma^{-0.8}$.

The integral γ-ray flux F_γ above 1 TeV at the current epoch is $F_\gamma(> 1\,\mathrm{TeV}) \approx$

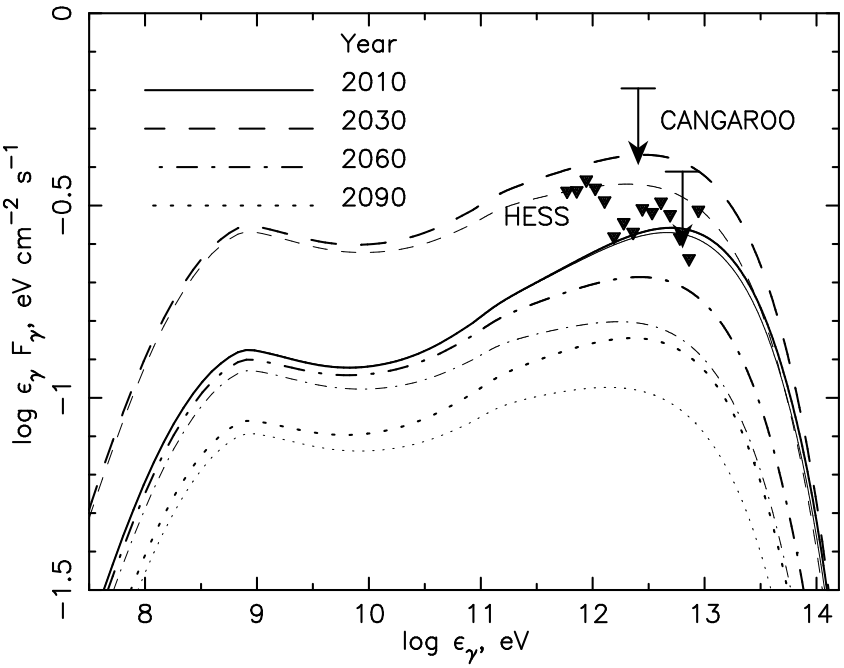

Figure 4.9: Integral γ-ray energy flux from SN 1987a, calculated for four epochs and compared with the CANGAROO [Enomoto et al., 2007] and H.E.S.S. [Komin, 2010] upper limits. The quantity in the y-axis is the threshold energy ϵ times the integral γ-ray flux F_γ above this energy threshold. The H.E.S.S. upper limits plotted here are calculated with the dataset of a 47-hr livetime, much shorter than the 169-hr livetime in this work. Taken from [Berezhko et al., 2011].

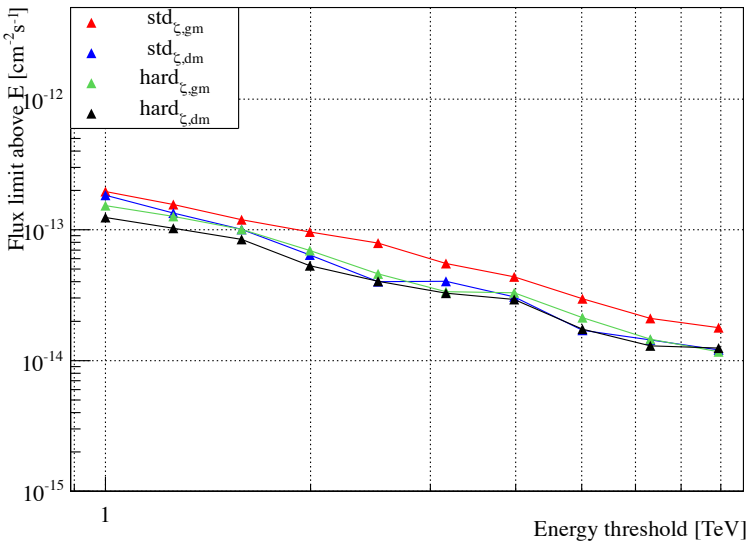

Figure 4.10: H.E.S.S. integral γ-ray flux upper limits on SN 1987a. The upper limits are calculated at the 99% confidence level.

$2.2 \times 10^{-13}\,\mathrm{cm}^{-2}\mathrm{s}^{-1}$. The flux is expected to grow a factor of about two during the next 20 years and then decrease with the decreasing CSM density. $F_\gamma(t)$ is sensitive to the radial profile of the actual CSM density distribution. If the dense shell, which in the spherically symmetric model represents the matter contained in the equatorial ring, is situated at a larger distance, the γ-ray flux is expected to be smaller and the peak of the flux is expected to occur later.

4.4.2 Upper limit on the VHE γ-ray flux of SN 1987a

Table 4.2 summarizes the statistics of γ-ray-like events in the SN 1987a region of the dataset described in Section 4.3. The *On-regions* used to calculate the upper limits are plotted in Figure 4.5(a): The white and yellow dashed circle denotes the *On-region* for the *std* and *hard* configurations. The positive excess and significance may result from the contamination from nearby sources. The resultant upper limits are thus conservative. Figure 4.10 shows the H.E.S.S. upper limits calculated with different configurations. The upper limits of the integral γ-ray flux above 1 TeV are roughly at the same magnitude of the theoretical predictions while taking into account the uncertainties from model parameters [Voelk, 2013].

.

Config.	Max θ^2 [deg^2]	N_{On}	$N_{\mathrm{Off}} \cdot \alpha$	Excess	Significance [σ]	FluxUL(>1 TeV) ($\times 10^{-13}$cm^{-2}s^{-1})
std_{ζ}	0.0125	3941	3700	241	3.8	2.1
$std_{\zeta,\mathrm{dm}}$	0.0125	2729	2465	264	5.0	1.9
$hard_{\zeta}$	0.01	903	751	152	5.2	1.8
$hard_{\zeta,\mathrm{dm}}$	0.01	501	409	92	4.3	1.4

Table 4.2: The statistics of γ-ray-like events passing *post-selection* in the SN 1987a region. The quantities listed here are defined in Section 2.4.

4.5 The pulsar wind nebula in N 157B

N 157B is a supernova remnant embedded in an HII region generated by the OB association LH 99. The Chandra image of the N 157B region is shown in Figure 4.12. N 157B is a Crab-like supernova remnant with the pulsar PSR J0537-6910 situated in its center powering the pulsar wind nebula. PSR J0537-6910 has a characteristic age of 5000 years and a high spin-down power $\dot{E} = 4.9 \times 10^{38}\mathrm{erg\,s^{-1}}$ [Manchester et al., 2005; Marshall et al., 1998], the most energetic pulsar ever known. The PWN consists of a $0.6\,\mathrm{pc} \times 1.7\,\mathrm{pc}$ barlike feature surrounding the pulsar and a $> 5\,\mathrm{pc}$ tail. The bar represents the reverse shock of a toroidal wind from PSR J0537-6910 and the tail is thought to be a pulsar wind bubble elongated because of the pulsar motion.

Pulsar wind nebulae (PWNs) accounts for most of the population of H.E.S.S. sources. The energy output of a PWN typically amounts to $\mathcal{O}(10^{49}\,\mathrm{erg})$, relatively small compared to the energy output in a supernova shock of $\mathcal{O}(10^{51}\,\mathrm{erg})$. Nevertheless, a large fraction of the energy in PWNs is carried by relativistic electrons accelerated up to PeV energies which efficiently convert the kinetic energy into radiation through emitting synchrotron X-rays and IC VHE γ rays. Although the unprojected distance to the star cluster RMC 136 is unknown, the angular distance between them is only 0.1°. Far infrared photons from RMC 136 and LH 99 provide an additional target radiation field other than the CMB for the IC scattering.

Powerful pulsars can drive PWNs for a long time, making them detectable in X-ray and γ-ray band up to an age of $\sim 10^5$yr. The X-ray and TeV emission from a PWN should be tightly linked if they originate from the same population of electrons. Nevertheless, in the PWN population study for example by Kargaltsev and Pavlov [2010], it is found that TeV PWN sizes generally increase with the pulsar age while the X-ray PWN sizes show an opposite trend. It is also indicated that the TeV size of older pulsars with an age larger than 10 kyr is usually $100 - 1000$ times larger than the size of the X-ray PWN while for young pulsars the difference in size is a factor of a few.

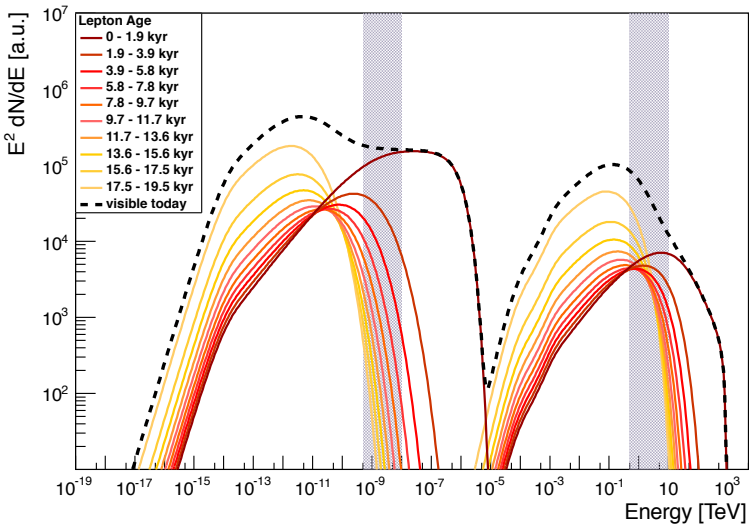

Figure 4.11: Photon SED (black broken line) of a 20 kyr old PWN decomposed into contributions by leptons from different injection epochs (solid colored lines). The gray areas denotes the energy ranges covered by current X-ray and VHE γ-ray observatories. This plot is taken from Mayer et al. [2012].

The modeling of X-ray and TeV emission from evolved PWNs is studied by Mayer et al. [2012]. Figure 4.11 shows an example of the SED from an evolved PWN with the age of 20 kyr, initial period $P_0 = 30$ms and magnetic field $B_0 = 50\mu$G. Contributions to the SED by leptons from different epochs are calculated. It shows that mainly the youngest leptons account for the observed X-ray emission while the TeV emission reflect the whole injection history of the pulsar. The reason is explained as follows: The energy of the leptons generating the synchrotron radiation in the observed X-ray regime is higher than the energy of the leptons generating the TeV IC emission. Since the electron cooling process is more efficient at higher energies, the number of higher-energy leptons are significantly reduces in the older lepton population. Therefore, for the older lepton population, the synchrotron peak is shifted to lower energies out of the observational X-ray range. Since the X-ray emission traces mainly the freshly injected leptons which are more concentrated to the center pulsar while the TeV emission also traces cooled and aged leptons which may have propagated away from the pulsar, the TeV PWN sizes of old PWNs are usually much larger than the X-ray PWN sizes.

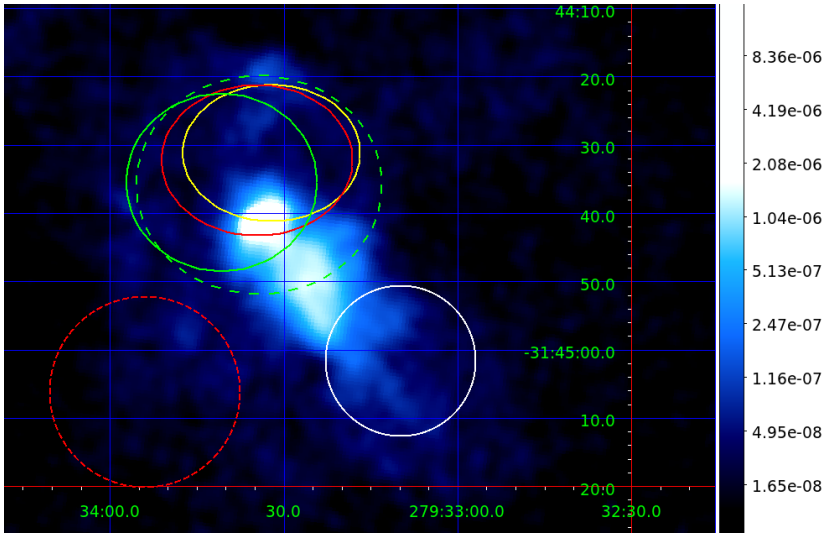

Figure 4.12: The best fit positions of the second source on top of the Chandra image of N 157B. Each ellipse denotes the 1σ statistical uncertainty on the fit position. Green solid: $std_{\zeta,\mathrm{dm}}$. Green dashed: std_{ζ}. Red solid: $hard_{\zeta,\mathrm{dm}}$. Red dashed: $hard_{\zeta}$. Yellow solid: $hires_{\zeta,\mathrm{dm}}$. White solid: From paper.

4.5.1 H.E.S.S. observation on N 157B

Considering the young age (5000 yr) of N 157B with the discussion above, one can argue that the size of TeV emission from the PWN should be only slightly larger than the size of X-ray emission. Given the X-ray PWN size of 1.4 pc [Kargaltsev and Pavlov, 2010], the expected TeV PWN size should certainly be smaller than 140 pc which corresponds to 11″ or 0.003° at a distance of 48 kpc. The source size is much smaller than the H.E.S.S. PSF and can be considered as a point source. With the point-like source assumption, the best fit positions to the emission seen in Figure 4.5 are plotted in Figure 4.12, overlapped with the X-ray image. The fit coordinates are consistent with the position of the pulsar wind nebula. The standard optimized θ^2 cut for point sources are used to extract the spectrum of the emission from N 157B. The statistics of γ-ray-like events in the *On-region* are listed in table 4.3. The differential energy spectra are presented in Figure 4.13 and the fit parameters for the spectra are listed in Table 4.4. The values from the published 2012 paper [H.E.S.S. Collaboration et al., 2012] with another analysis chain (*Model analysis* [de Naurois and Rolland, 2009]) are also listed for comparison. Note that the dataset used in the paper is different from the one used in this work. The dataset in this work has a much longer livetime and is selected with a different data quality cut with a different DST. The obtained

Config.	Max θ^2[deg^2]	$N_{\rm On}$	$N_{\rm Off} \cdot \alpha$	excess	Sig.[σ]
std_{ζ}	0.0125	4909	3747	1162	17.5
$std_{\zeta,\rm dm}$	0.0125	3508	2410	1098	20.2
$hard_{\zeta}$	0.01	1310	760	550	17.5
$hard_{\zeta,\rm dm}$	0.01	876	400	476	19.8
$hires_{\zeta,\rm dm}$	0.005	325	75	250	20.6
paper(2012)	0.01	395	169	226	14.0

Table 4.3: The statistics of γ-ray-like events passing *post-selection* of different configurations in the N 157B region.

Config.	$E_{\rm min}$ [TeV]	$I_0(1\,\rm TeV)$ ($\times 10^{-13}$cm^{-2}s^{-1}TeV^{-1})	α	$F_{1-10\,\rm TeV}$ ($\times 10^{-13}$cm^{-2}s^{-1})
std_{ζ}	0.62	10.5 ± 0.8	2.6 ± 0.1	6.4 ± 0.4
$std_{\zeta,\rm dm}$	0.75	9.6 ± 0.7	2.6 ± 0.1	5.8 ± 0.3
paper(2012)	0.60	8.2 ± 0.8	2.8 ± 0.2	4.6 ± 0.3

Table 4.4: Fit parameters for the differential energy spectra of N 157B. $E_{\rm min}$ is the minimum energy used in the fitting. $I_0(1\,\rm TeV)$ is the differential flux at $1\,\rm TeV$,$F_{1-10\,\rm TeV}$ is the integrated flux between $1-10\,\rm TeV$, α is the power index of the differential spectrum.

γ-ray fluxes are consistent with each other within 20% systematic uncertainties.

With the integrated γ energy flux and the known distance, the total energy in the PWN can be calculated with the hadronic and leptonic scenario. Since the results in this work are consistent with the 2012 paper, the fit of model to the data is not repeated. The derived total energy and birth rate from the paper are quoted here. The expected total energy with a pure hadronic origin $W_{\rm had} = 1.8 \times 10^{52} (n/\rm cm^{-3})^{-1}$erg requires an ambient density of at least $100\,\rm cm^{-3}$ to produce this emission by a single supernova explosion. Since the SNR is expected to expand into the low-density interiors of a superbubble, this density is too high to be possible. With the leptonic scenario, the required energy stored in electron, depending on different model assumptions, is $2 \sim 4 \times 10^{49}$ erg. This number leads to a birth period of the pulsar as short as less than 10 ms, the shortest birth period ever inferred for a pulsar.

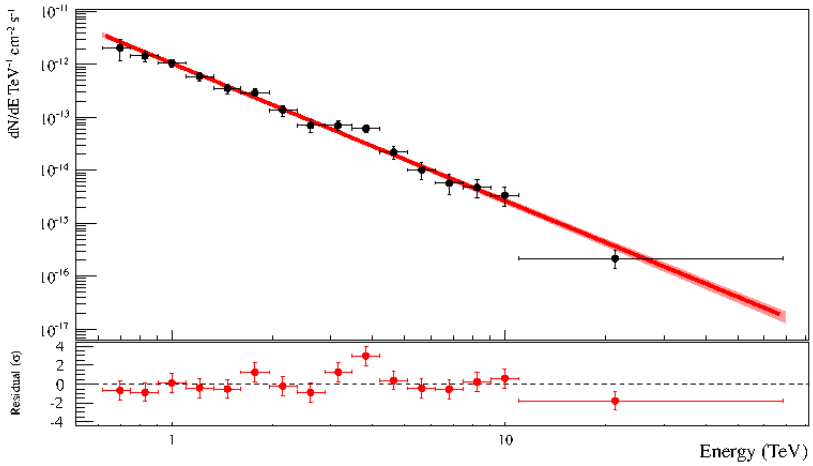

(a) std_{ζ}

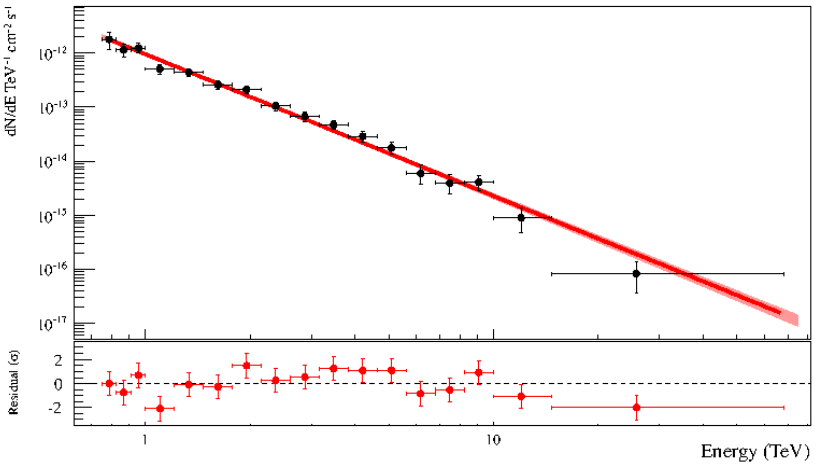

(b) $std_{\zeta,\mathrm{dm}}$

Figure 4.13: Differential spectra of the N 157B region extracted by the *std* configurations. The spectra are fit with a pure power law and the best fit parameters are listed in Table 4.4.

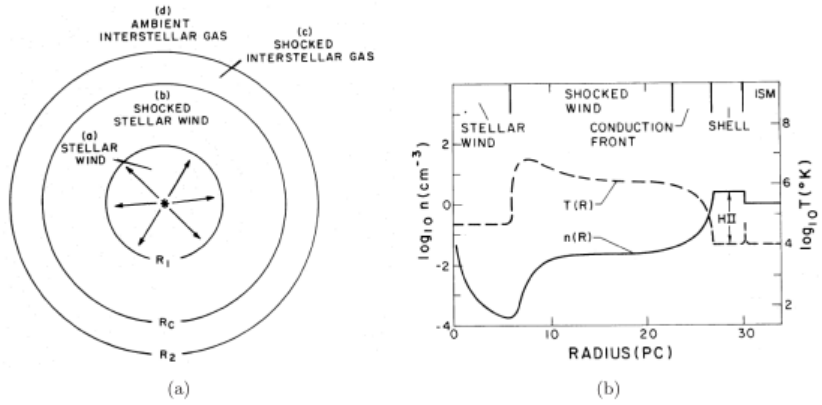

Figure 4.14: (a) A schematic diagram for an interstellar bubble. (b) Density and temperature profiles of a bubble blown by an O7-type star after 1 Myr. Taken from [Weaver et al., 1978].

4.6 The source associated with the superbubble 30 Dor C

4.6.1 The formation of a superbubble

Most massive stars (i.e. O and B stars) are formed in groups by the collapse of giant molecular clouds with typical sizes of $10-30$ pc [de Geus, 1991]. Although these stars are not gravitationally bound , they will always stay close to their birth place and remain concentrated before explosion because they do not have time to acquire large dispersion velocities during the short lifetime of $3-20$ Myr [Schaller et al., 1992] to escape. They thus form OB associations which contains typically several tens of O and B stars within regions of a radius of $R_{\rm OB} \sim 35$ pc [Bresolin et al., 1999; Garmany, 1994; Pietrzyński et al., 2001]. For evenly distributed stars, each star can be considered as occupying an individual spherical volume of a radius [Parizot et al., 2004],

$$R_* \sim 6 \frac{R_{\rm OB}}{35{\rm pc}} \left(\frac{N_{\rm OB}}{100} \right)^{-1/3} {\rm pc}. \tag{4.25}$$

OB stars blow strong stellar winds during most of their lifetime with the total wind energy integrated over their lifetime amounts to 10^{51} erg, which is comparable to a supernova explosion energy. According to the standard wind bubble theory by [Weaver et al., 1978], an interstellar bubble blown by a massive star has the structures shown in Figure 4.14. The development of the bubble can be

described as follows: In the first $\mathcal{O}(10^3)$ yrs, the bubble goes through a very rapid expansion where radiative losses do not have enough time to affect the structure and evolution of the system. Later, the system goes into a semi-adiabatic phase, where radiative losses cause the pushed-away material to collapse, forming a thin shell of shocked gas. The outer radius of the shocked gas is given by [Parizot et al., 2004]:

$$R_{\rm ext} \sim 13 t_{\rm Myr}^{3/5} \left(\frac{L_{\rm wind}}{3 \cdot 10^{36} {\rm erg/s}} \right)^{1/5} \left(\frac{n}{10^2 cm^{-3}} \right)^{-1/5} {\rm pc}, \tag{4.26}$$

with the last two terms approximately equal to 1. This radius is considerably larger than the R_* in Eq. (4.25), so that the individual wind bubbles actually collide and merge during the first million years. This results in a large collective bubble expanding around the whole OB association, even before the first supernova explosion [Parizot et al., 2004]. Further more energy input is provided by subsequent supernova explosions after the stars' lifetime. Thus, superbubbles are good candidates as high energy cosmic ray accelerators. The recent detection of GeV emission from Cygnus superbubble by the Fermi collaboration provides a proof that superbubbles are efficient accelerators where protons and electrons can be accelerated to the maximum energies of $80 - 300$ and $6 - 50$ TeV [Ackermann et al., 2011].

4.6.2 The superbubble 30 Dor C

30 Dor C was discovered by Le Marne [1968] in the radio band. Later a shell-like structure with a radius of about $3'$ was found in the 843 MHz band by Mills et al. [1984]. The X-ray emission of this object is first detected by the Einstein satellite [Long et al., 1981] and later extensively studied with other higher resolution instruments. A clear shell-like structure in the X-ray band confined within the H_α shell is found with ROSAT by Dunne et al. [2001] and interpreted as the emission from the interaction between the superbubble and an interior SNR. The spectrum shows a thermal emission with a high temperature of $\sim 1\,$keV. The non-thermal emission in the hard X-ray band is found in the western part of the shell by Dennerl et al. [2001] with the XMM-Newton, Bamba et al. [2004] with the Chandra, and Yamaguchi et al. [2009] with the Suzaku data. The hard X-ray emission resemble the synchrotron X-ray in the shock front of SNRs, revealed as a site of cosmic-ray acceleration.

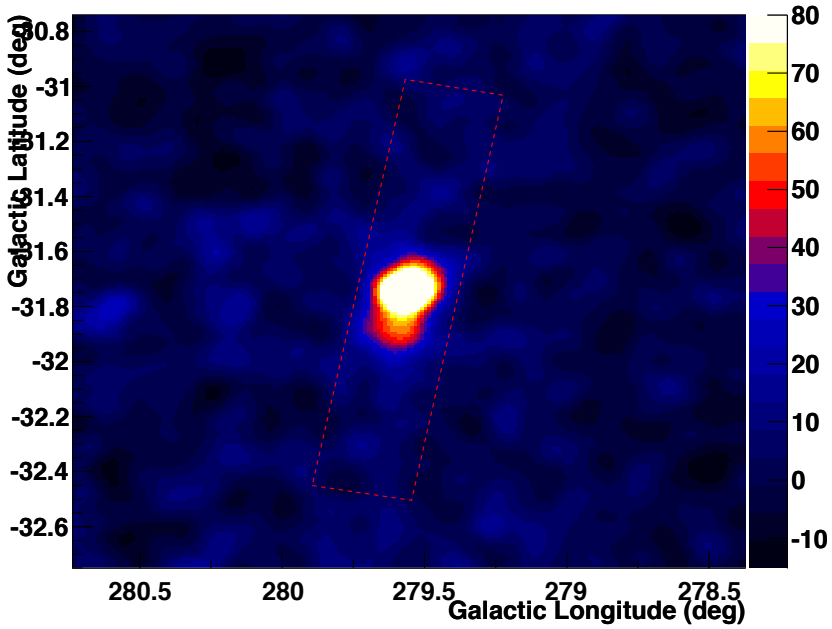

Figure 4.15: The $hires_{\zeta,\mathrm{dm}}$ excess map in Galactic coordinates of the 30 Dor region. The map is smoothed with a 2-D Gaussian with a width of 0.07° for better visualization. The sliced region for the 1-D projections shown in Figure 4.16, 4.17, and 4.18 is denoted by the red box.

4.6.3 VHE γ-ray emission from 30 Dor C

The skymaps in Figure 4.5 suggest the existence of a second source since as discussed in Section 4.5.1, N 157B is expected to be a point source. Figure 4.16–4.18 show the 1-D projection of the excess events in the 30 Dor region (as defined by the red box ($0.3° \times 1.5°$) in Figure 4.15) on the pre-defined axis which passes through the position of PSR J0537-6910 and the center of 30 Dor C (the center of the circle in Figure 4.3. The projected angular distributions of the excess events are fit with one and two Gaussians. For the *std* configurations with a poorer angular resolution, there is no clear indication of a second source. For $hard_{\zeta,\mathrm{gm}}$, $hard_{\zeta,\mathrm{dm}}$ and $hires_{\zeta,\mathrm{dm}}$ configurations, two-Gaussian models are favored by TS values of 7, 13, and 21 respectively, corresponding to the significance values of 1.8σ, 2.8σ and 3.9σ.

The position of this emission just next to N 157B coincide with the position of 30 Dor C. The significance in a pre-defined *On-region* (the circle in 4.3) is calculated for all configurations as listed in Table 4.5. The highest significance of

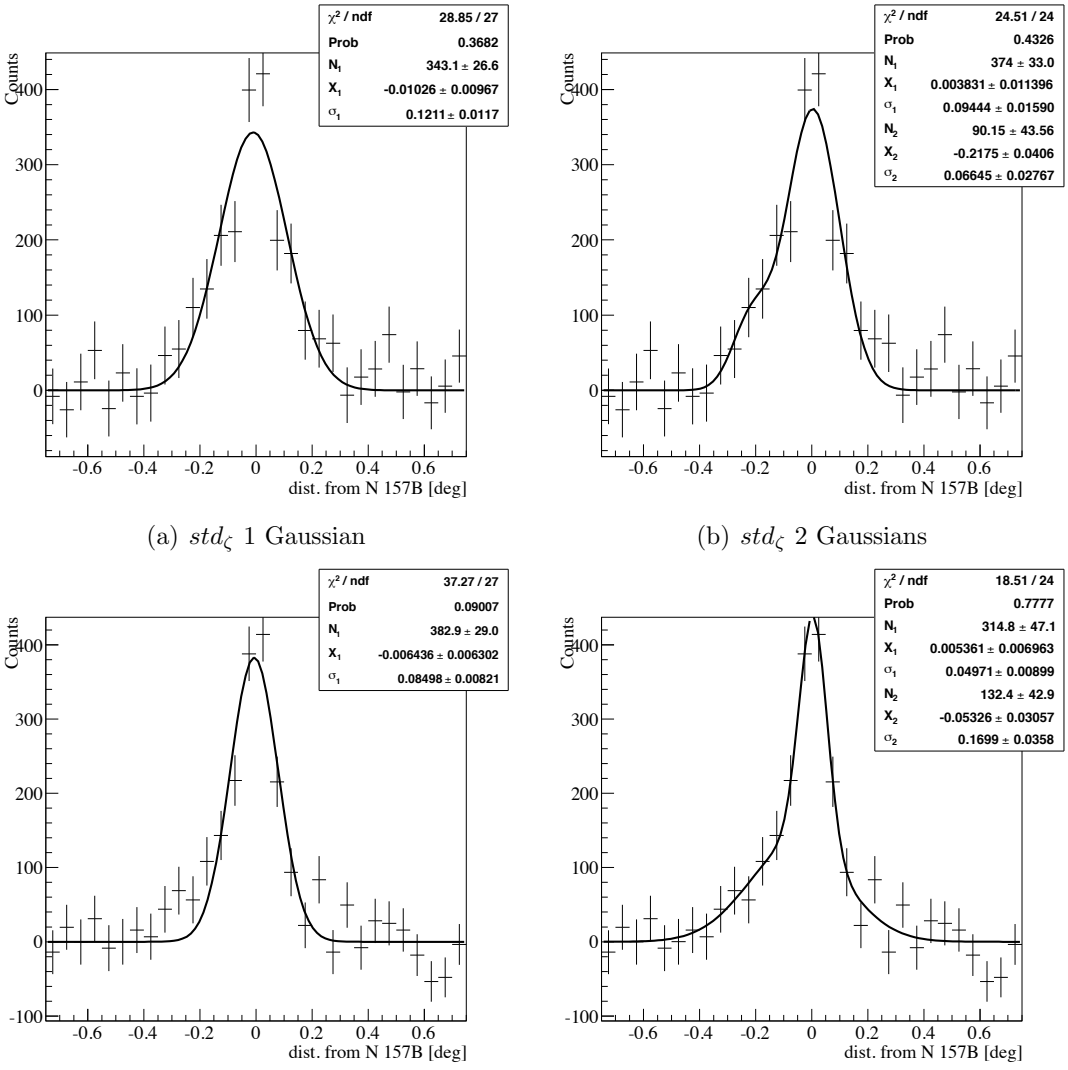

(a) std_{ζ} 1 Gaussian

(b) std_{ζ} 2 Gaussians

(c) $std_{\zeta,\mathrm{dm}}$ 1 Gaussian

(d) $std_{\zeta,\mathrm{dm}}$ 2 Gaussians

Figure 4.16: 1-D projections of the excess events with the *std* configurations in the sliced region around 30 Dor as marked by the red box in Figure 4.15.

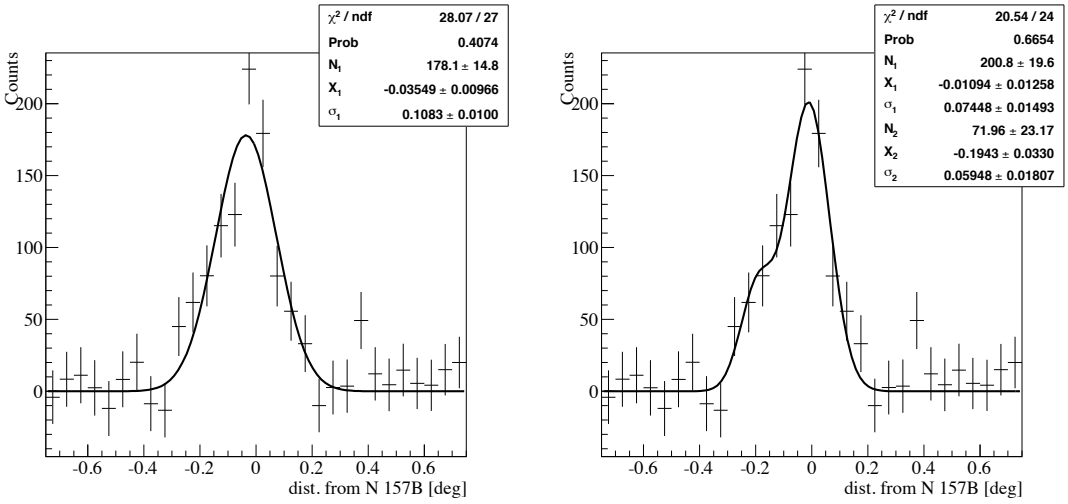

(a) $hard_{\zeta}$ 1 Gaussian

(b) $hard_{\zeta}$ 2 Gaussian

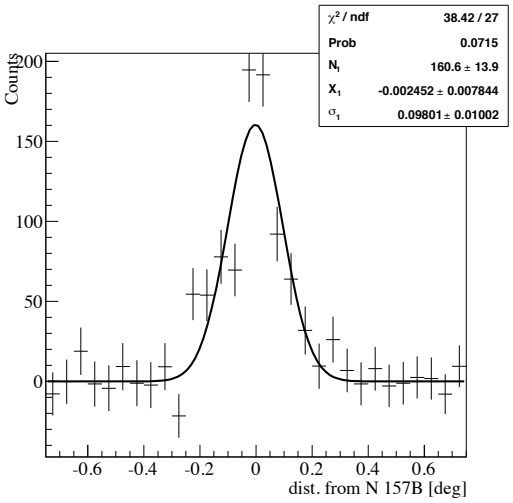

(c) $hard_{\zeta,\mathrm{dm}}$ 1 Gaussian

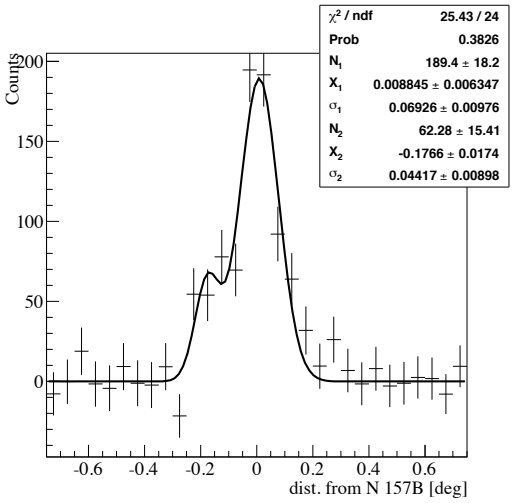

(d) $hard_{\zeta,\mathrm{dm}}$ 2 Gaussian

Figure 4.17: 1-D projections of the excess events with the *hard* configurations in the sliced region around 30 Dor as marked by the red box in Figure 4.15.

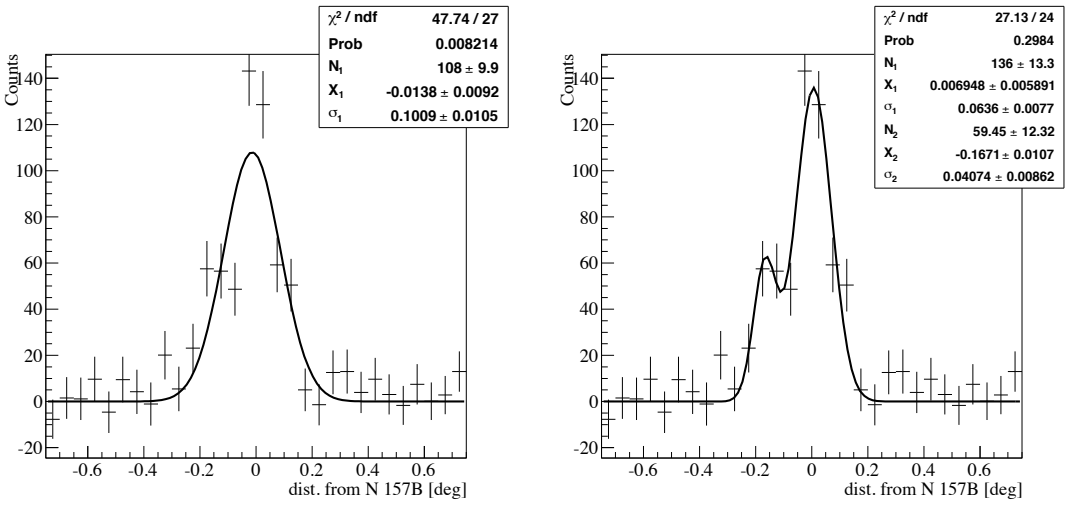

(a) $hires_{\zeta,\mathrm{dm}}$ 1 Gaussian

(b) $hires_{\zeta,\mathrm{dm}}$ 2 Gaussian

Figure 4.18: 1-D projections of the excess events with the $hires_{\zeta,\mathrm{dm}}$ configuration in the sliced region around 30 Dor as marked by the red box in Figure 4.15.

7.4σ is obtained with the $hires_{\zeta,dm}$ configuration.

The excess shown in Table 4.5 is expected to have leakage emission from N 157B since the tested *On-region* is only 0.15° away from the position of N 157B. To take into account the contamination from N 157B and to estimate the reliability of the signal from 30 Dor C, the models of single point source and two point sources are tested with the maximum likelihood method. The best fit positions and the significance of the second source, calculated by the TS value, which is the difference of the likelihood of the two models, are listed in Table 4.6. The maximum significance of 5.5, calculated by the TS value of 37 under 3 degree of freedom, is obtained with the $hires_{\zeta,\mathrm{dm}}$ configuration.

As shown in Figure 3.31, the $hires_{\zeta,\mathrm{dm}}$ configuration has an intrinsic width for point sources which may arise from the systematic effects introduced from e.g. broken pixels. Figure 3.34(b) shows that for the $hires_{\zeta,\mathrm{dm}}$ configuration, broken pixels may result in an increase of 15% to the PSF size, depending on the broken pixel pattern and zenith angle. To check the influence of an enlarged PSF on the fit result, fitting of a PSF enlarged by 15% of the original size is tested and shows a consistent result as shown in Table 4.6.

The best fit positions are overlapped with the X-ray Chandra image in Figure 4.19. The fit positions are close to the most intensive part of the shell, where the hard X-ray non-thermal emission is interpreted as synchrotron radiation in the shock front of SNRs [Bamba et al., 2004; Dennerl et al., 2001].

Config.	Max θ^2[deg^2]	$N_{\rm On}$	$N_{\rm Off} \cdot \alpha$	Excess	Sig.[σ]
std_ζ	0.005	1734	1523	211	5.2
$std_{\zeta,\rm dm}$	0.005	1149	984	165	5.0
$hard_\zeta$	0.005	494	375	119	5.7
$hard_{\zeta,\rm dm}$	0.005	311	105	206	6.6
$hires_{\zeta,\rm dm}$	0.005	160	82	78	7.4

Table 4.5: The statistics of γ-ray-like events passing *post-selection* of different configurations in the 30 Dor C region. The θ^2 cut used here is set to be 0.005 deg^2 in all configuration to avoid signal contamination from N 157B. This values is different from the optimized values for point sources, which are 0.0125 deg^2 for std_ζ configurations, 0.01 deg^2 for $hard_\zeta$ configurations and 0.005 deg^2 for the $hires_{\zeta,\rm dm}$ configuration.

Config.	l[deg]	b[deg]	TS	Sig.[σ]	N_2/N_1
std_ζ	$279:33:25 \pm 54''$	$-31:55:05 \pm 47''$	17	3.4	0.27 ± 0.06
$std_{\zeta,\rm dm}$	$279:34:48 \pm 43''$	$-31:54:32 \pm 18''$	26	4.4	0.29 ± 0.05
$hard_\zeta$	$279:33:14 \pm 40''$	$-31:54:54 \pm 36''$	24	4.2	0.29 ± 0.05
$hard_{\zeta,\rm dm}$	$279:35:31 \pm 40''$	$-31:53:42 \pm 36''$	24	4.2	0.23 ± 0.04
$hires_{\zeta,\rm dm}$	$279:35:13 \pm 32''$	$-31:53:28 \pm 29''$	37	5.5	0.28 ± 0.05
$hires_{\zeta,\rm dm,15\%}$	$279:35:35 \pm 32''$	$-31:53:49 \pm 29''$	37	5.5	0.30 ± 0.05

Table 4.6: Fit parameters of the second source in the 30 Dor region. N_2/N_1 is the ratio between the normalization factor of the second and first source. Sig. is the abbreviation of significance. The raw of $hires_{\zeta,\rm dm,15\%}$ is the fit result by a PSF enlarged with 15% of the original size.

The values of the fit relative normalization of the two source are also listed in Table 4.6. The values range between 0.23 and 0.30 for all configurations within good agreement in 1σ statistical uncertainties. Assuming the two sources have the same spectral index, one can estimate the γ-ray flux of the second source by multiplying this value with the γ-ray flux of N 157B. Taking the relative normalization value of 0.28, the estimated γ-ray flux between $1 - 10$ TeV of the second source is $(1.6 \pm 0.3) \times 10^{-13}$cm^{-2}s^{-1}, corresponding to the energy γ-ray flux of $(4.8 \pm 0.9) \times 10^{-13}$erg cm^{-2}s^{-1}. For a hadronic scenario, with an ambient density of 38 cm^{-3}, the energy stored in the proton population is required to be 1.3×10^{50} erg, roughly equaling to the output energy of one supernova explosion.

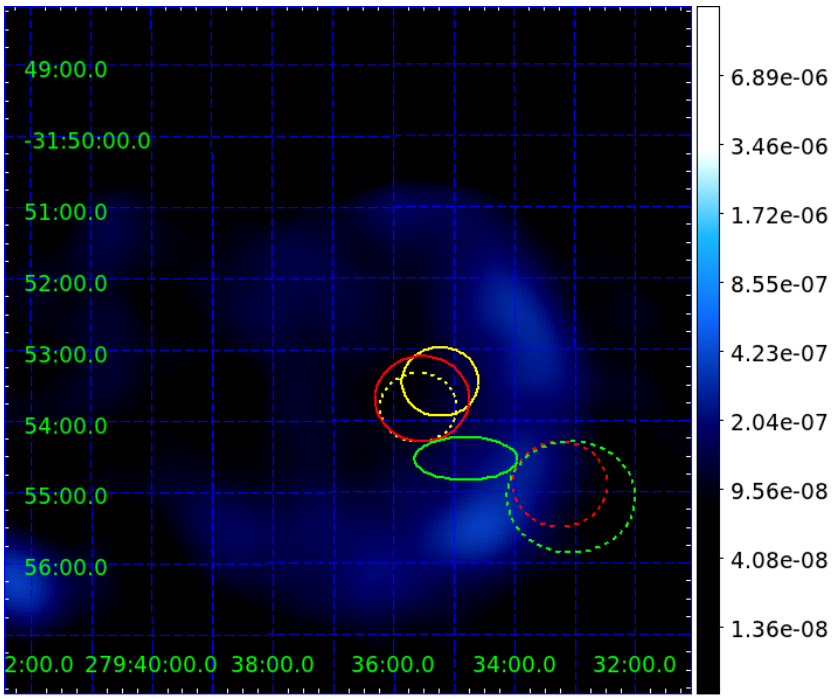

Figure 4.19: The best fit positions of the second source overlapped with the Chandra image of 30 Dor C. Each ellipse denotes the 1σ statistical uncertainty on the fit position. Green solid: $std_{\zeta,\mathrm{dm}}$. Green dashed: std_{ζ}. Red solid: $hard_{\zeta,\mathrm{dm}}$. Red dashed: $hard_{\zeta}$. Yellow solid: $hires_{\zeta,\mathrm{dm}}$. Yellow dashed: $hires_{\zeta,\mathrm{dm},15\%}$.

Conclusions and Outlook

In this work, an advanced direction reconstruction technique using the *Disp method* is developed. The performance of this technique is compared with the currently-used *Geometrical reconstruction*. The angular resolution, defined as the 68% containment radius of the point spread function, of *Geometrical reconstruction* degrades very quickly with the zenith angle: 0.1° at the zenith and 0.2° at 60° zenith angle. The angular resolution is significantly improved by the *Disp method* at zenith angles larger than 45°. For events from high zenith angles at 0.5°-1.5° offsets, the improvement is 20%–40% between 45°-60° zenith angles. For offsets larger than 2.0, there is an additional improvement of 5%-10%. Due to the improved angular resolution, the γ efficiency, effective area and Q factor are also increased. The high resolution configuration, $hires_{\zeta,\mathrm{dm}}$, with an extra cut on the direction uncertainty is set up. For a 0.5° offset, by losing about 50% of effective detection area (compared with $hard_{\zeta,\mathrm{dm}}$) configuration, an angular resolution of $\sim 0.055°$ is achieved. The Q factor is reduced by only 20% since this cut is also efficient on rejecting hadrons.

Systematic tests on spectral and morphology fits to known sources for *std* and *hard* configurations with this technique show a good agreement with the currently-used one. The morphology fits for the $hires_{\zeta,\mathrm{dm}}$ configuration show a systematic extension of ~ 0.025. This systematic bias may result from the the broken pixels in real data which is not considered in Monte-Carlo simulations where a perfectly-functioning instrument is assumed.

The seven-year observation of LMC yields a livetime of 169 hr. No significant point-like emission from SN 1987a is found. Calculated upper limits on integral γ-ray flux are at the same magnitude with model predictions. A bright source is found and identified as the pulsar wind nebula of PSR J0537-6910 in the supernova remnant N 157B. The fit spectral index and integral flux are consistent with the values in the 2012 paper. The total energy stored in electrons is estimated to be $2 \sim 4 \times 10^{49}$ erg with a pure leptonic scenario.

A second source only $\sim 0.15°$ away from the PWN is found with a significance of 5.5σ by the morphology fit with the $hires_{\zeta,\mathrm{dm}}$ configuration. The best positions are close to the most intensive part of the non-thermal X-ray emission from the

superbubble 30 Dor C. For a hadronic scenario, the total energy stored in the proton population is estimated to be 10^{50} erg, roughly equaling to the output energy of one supernova explosion. Despite the coincidence of the positions, if this source is associated with 30 Dor C still needs further investigations. The emission contamination from N 157B makes the spectral analysis of this source difficult. A tool of simultaneous fit of two spectra is needed to derive the spectral index of the weak source.

For future work, the *Disp method* reconstruction can be applied widely to every kind of sources. The $hires_{\zeta,\mathrm{dm}}$ configuration with a better angular resolution is suitable for studies of sources with complicated morphology and the crowded regions in the Galactic plane. The $std_{\zeta,\mathrm{dm}}$ and $hard_{\zeta,\mathrm{dm}}$ configurations with an improved sensitivity at large zenith angles can be used to search for new sources.

Acknowledgements

In the past, I once thought it was *funny* to put so many names and affiliations on publications that they occupied almost one page. After these three and half years, I realize a thought like that is *ridiculous*. My thesis is also an outcome of teamwork. There are so many people I don't even know their name, but I know I can accomplish nothing without their work of building and maintaining the instruments and software. So first, I would like to thank the whole H.E.S.S. collaboration. I would like to thank Prof. Werner Hofmann for creating the great working environment in MPIK and suggesting the LMC as the topic for my thesis, Prof. Wagner and Prof. Voelk, the members of my thesis committee for discussing the outlines of my thesis. I would like to thank Andre, Raquel, Christopher, Stefan for helping me to learn the analysis, Hilly for setting up TMVA for my new reconstruction method, and Henning for his great new lookup scheme and the very useful suggestions for my work. I would like to thank Dan and Christoph for the very nice discussions and proof-reading, especially about the technical part of my thesis, Konrad for explaining me many details about the air shower, and Willy for the discussions about the exciting science. I would like to thank my officemate Joachim for the many nice songs he has composed for me, and Petter for the amazingly beautiful secret paths in the forest, Dirk for the funny photos and videos he took of me. I also would like to thank Ruth and Christian for all kinds of helps, especially at the beginning of my Ph.D., to make living in a foreign country easier . Finally, my parents and Prof. Lin. You always respect my decisions and provide all the possible supports, accompanying me to go through all the ups and downs in my life. Thank you is definitely not enough so I want to say: I love you.

References

Acero, F., Aharonian, F., Akhperjanian, A. G., et al. Detection of Gamma Rays from a Starburst Galaxy. *Science*, 326 (2009), 1080. 48

Ackermann, M., Ajello, M., Allafort, A., et al. A Cocoon of Freshly Accelerated Cosmic Rays Detected by Fermi in the Cygnus Superbubble. *Science*, 334 (2011), 1103. 111

Aharonian, F., Akhperjanian, A. G., Aye, K.-M., et al. Very high energy gamma rays from the direction of Sagittarius A*. *A&A*, 425 (2004), L13. 18

Aharonian, F., Akhperjanian, A. G., Aye, K.-M., et al. H.E.S.S. observations of PKS 2155-304. *A&A*, 430 (2005), 865. 75

Aharonian, F., Akhperjanian, A. G., Bazer-Bachi, A. R., et al. Observations of the Crab nebula with HESS. *A&A*, 457 (2006), 899. 72, 73, 75

Aliu, E., Anderhub, H., Antonelli, L. A., et al. Observation of Pulsed γ-Rays Above 25 GeV from the Crab Pulsar with MAGIC. *Science*, 322 (2008), 1221. 81

Atwood, W. B., Abdo, A. A., Ackermann, M., et al. The Large Area Telescope on the Fermi Gamma-Ray Space Telescope Mission. *ApJ*, 697 (2009), 1071. 1

Bamba, A., Ueno, M., Nakajima, H., et al. Thermal and Nonthermal X-Rays from the Large Magellanic Cloud Superbubble 30 Doradus C. *ApJ*, 602 (2004), 257. 111, 115

Berezhko, E. G. and Ksenofontov, L. T. Cosmic Rays, Radio and Gamma-Ray Emission from the Remnant of Supernova 1987A. *Astronomy Letters*, 26 (2000), 639. 100

Berezhko, E. G. and Ksenofontov, L. T. Magnetic Field in Supernova Remnant SN 1987A. *ApJL*, 650 (2006), L59. 100

Berezhko, E. G., Ksenofontov, L. T., and Völk, H. J. Expected Gamma-Ray Emission of Supernova Remnant SN 1987A. *ApJ*, 732 (2011), 58. 100, 103

Berge, D. *A detailed study of the gamma-ray supernova remnant RX J1713.7-3946 with H.E.S.S.* Ph.D. thesis (2010). 46

Berge, D., Funk, S., and Hinton, J. Background modelling in very-high-energy γ-ray astronomy. *A&A*, 466 (2007), 1219. 41

Bernloehr, K. Geomagnetic effects on showers relevant for the H.E.S.S. experiment. *H.E.S.S internal note*, (2005). 53, 58

Bernlohr, K. Impact of atmospheric parameters on the atmospheric Cherenkov technique. *Astropart.Phys.*, 12 (2000), 255. 16

Bernlöhr, K. Monte Carlo images of air showers. `http://www.mpi-hd.mpg.de/hfm/~bernlohr/HESS/` (2000). 6

Bernlöhr, K. Simulation of imaging atmospheric Cherenkov telescopes with CORSIKA and sim_telarray. *Astroparticle Physics*, 30 (2008), 149. 16

Bica, E. L. D., Schmitt, H. R., Dutra, C. M., et al. A Revised and Extended Catalog of Magellanic System Clusters, Associations, and Emission Nebulae. II. The Large Magellanic Cloud. *AJ*, 117 (1999), 238. 93

Bresolin, F., Kennicutt, R. C., Jr., and Garnett, D. R. The Ionizing Stars of Extragalactic H II Regions. *ApJ*, 510 (1999), 104. 110

Burrows, D. N., Michael, E., Hwang, U., et al. The X-Ray Remnant of SN 1987A. *ApJL*, 543 (2000), L149. 101

Cash, W. Parameter estimation in astronomy through application of the likelihood ratio. *ApJ*, 228 (1979), 939. 42

Chadwick, P. M., Lyons, K., McComb, T. J. L., et al. Very High Energy Gamma Rays from PKS 2155-304. *ApJ*, 513 (1999), 161. 75

Daum, A., Hermann, G., Hess, M., et al. First results on the performance of the HEGRA IACT array. *Astroparticle Physics*, 8 (1997), 1. 12

de Geus, E. J. Interaction of massive stars with the interstellar medium. In K. Janes (editor), *The Formation and Evolution of Star Clusters*, volume 13 of *Astronomical Society of the Pacific Conference Series*, pages 40–54 (1991). 110

de Naurois, M. and Rolland, L. A high performance likelihood reconstruction of γ-rays for imaging atmospheric Cherenkov telescopes. *Astroparticle Physics*, 32 (2009), 231. 107

Deil, C. *Private communication*, (2013). 17

Dennerl, K., Haberl, F., Aschenbach, B., et al. The first broad-band X-ray images and spectra of the 30 Doradus region in the LMC. *A&A*, 365 (2001), L202. 111, 115

Domingo-Santamaria, E., Flix, J., Rico, J., et al. The DISP analysis method for point-like or extended gamma source searches/studies with the MAGIC Telescope. In *International Cosmic Ray Conference*, volume 5 of *International Cosmic Ray Conference*, page 363 (2005). 23

Dunne, B. C., Points, S. D., and Chu, Y.-H. X-Rays from Superbubbles in the Large Magellanic Cloud. VI. A Sample of Thirteen Superbubbles. *ApJS*, 136 (2001), 119. 111

Enomoto, R., Bicknell, G. V., Clay, R. W., et al. CANGAROO-III Search for Gamma Rays from SN 1987A and the Surrounding Field. *ApJ*, 671 (2007), 1939. 103

Fermi, E. On the Origin of the Cosmic Radiation. *Physical Review*, 75 (1949), 1169. 86

Fey, A. L., Ma, C., Arias, E. F., et al. The Second Extension of the International Celestial Reference Frame: ICRF-EXT.1. *AJ*, 127 (2004), 3587. 76

Fomin, V. P., Stepanian, A. A., Lamb, R. C., et al. New methods of atmospheric Cherenkov imaging for gamma-ray astronomy. I. The false source method. *Astroparticle Physics*, 2 (1994), 137. 23

Freund, Y. and Schapire, R. E. A decision-theoretic generalization of on-line learning and an application to boosting. *J. Comput. Syst. Sci.*, 55 (1997) 1, 119.
URL `http://dx.doi.org/10.1006/jcss.1997.1504` 37

Garmany, C. D. OB associations: Massive stars in context. *PASP*, 106 (1994), 25. 110

Gast, H. A new lookup scheme for hap. (2011). 57

Glueck, B. *A Detailed Study of the Pulsar Wind Nebula HESS J0835455 (Vela X) in TeV Gamma-Rays*. Ph.D. thesis (2011). 40

Hahn, J. Ensuring long-term stability of data quality selection for H.E.S.S. under challenging atmospheric conditions. *H.E.S.S. internal note*, (2012). 75, 96

Hartman, R. C., Bertsch, D. L., and Bloom, S. D. Third EGRET catalog (3EG) (Hartman+, 1999). *VizieR Online Data Catalog*, 212 (1999), 30079. 1

Heck, D., Knapp, J., Capdevielle, J. N., et al. *CORSIKA: a Monte Carlo code to simulate extensive air showers.* (1998). 16

Heitler, W. Dover Press, 3rd edition (1954). 2

H.E.S.S. Collaboration, Abramowski, A., Acero, F., et al. VHE γ-ray emission of PKS 2155-304: spectral and temporal variability. *A&A*, 520 (2010), A83. 75, 76

H.E.S.S. Collaboration, Abramowski, A., Acero, F., et al. Discovery of gamma-ray emission from the extragalactic pulsar wind nebula N 157B with H.E.S.S. *A&A*, 545 (2012), L2. 107

Hillas, A. M. "Cerenkov light images of EAS produced by primary gamma". In F. C. Jones (editor), *International Cosmic Ray Conference*, volume 3, pages 445–448 (1985). 18, 19, 31

Hinton, J. A. The status of the HESS project. *New Astronomy Review*, 48 (2004), 331. 12

Hinton, J. A. and Hofmann, W. Teraelectronvolt Astronomy. *ARA&A*, 47 (2009), 523. 88, 92

Hoecker, A., Speckmayer, P., Stelzer, J., et al. TMVA - Toolkit for Multivariate Data Analysis. *ArXiv Physics e-prints*, (2007). 35

Hofmann, W., Jung, I., Konopelko, A., et al. Comparison of techniques to reconstruct VHE gamma-ray showers from multiple stereoscopic Cherenkov images. *Astroparticle Physics*, 12 (1999), 135. 18, 21, 23

Hoppe, S. *Emitters of VHE gamma-radiation as revealed by the H.E.S.S. Galactic plane survey.* Ph.D. thesis, Ruperto-Carola University of Heidelberg (2008). 13

Kardashev, N. S. Nonstationarity of Spectra of Young Sources of Nonthermal Radio Emission. *Soviet Astronomy*, 6 (1962), 317. 91

Kargaltsev, O. and Pavlov, G. G. Pulsar-wind nebulae in X-rays and TeV γ-rays. *X-ray Astronomy 2009; Present Status, Multi-Wavelength Approach and Future Perspectives*, 1248 (2010), 25. 105, 107

Komin, N. Poster, Nr. Thu-299. *COSPAR Scientific Assembbly, Bremen*, (2010). 103

Koshiba, M., Thomas, M., Ryder, S., et al. Supernova 1987A in the Large Magellanic Cloud. *IAU Circ.*, 4338 (1987), 1. 99

Kranich, D. and Stark, L. S. An New Method to Determine the Arrival Direction of Individual Air Showers with a Single Air Cherenkov Telescope. In *International Cosmic Ray Conference*, volume 5 of *International Cosmic Ray Conference*, page 3023 (2003). 23

Le Marne, A. E. High resolution observations of the 30 Doradus Nebula at 408 MHz. *MNRAS*, 139 (1968), 461. 111

Lessard, R. W., Buckley, J. H., Connaughton, V., et al. A new analysis method for reconstructing the arrival direction of TeV gamma rays using a single imaging atmospheric Cherenkov telescope. *Astroparticle Physics*, 15 (2001), 1. 23

Li, T.-P. and Ma, Y.-Q. Analysis methods for results in gamma-ray astronomy. *ApJ*, 272 (1983), 317. 42, 45

Lobanov, A. P., Horns, D., and Muxlow, T. W. B. VLBI imaging of a flare in the Crab nebula: more than just a spot. *A&A*, 533 (2011), A10. 76

Long, K. S., Helfand, D. J., and Grabelsky, D. A. A soft X-ray study of the Large Magellanic Cloud. *ApJ*, 248 (1981), 925. 111

Longair, M. *High energy Astrophysics*, volume 1 (1992a). 2

Longair, M. *High energy Astrophysics*, volume 2 (1992b). 86, 87, 89

Lorenz, E. Status of the 17 m MAGIC telescope. *New Astronomy Review*, 48 (2004), 339. 12

Macri, L. M., Stanek, K. Z., Bersier, D., et al. A New Cepheid Distance to the Maser-Host Galaxy NGC 4258 and Its Implications for the Hubble Constant. *ApJ*, 652 (2006), 1133. 91

Manchester, R. N., Hobbs, G. B., Teoh, A., et al. ATNF Pulsar Catalog (Manchester+, 2005). *VizieR Online Data Catalog*, 7245 (2005), 0. 105

Marshall, F. E., Gotthelf, E. V., Zhang, W., et al. Discovery of an Ultrafast X-Ray Pulsar in the Supernova Remnant N157B. *ApJL*, 499 (1998), L179. 105

Mayer, M., Brucker, J., Jung, I., et al. Implications on the X-ray emission of evolved pulsar wind nebulae based on VHE gamma-ray observations. *ArXiv e-prints*, (2012). 106

Mills, B. Y., Turtle, A. J., Little, A. G., et al. A new look at radio supernova remnants. *Australian Journal of Physics*, 37 (1984), 321. 111

Moderski, R., Sikora, M., Coppi, P. S., et al. Klein-Nishina effects in the spectra of non-thermal sources immersed in external radiation fields. *MNRAS*, 363 (2005), 954. 90

Nikolaev, S., Drake, A. J., Keller, S. C., et al. Geometry of the Large Magellanic Cloud Disk: Results from MACHO and the Two Micron All Sky Survey. *ApJ*, 601 (2004), 260. 93

Ohm, S. *Advanced gamma/hardron separation technique and application to particular gamma-ray sources with H.E.S.S.* Ph.D. thesis (2010). 3, 36, 38, 48

Parizot, E., Marcowith, A., van der Swaluw, E., et al. Superbubbles and energetic particles in the Galaxy. I. Collective effects of particle acceleration. *A&A*, 424 (2004), 747. 110, 111

Pietrzyński, G., Gieren, W., Fouqué, P., et al. A Catalog of OB Associations in the spiral galaxy NGC 300. *A&A*, 371 (2001), 497. 110

Rowell, G., Hinton, J., and H.E.S.S. Collaboration. Preliminary results from a search for TeV γ-ray emission from SN1987A and the surrounding field with H.E.S.S. In F. A. Aharonian, H. J. Völk, and D. Horns (editors), *High Energy Gamma-Ray Astronomy*, volume 745 of *American Institute of Physics Conference Series*, pages 299–304 (2005). 93

Sanchez, D. and Marandon, V. Effect of the broken pixels on the H.E.S.S. PSF. (2012). 81, 83

Schaller, G., Schaerer, D., Meynet, G., et al. New grids of stellar models from 0.8 to 120 solar masses at Z = 0.020 and Z = 0.001. *A&A Supplement*, 96 (1992), 269. 110

Sreekumar, P., Bertsch, D. L., Dingus, B. L., et al. Observations of the Large Magellanic Cloud in high-energy gamma rays. *ApJL*, 400 (1992), L67. 93

The Fermi/LAT collaboration and Abdo, A. A. Observations of the Large Magellanic Cloud with Fermi. *ArXiv e-prints*, (2010). 93

Ulrich, M. *Eine neue Bildanalysemethode fuer Abbildende Atmosphaerische Cherenkov Teleskope und die zweidimensionale Richtungsrekonstruktion von TeV-Photonen des Krebs-Nebels*. Ph.D. thesis, Ruperto-Carola University of Heidelberg, Germany (1996). 8

VERITAS Collaboration, Aliu, E., Arlen, T., et al. Detection of Pulsed Gamma Rays Above 100 GeV from the Crab Pulsar. *Science*, 334 (2011), 69. 81

Voelk, H. *Private communication*, (2013). 104

Weaver, R., McCray, R., Castor, J., et al. Errata: Interstellar Bubbles. II. Structure and Evolution. *ApJ*, 220 (1978), 742. 110

Weekes, T. C., Badran, H., Biller, S. D., et al. VERITAS: the Very Energetic Radiation Imaging Telescope Array System. *Astroparticle Physics*, 17 (2002), 221. 12

Weekes, T. C., Cawley, M. F., Fegan, D. J., et al. Observation of TeV gamma rays from the Crab nebula using the atmospheric Cerenkov imaging technique. *ApJ*, 342 (1989), 379. 40, 72

Weisskopf, M. C., Hester, J. J., Tennant, A. F., et al. Discovery of Spatial and Spectral Structure in the X-Ray Emission from the Crab Nebula. *ApJL*, 536 (2000), L81. 82

Wiedner, C. A. Site aspects of the H.E.S.S. project: astronomical and visibility conditions. *H.E.S.S. internal note*, (1998). 14

Wilks, S. S. The large-sample distribution of the likelihood ratio for testing composite hypotheses. *Annals of Mathematical Statistics*, 9 (1938), 60. 44

Winkler, C., Courvoisier, T. J.-L., Di Cocco, G., et al. The INTEGRAL mission. *A&A*, 411 (2003), L1. 1

Yamaguchi, H., Bamba, A., and Koyama, K. Suzaku Observation of 30 Dor C: A Supernova Remnant with the Largest Non-Thermal Shell. *PASJ*, 61 (2009), 175. 111